Final Technical Report

Report Date: July 22, 2011

Project Titles:	Simulation of Dimensional Changes and Hot Tears During Solidification of Steel Castings
DOE Award No:	DE-FC36-04GO14230
Project Period:	January 1, 2004 through June 30, 2011
Investigator:	Christoph Beckermann (Principal Investigator) phone: (319) 335-5681 e-mail: christoph-beckermann@uiowa.edu Kent Carlson (Author): phone: (319) 335-6075 e-mail: kent-carlson@uiowa.edu
Recipient Organization:	The University of Iowa Iowa City, Iowa 52242
Partners:	MAGMA Foundry Technologies Steel Founders' Society of America (SFSA) SFSA Member Foundries

Acknowledgement, Disclaimer and Proprietary Data Notice

Acknowledgement:	This report is based upon work supported by the U. S. Department of Energy under Award No. DE-FC36-04GO14230.
Disclaimer:	Any findings, opinions, and conclusions or recommendations expressed in this report are those of the authors and do not necessarily reflect the views of the Department of Energy.
Proprietary Data Notice:	This report does not contain any proprietary data.

Table of Contents

List of Acronyms

LVDT	linear voltage displacement transducer
PSD	porosity due to solid deformation
SFSA	Steel Founders’ Society of America

List of Figures

List of Tables

List of Appendices

Appendix A: "Development of a Hot Tear Indicator for Use in Casting Simulation," a paper by C. Monroe and C. Beckermann in Proceedings of the 58th SFSA Technical and Operating Conference, 2004.

Appendix B: "Development of a Hot Tear Indicator for Steel Castings," a paper by C. Monroe and C. Beckermann in *Materials Science and Engineering A*, 2005.

Appendix C: "Simulation of Hot Tearing and Distortion during Casting of Steel: Comparison with Experiments," a paper by C. Monroe and C. Beckermann in Proceedings of the 60th SFSA Technical and Operating Conference, 2006.

Appendix D: "Deformation during Casting of Steel: Model and Material Properties," a paper by C. Monroe and C. Beckermann in Proceedings of the 61st SFSA Technical and Operating Conference, 2007.

Appendix E: "Simulation of Deformation and Hot Tear Formation Using a Visco-Plastic Model with Damage," a paper by C. Monroe, C. Beckermann and J. Klinkhammer in Modeling of Casting, Welding, and Advanced Solidification Processes – XII, 2009.

Appendix F: "Prediction of Hot Tear Defects in Steel Castings Using a Damage Based Model," a paper by Z. Lin, C. Monroe, R. Huff and C. Beckermann in Modeling of Casting, Welding, and Advanced Solidification Processes – XII, 2009.

Executive Summary

During solidification, contractions or distortions of the steel, known as “dimensional changes,” can cause the final product to vary significantly from the original pattern. Cracks in the casting that form during the late stages of solidification, called “hot tears,” occur when contractions can no longer be accommodated by residual liquid metal flow or solid metal displacement. Dimensional changes and hot tears are major problems in the steel casting industry. These occurrences are difficult to anticipate and correct using traditional foundry engineering methods. While dimensional changes are accommodated using pattern allowances, the desired dimensions are often inaccurate. Castings that form hot tears must then be scrapped or weld repaired, expending unnecessary energy. Correcting either of these problems requires a tedious trial-and-error process that may not necessarily yield accurate results.

A model that predicts hot tears and dimensional changes during steel casting solidification has been successfully developed and implemented in commercial casting and stress analysis software. This model is based on a visco-plastic constitutive model with damage, where the damage begins to form when liquid feed metal is cut off to a solidifying region. The hot tear prediction is a locater for hot tear initiation sites, and not a full tear prediction: casting regions with relatively high damage values indicate where a casting is more likely to tear. In addition to model development, experimental castings were designed and produced, to provide both hot tear and dimensional change data during casting solidification and cooling. In both experimental castings and industrial production castings, regions of high damage were seen to correlate reasonably well with hot tear locations. Reasonable prediction of dimensional changes was also seen. The predictive capability of the model will improve with the development of more accurate high-temperature mechanical properties.

The hot tear/dimensional change model provides the steel casting industry with a tool that will result in a reduction of scrapped castings and re-work/repair due to dimensional changes or hot tears, and also an increase in casting yield due to a reduction in the use of padding and improved placement of risers, leading to better riser efficiency. This new technology is expected to result in an estimated energy savings of 2.15 trillion BTU’s/year. Along with these energy savings, reduction of scrap and improvement in casting yield will result in a reduction of the environmental emissions associated with the melting and pouring of the metal which will be saved as a result of this technology.

Introduction

Solidification is a crucial stage in steel casting production. During solidification, contractions or distortions of the steel, known as "dimensional changes," can cause the final product to vary significantly from the original pattern. Cracks in the casting that form during the late stages of solidification, called "hot tears," occur when contractions can no longer be accommodated by residual liquid flow or solid displacement. Dimensional changes and hot tears are major problems in the steel casting industry. These occurrences are difficult to anticipate and correct using traditional foundry engineering methods. While dimensional changes are accommodated using pattern allowances, the desired dimensions are often inaccurate. Castings that form hot tears must then be scrapped or weld repaired, expending unnecessary energy. Correcting either of these problems requires a tedious trial-and-error process that may not necessarily yield accurate results.

Prior research conducted by at The University of Iowa has shown that large dimensional changes are not possible without liquid flowing into or out of a casting section. Hot tears occur along the grain boundaries during the terminal stages of solidification when the stresses developed across adjacent grains exceed the strength of the almost completely solidified steel. Thus, hot tears are initiated in the residual liquid, and ruptured by contraction stresses. Some successes have been reported in predicting the final dimensions of and residual stresses in castings using stress analysis. However, these models cannot always predict results, in part due to their inability to account for liquid flow. Recently, the present researchers developed a model that predicts feeding flow and porosity formation during solidification, but that model assumes the solidified steel to be rigid and immobile. Hence, the occurrence of hot tears cannot be predicted. This project will combine these recently developed stress analysis and feeding flow/porosity models to form a reasonable starting point for a comprehensive, physics-based model of dimensional changes and hot tearing.

The goal of this part of the project is to develop a model to predict dimensional changes and hot tears during solidification of steel castings. The impact of this model on the steel casting industry will be a reduction in scrapped castings and re-work/repair due to dimensional changes or hot tears, and also an increase in casting yield due to a reduction in the use of padding and improved placement of risers, leading to better riser efficiency. This new technology is expected to result in an estimated energy savings of 2.15 trillion BTU's/year. Commercialization of this work will be a by-product of this project, because the model developed for this project is being developed within commercial casting simulation software. Once the model is complete, it will be commercially available.

Background

This section discusses the current state of the art in the modeling of dimensional changes and hot tears during steel casting solidification. Further, this section explains how the research performed for this project advances this state of the art. The approach used in developing this new technology is also briefly discussed.

Dimensional changes occur in steel casting because metal contracts as it solidifies and cools. Prediction of the final dimensions of a casting is difficult, because it involves consideration of how the metal shrinks as well as consideration of how the solidifying metal interacts with the mold and cores, both of which may hinder or otherwise influence the manner in which contracting metal may deform. Reasonable prediction of the final dimensions of a casting requires simulation of casting solidification/cooling as well as simulation of the stresses and strains that develop during this process. Advanced casting simulation software packages have the rudimentary ability to predict dimensional changes and even more approximately hot tears, but even the most advanced commercial software available does not account for the flow of liquid feed metal, nor for the presence of porosity in the metal. Both of these phenomena are important in order to correctly predict the final casting shape.

Hot tears are caused by the same phenomena that cause dimensional changes, and occur when a certain combination of conditions co-exist. Simply put, hot tears occur when solidifying steel is cut off from liquid feed metal, and is under tensile loading. Numerous hot tear indicators have been reported in the literature. Critical strain has been one measure of hot tearing susceptibility [1]. However, the critical strain is dependent on many other parameters, such as the availability of liquid metal feeding and strain rate and cannot be used alone as an indicator of hot tears [2]. A recently developed, physically based indicator is the Rappaz, Drezet and Gremaud (RDG) criterion developed by Rappaz et al. [3]. The RDG criterion is derived using a mass balance on a solidifying mushy zone. The mass balance is solved for the maximum sustainable strain rate. This is the strain rate beyond which cavitation or porosity formation occurs. The model is developed using a one-dimensional domain across the mushy zone and is thus not immediately applicable to three-dimensional situations. The RDG criterion also is sensitive to the definition of the coherency temperature, i.e., the temperature at which the dendritic network can transmit stresses. In continuous casting, this criterion is useful because the strain rate is directly related to the casting speed. However, it is not clear how the RDG criterion can be applied to shaped castings. Mo et al. [4] recently developed a two-phase model for hot tearing, where the energy, liquid and solid momentum and continuity equations are solved simultaneously. Similar to the RDG criterion, a hot tear criterion based on the liquid pressure drop is used. However, this model also has limitations because porosity formation is not considered. Additional references to previous research in this area can be found in the papers given in Appendices A – F.

The objective of this project is to develop a more general and accurate model to predict dimensional changes and hot tears during solidification of steel castings. The planned approach to accomplish this objective involves four steps:

1. Develop a stress and hot tear model: develop a model of dimensional changes and hot tears during solidification of steel castings.

2. Implement the model in commercial casting and stress analysis software.
3. Perform a validation experiment based on simulation results: perform a small-scale experiment to test and validate the model.
4. Perform a case study on production parts illustrating the use of the model in foundry practice: carefully compare predictions of the model to casting measurements to illustrate the use of the model in foundry practice.

The present researchers, who have extensive experience modeling various casting phenomena, have previously developed a model that predicts feeding flow and porosity during solidification of steel castings. This model, which is already available in commercial casting simulation software, will be utilized in the present model, since the inclusion of feeding flow and porosity are important in accurately predicting dimensional changes and hot tears.

Results and Discussion

The results of the research performed for this project are briefly presented and discussed in this section. The research is presented in full detail in the conference papers and journal articles contained in Appendices A – F.

The hot tear prediction model was created to utilize data that is available from casting simulations. Hot tears form when the mushy zone (i.e., the solidifying solid-liquid metal mixture) becomes cut off from the feed metal that feeds solidification shrinkage, and is then deformed in tension. This unfed tensile deformation creates porosity, which is termed porosity due to solid deformation (PSD), f_p^s. This porosity is in addition to the porosity due to solidification shrinkage, liquid mass flux, etc., which is symbolized by f_p^l. The total pore fraction occurring in a casting is the sum of these two: $f_p = f_p^s + f_p^l$. A physical model based on a mass balance was developed to determine the PSD. The end result of the model is the following equation:

$$\mathrm{PSD} = f_p^s = \frac{1}{\rho_l} \int_{f_p^l > 0}^{T < T_{sol}} \left[\boldsymbol{v}_s \cdot \nabla \left(f_s \rho_s \right) + f_s \rho_s \nabla \cdot \boldsymbol{v}_s \right] \mathrm{d}t \tag{1}$$

The derivation of this equation is given in Appendices A and B. In Eq. (1), f_s is the solid fraction, ρ_s and ρ_l are the solid and liquid densities, respectively, t is time, and $\boldsymbol{v}_s$ is the solid velocity. The solid fraction and the densities are available in solidification simulation results, and the solid velocity can be determined from stress simulation displacement results by dividing the change of the displacement, $\boldsymbol{u}$, by the time step:

$$\boldsymbol{v}_s = \frac{\Delta \boldsymbol{u}}{\Delta t} \tag{2}$$

The divergence of the solid velocity in Eq. (1) can be determined from the sum of the normal strain rate components, also available in stress simulation results:

$$\nabla \cdot \boldsymbol{v}_s = \dot{\varepsilon}_{xx} + \dot{\varepsilon}_{yy} + \dot{\varepsilon}_{zz} \tag{3}$$

To determine PSD, Eq. (1) must be integrated from the time that feeding is cut off from the local mushy zone until solidification is complete (i.e., $T = T_{sol}$). The time that feeding is cut off is modeled as the time that the porosity due to solidification shrinkage first becomes greater than zero, i.e., $f_p^l > 0$. As stated earlier, f_p^l includes porosity due to solidification shrinkage, which forms as soon as feeding is cut off. The porosity component f_p^l is predicted as part of the advanced feeding module (developed previously by the present researchers) available in the commercial casting simulation software being utilized in the present study. It is worth noting that previous hot tear models typically consider the beginning of hot tear modeling to be when the temperature drops below a coherency temperature, which is the temperature where the solid dendritic network will transmit stresses. However, this type of approach ignores the presence or absence of feed metal, which is an important consideration.

The procedure used to solve for PSD requires three steps: (1) perform an advanced feeding solidification simulation to determine the temperature, the porosity (f_p^l) and solid fractions, and the solid and liquid densities as a function of time during solidification and cooling; (2) perform a stress simulation based on the temperature results generated in the solidification simulation, to determine the displacements and normal strain rates as a function of time; and (3) using a user-programming interface available for the commercial casting simulation software utilized in the present research, gather the necessary values and calculate PSD throughout the casting by solving Eq. (1). Note that the PSD prediction is a locater for hot tear initiation sites, and not a full tear prediction: casting regions with relatively high PSD values indicate where a casting is more likely to tear. This is useful in comparing two casting designs, for example, and determining if one design is more or less likely to develop a tear.

The initial tests of this model were performed by simulating T-shaped casting hot tear experiments detailed in the literature, and determining how well the PSD predictions correlated with the results of the hot tear experiments. A schematic of the T-shaped castings is given in Fig. 1, which illustrates how the ends of the casting were fixed to prevent shrinkage and promote hot tearing in the T-junction. A comparison between the predicted average PSD in the hot tear region and the result of the experimental casting (tear, no tear) is given in Table 1. Pictures of the experimental castings and comparisons to the simulated PSD distributions are given in Appendices A and B.

Table 1 indicates that there is good correlation between relatively large PSD values and the presence of hot tears. All the castings that exhibited tears have high PSD values. The superiority of modeling the start of the PSD integration with the formation of porosity (i.e., $f_p^l > 0$) rather than with a coherency temperature limit, as in previous hot tear models, is demonstrated by

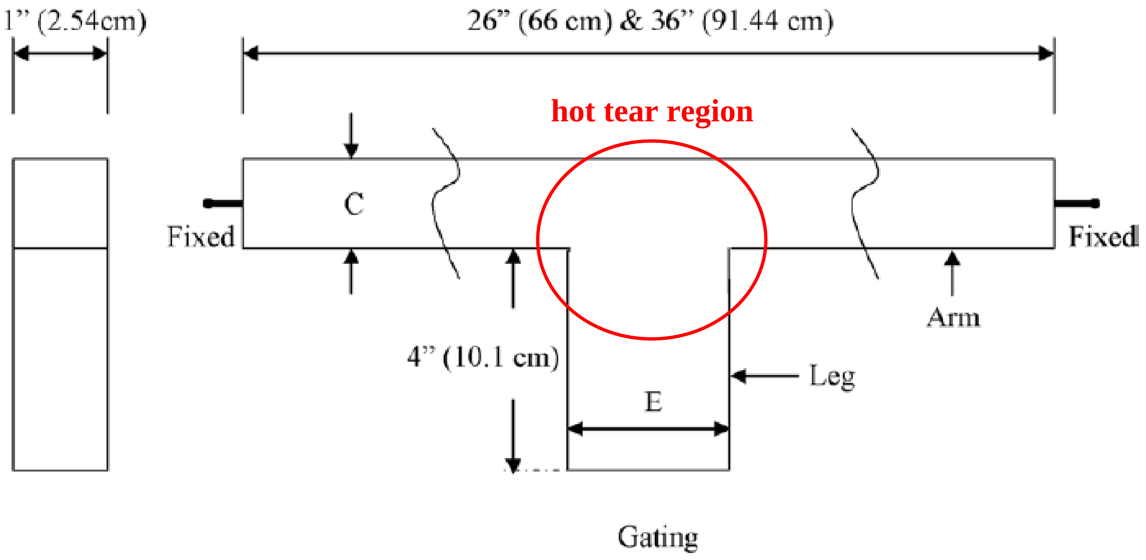

Figure 1. Schematic of the experimental T-shaped castings [5].

Table 1. Summary of hot tearing predictions and experimental results for the “T”-shaped steel castings of Ref. [5]

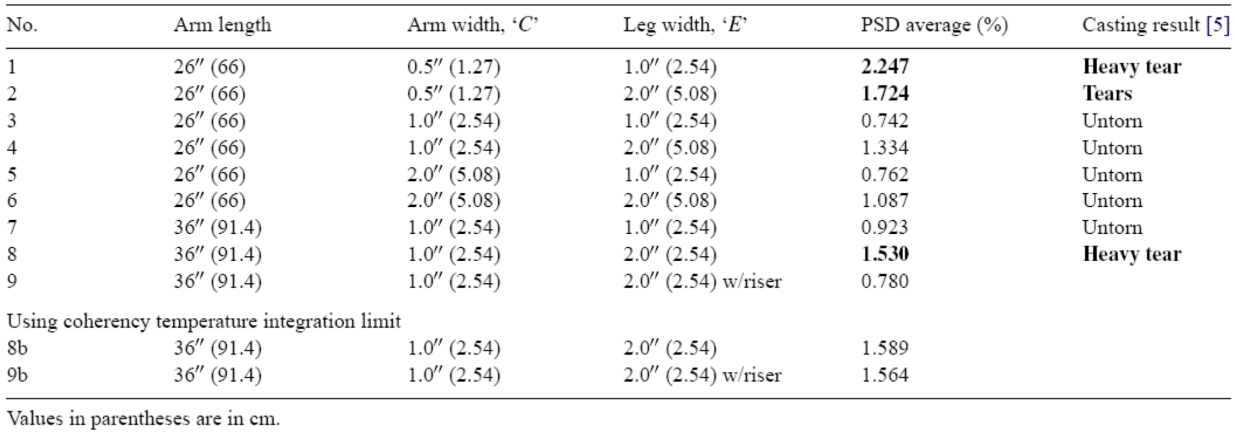

No.	Arm length	Arm width, ‘*C*’	Leg width, ‘*E*’	PSD average (%)	Casting result [5]
1	26″ (66)	0.5″ (1.27)	1.0″ (2.54)	**2.247**	**Heavy tear**
2	26″ (66)	0.5″ (1.27)	2.0″ (5.08)	**1.724**	**Tears**
3	26″ (66)	1.0″ (2.54)	1.0″ (2.54)	0.742	Untorn
4	26″ (66)	1.0″ (2.54)	2.0″ (5.08)	1.334	Untorn
5	26″ (66)	2.0″ (5.08)	1.0″ (2.54)	0.762	Untorn
6	26″ (66)	2.0″ (5.08)	2.0″ (5.08)	1.087	Untorn
7	36″ (91.4)	1.0″ (2.54)	1.0″ (2.54)	0.923	Untorn
8	36″ (91.4)	1.0″ (2.54)	2.0″ (2.54)	**1.530**	**Heavy tear**
9	36″ (91.4)	1.0″ (2.54)	2.0″ (2.54) w/riser	0.780	
Using coherency temperature integration limit					
8b	36″ (91.4)	1.0″ (2.54)	2.0″ (2.54)	1.589	
9b	36″ (91.4)	1.0″ (2.54)	2.0″ (2.54) w/riser	1.564	

Values in parentheses are in cm.

comparing castings 8 and 9 (which calculate PSD using $f_p^l > 0$ as the start of integration) with castings 8b and 9b (which calculate PSD using $T < T_{coherency}$ as the start of integration). Casting 9 (9b) is the same as casting 8 (8b), except that in the simulation, a riser was placed directly on top of the hot spot where the hot tear forms. Adding this riser should prevent the hot tear, because there is adequate feed metal throughout the solidification of this region. Note that beginning integration when $f_p^l > 0$ (cases 8 and 9), the predicted PSD is much lower with the riser than without, indicating a reduced tendency to hot tear. On the other hand, beginning integration when $T < T_{coherency}$ (cases 8b and 9b), the predicted PSD is essentially unchanged when the riser is added, which is clearly unrealistic. This initial work showed that the PSD model is very promising, as it is clearly sensitive to known hot tear factors.

These simulations of hot tear experiments from the literature pointed to shortcomings in the amount of information available regarding these experiments. First and foremost, the castings were not available, so they could not be radiographed, for example, to detect the presence of internal cracks or very small tears. Additionally, to fully test the model, it is necessary to gather information about the forces and displacements that occur during solidification and cooling; this data was not available. To address the lack of desired data for model testing, new T-shaped casting experiments were devised. A schematic of the experimental set-up is given in Fig. 2. Displacements were measured using linear voltage displacement transducers (LVDT) at the four locations D1 – D4 indicated in Fig. 2. The displacements D1 and D3 were necessary to account for the motion of the mold within the apparatus, so that mold displacement was not included in the displacements measured in D2 and D4. The forces in the ends of the T-section castings were measured with load cells at the locations F1 and F2 indicated in Fig. 2. The castings used in these experiments were 36” long and 1” thick (in the depth direction not visible in Fig. 2). The castings were made from standard cast steel (defined under ASTM A-216), and the molds were furan sand. Complete experimental details are provided in Appendix C.

The hot tear results from these casting experiments are summarized in Table 2. The parameters that were varied were the arm width (E in Fig. 2), the leg width (C in Fig. 2), and the sulfur content. It was found that increasing the sulfur and phosphorus content in the melt (which

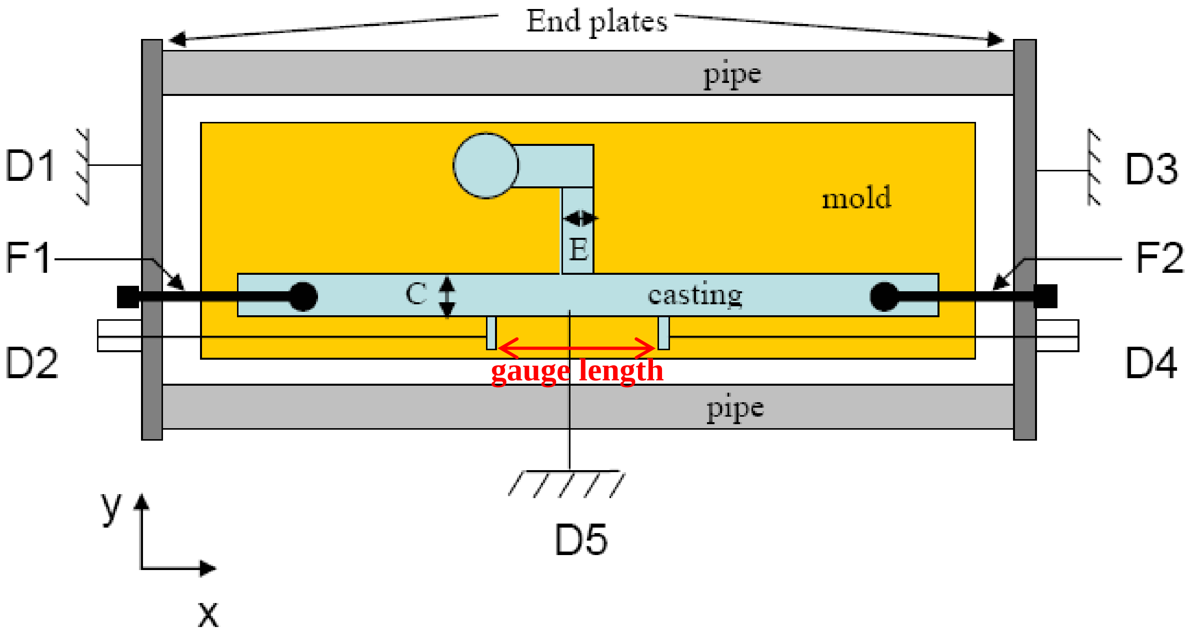

Figure 2. Schematic of the new experimental T-shaped casting set-up, indicating the location of displacement

Table 2. Summary of castings and hot tear results from new casting experiments.

Casting #	Arm	Leg	Composition	Restraint	Tear
1	2"	1"	Low Sulfur	Bolts	None
2	2"	2"	Low Sulfur	Bolts	None
3	1"	1"	Low Sulfur	Bolts	None
4	1"	2"	Low Sulfur	Bolts	None
5	1"	2"	High Sulfur	Bolts	Large Tear
6	2"	2"	High Sulfur	Bolts	Linear Indication
7	1"	2"	High Sulfur	None	None

increases the size of the solidification range) increased the hot tear tendency, as seen by comparing castings 4 and 5 in Table 2. Complete discussion of these experimental results is provided in Appendix C.

Figs. 3 and 4 show the time-dependent displacement and force measurements for casting 5. The displacements shown in Fig. 3 represent the change in the gauge length defined in Fig. 2 (i.e., the gauge displacement), which is the change in the original distance between the two tabs where the displacement measurements D2 and D4 (see Fig. 3) were taken. These results already account for mold motion measured by D1 and D3. The results illustrate how the gauge length increases during solidification. The corresponding force measurements given in Fig. 4 illustrate that the forces begin to build at about the same time that the gauge length begins to increase. The increase of forces above zero indicates the point where the metal has solidified sufficiently to sustain forces. Additional discussion of these results is provided in Appendix C.

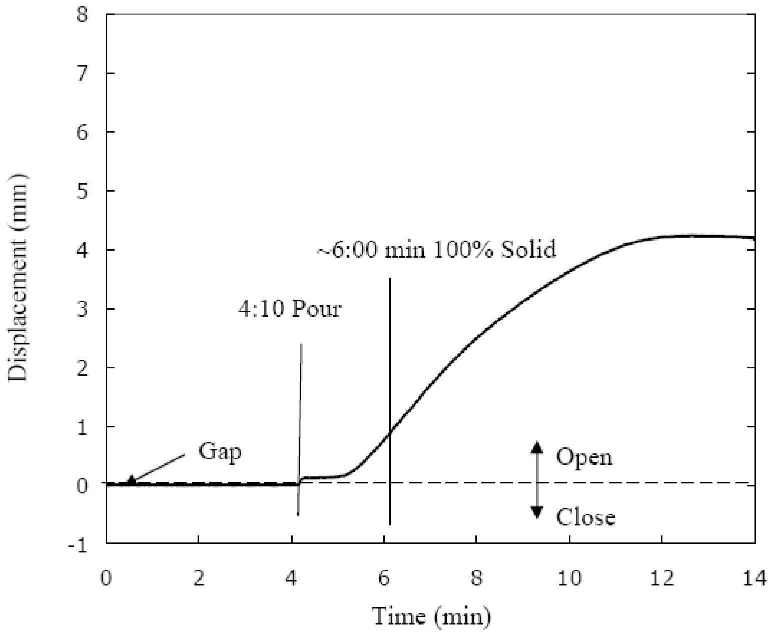

Figure 3. Time-dependent gauge length change for casting 5, calculated from the measured displacements.

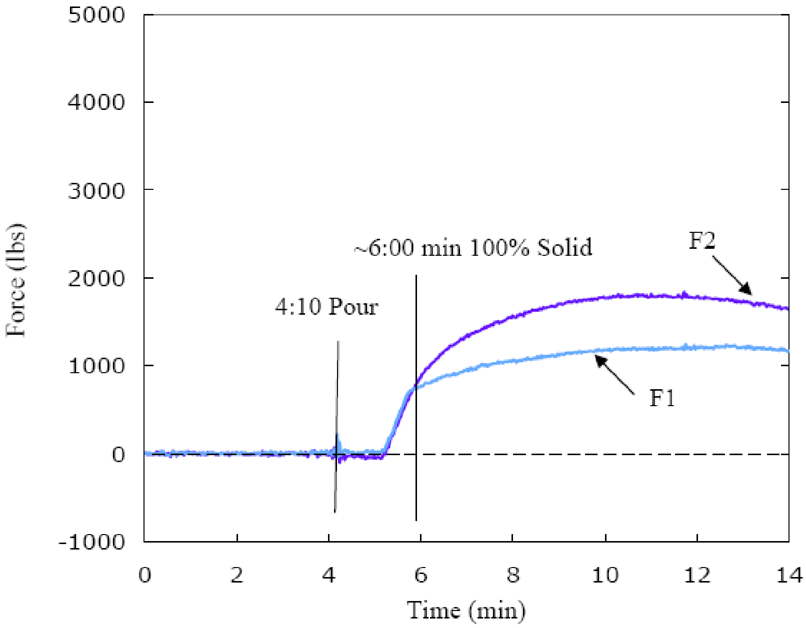

Figure 4. Time-dependent force measurements for casting 5.

In addition to performing the new experiments, simulations were performed for casting 3, in order to test a new material model for the stress simulation. The previous simulation results were performed with a completely elastic material model. For casting 3, this original elastic model was used for one stress simulation, and a new plastic material model was used to perform a second stress simulation. The resulting gauge length and force measurements are presented in Figs. 5 and 6. It is evident from these figures that the elastic simulation significantly under-predicts the change in gauge length and over-predicts the forces. The plastic material model

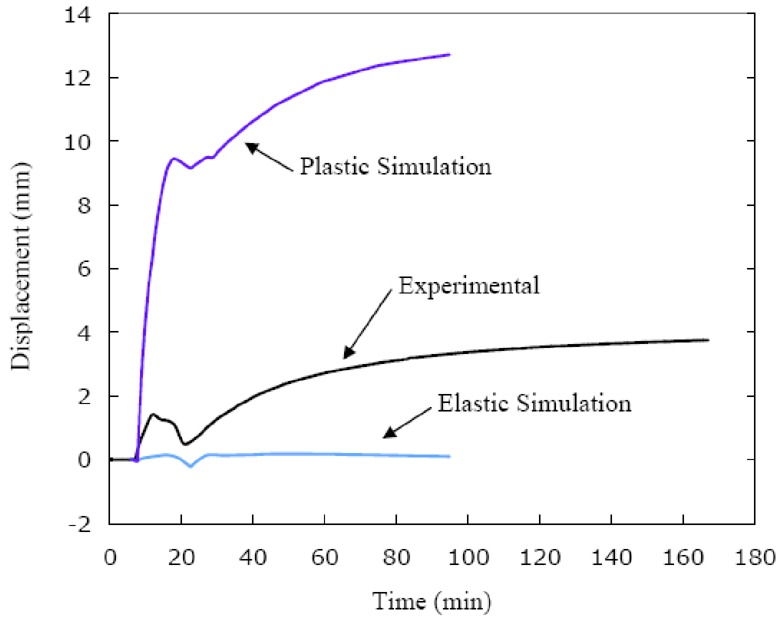

Figure 5. Experimental and simulated changes in gauge length for casting 3.

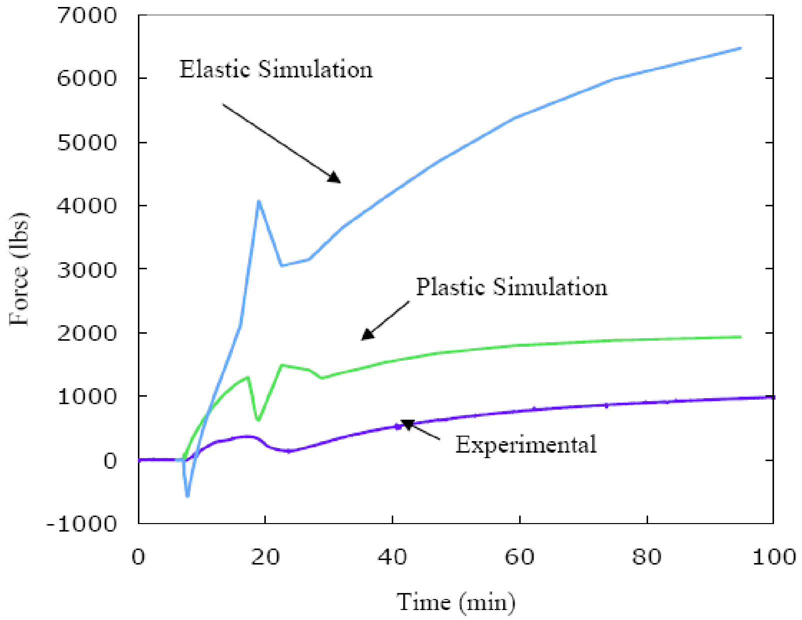

Figure 6. Experimental and simulated force curves for casting 3.

over-predicts both the change in gauge length and the forces. Through further research, it was determined that the plastic material model was a better model, and that the inaccuracy seen in Figs. 5 and 6 was primarily due to inaccurate mechanical properties. See Appendix C for further discussion.

Based on the discrepancies seen between the simulated and measured displacements and forces from the new casting experiments, new mechanical property data models were developed for low alloy steels. This new property data model was developed using a yield stress model that includes strain hardening and strain rate dependence. The mechanical property model equations are provided in Appendix D, along with substantial discussion about the properties. These new properties were utilized in conjunction with a new stress model that includes finite element solution and other new models, notably a new contact model that more accurately models the contact between the solidifying casting and the mold and cores. Using the new stress model and the new material property models, the simulated gauge displacement for casting 7 in Table 2 (the unrestrained casting) is shown in Fig. 7. This figure includes the results of a parametric study wherein the mold stiffness was varied from 1500 MPa to 3000 MPa. Increasing the mold stiffness acts to restrict the shrinkage of the gauge length. Using the final value selected, 2250 MPa, the simulated gauge displacement was in excellent agreement with the measured values. The results of this study indicate that a reasonable model for mold deformation and suitable properties must be included in order to accurately predict casting distortion and hot tearing tendencies. See Appendix D for further details.

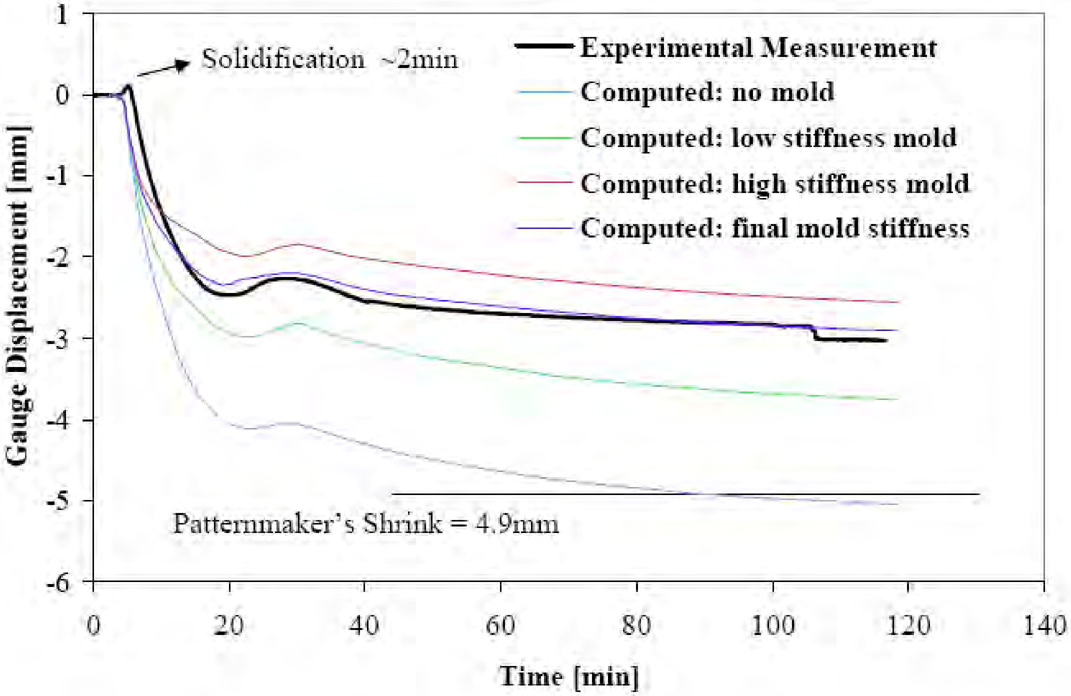

Figure 7. Gap displacement curves comparing casting 3 experimental and simulated results.

Based on all the modeling lessons learned thus far in this research, the PSD model was further refined to its final state. The equations for this final model, based on a visco-plastic constitutive model with damage (i.e., PSD), are given in Appendix E. This final model is implemented in commercial casting and stress analysis software. Comparisons between the measured and predicted gauge displacements for new restrained T-section castings, one with 2” arm/leg dimensions and two with 1” arm/leg dimensions, are shown in Fig. 8. Excellent agreement is seen between the simulated and measured displacements in the 2” arm/leg casting. The agreement is only qualitative for the 1” arm/leg castings, however. It is believed that improvement of the high-temperature mechanical properties used in the simulations is necessary to improve this agreement. A comparison between the damage (PSD) prediction and casting radiographs are provided for the restrained 2” arm/leg casting in Fig. 9. The large crack seen

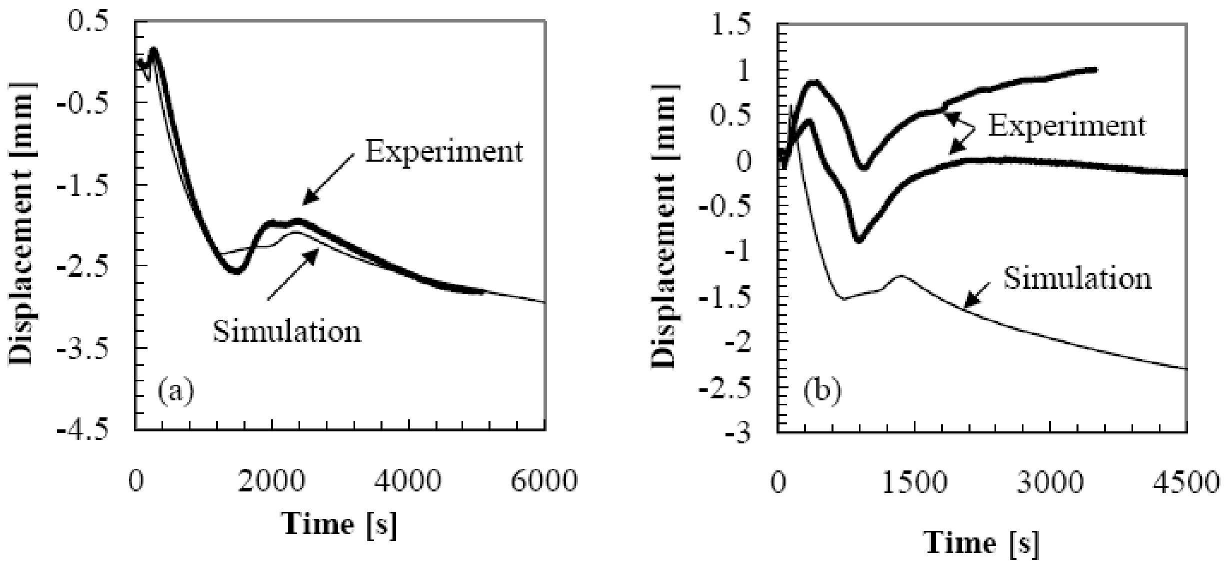

Figure 8. Comparison between measured and predicted gauge displacements for restrained castings; (a) 2” arm/leg; and (b) 1” arm/leg.

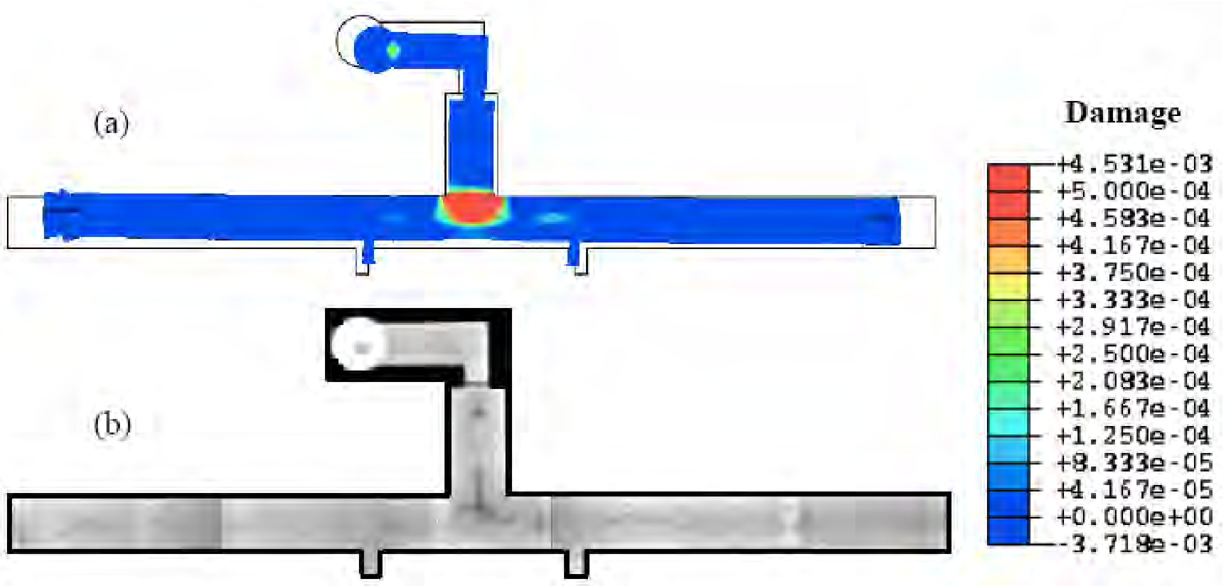

Figure 9. Results for the restrained 2” arm/leg casting: (a) predicted distortions (five times magnified) and damage porosity field; and (b) radiograph of the casting.

along the centerline of the arm is in good agreement with the damage prediction. Additional results and discussion are provided in Appendix E.

Finally, two case studies involving production castings were simulated with the final model. As shown in Fig. 10, good correlation between indications on castings and damage prediction were observed. Further details and comparisons are given in Appendix F.

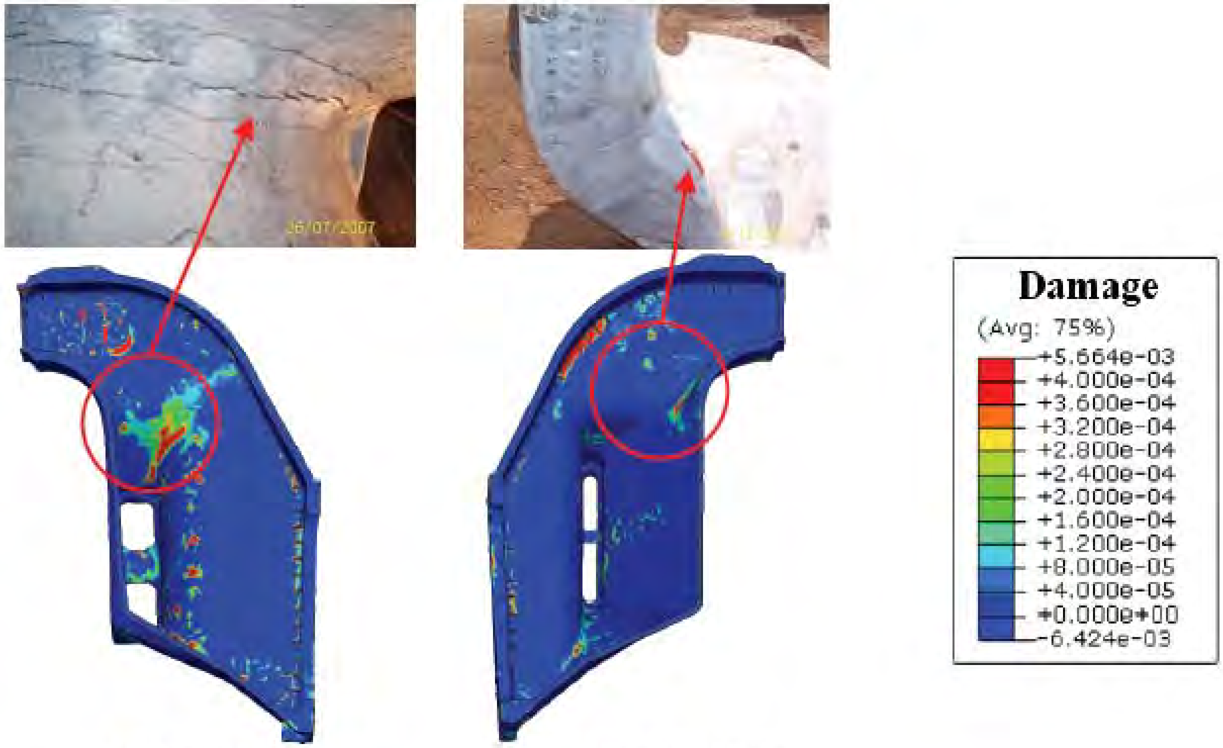

(a) Cope side

(b)Drag side

Figure 10. Hot tears and damage prediction for an industrial casting.

Benefits Assessment

The development of a commercial model to predict dimensional changes and hot tears during solidification of steel castings will provide the steel casting industry with a tool that will result in a reduction of scrapped castings and re-work/repair due to dimensional changes or hot tears, and also an increase in casting yield due to a reduction in the use of padding and improved placement of risers, leading to better riser efficiency. This new technology was predicted to result in an average energy savings of 1.43 trillion BTU's/year over a 10 year period (with full funding). With 86.6% of proposed funding, current (2011) annual energy saving estimates, based on commercial introduction in 2012, a market penetration of 29% by 2020, and 10% reduction in energy usage per year, is 2.15 trillion BTU's/year.

Along with these energy savings, reduction of scrap and improvement in casting yield will result in a reduction of the environmental emissions associated with the melting and pouring of the metal which will be saved as a result of this technology. The average annual estimate of CO_2 reduction per year through 2020 is 0.03 Million Metric Tons of Carbon Equivalent (MM TCE).

Commercialization

As discussed in the Introduction, commercialization of the hot tear/dimensional changes model is a natural outcome of this project, because the models developed for this project were developed within/alongside commercial casting simulation software. The hot tear predictor is in the form of a user subroutine that can be utilized in conjunction with the commercial casting simulation package MAGMAsoft, via the MAGMAsoft API (applications programming interface). The final visco-plastic stress model with damage is implemented using the commercial software package ABAQUS. In addition, technology transfer occurred in the form of the publication of papers describing the hot tear/dimensional changes model, which are available in conference proceedings and journals (see Appendices A – F).

Accomplishments

A model to simulate hot tears and dimensional changes during casting solidification has been successfully developed and implemented in commercial casting simulation software. Hot tear experiments have also been performed, expanding the available experimental database on this topic. This model advances the state-of-the-art in the prediction of hot tears and dimensional changes. As an added benefit of the commercialization of this project, the hot tear/dimensional changes model has also been successfully applied outside of the steel industry, to predict hot tears and dimensional changes in squeeze cast magnesium alloy control arms.

The work detailed in this report resulted in the publication of one journal article (given in Appendix B) and five papers available in technical conference proceedings (given in Appendices A and C – F). This research also resulted in a doctoral dissertation (Charles Monroe, 2004, "Development of a Hot Tear Indicator for Use in Casting Simulation").

Conclusions

A model that predicts hot tears and dimensional changes during steel casting solidification has been successfully developed and implemented in commercial casting and stress analysis software. This model is based on a visco-plastic constitutive model with damage, where the damage begins to form when feed metal is cut off to a solidifying region. The hot tear prediction is a locater for hot tear initiation sites, and not a full tear prediction: casting regions with relatively high damage values indicate where a casting is more likely to tear. In both experimental castings and industrial production castings, regions of high damage were seen to correlate reasonably well with hot tear locations. The predictive capability of the model will improve with the development of more accurate high-temperature mechanical properties. This model provides the steel casting industry with a tool that will result in a reduction of scrapped castings and re-work/repair due to dimensional changes or hot tears, and also an increase in casting yield due to a reduction in the use of padding and improved placement of risers, leading to better riser efficiency. This new technology is expected to result in an estimated energy savings of 2.44 trillion BTU's/year. Along with these energy savings, reduction of scrap and improvement in casting yield will result in a reduction of the environmental emissions associated with the melting and pouring of the metal which will be saved as a result of this technology.

Recommendations

During the course of the development of the model that predicts hot tears and dimensional changes during steel casting solidification, it has become apparent that the mechanical properties of both the steel and the sand, required for stress simulation, are very important. Accurate predictions with this model require accurate properties. The constitutive model for the mechanical properties of low alloy steel developed in the course of this research significantly improved the model's predictions. The predictive capability of the model will improve further with the development of more accurate high-temperature mechanical properties.

References

[1] H. Hiebler, C. Bernhard, *Steel Res.*, vol 70, 1999, 349–355.

[2] K. Nakayama, M. Kinefuchi, K. Tsutsumi, in: B.G. Thomas, C. Beckermann (Eds.), Modeling of Casting, Welding and Advanced Solidification Processes, vol. VIII, Warrendale, PA, 1998.

[3] M. Rappaz, J.-M. Drezet, M. Gremaud, *Metall. Mater. Trans. A*, vol. 30A, 1999, pp. 449–455.

[4] A. Mo, M. M'Hamdi, H.G. Fjaer, in: D.M. Stefanescu, J.A. Warren, M.R. Jolly, M.J.M. Krane (Eds.), Modeling of Casting, Welding and Advanced Solidification Processes, vol. X, Warrendale, PA, 2003, pp. 199–206.

[5] C.W. Briggs, Steel Founders' Society of America Research Report, No. 38, Technical Research Committee, SFSA, Crystal Lake, IL, 1957.

Appendices

The appendices include all the papers that were written based on the research performed for this project.

Appendix A: "Development of a Hot Tear Indicator for Use in Casting Simulation," a paper by C. Monroe and C. Beckermann in Proceedings of the 58th SFSA Technical and Operating Conference, 2004.

Appendix B: "Development of a Hot Tear Indicator for Steel Castings," a paper by C. Monroe and C. Beckermann in *Materials Science and Engineering A*, 2005.

Appendix C: "Simulation of Hot Tearing and Distortion during Casting of Steel: Comparison with Experiments," a paper by C. Monroe and C. Beckermann in Proceedings of the 60th SFSA Technical and Operating Conference, 2006.

Appendix D: "Deformation during Casting of Steel: Model and Material Properties," a paper by C. Monroe and C. Beckermann in Proceedings of the 61st SFSA Technical and Operating Conference, 2007.

Appendix E: "Simulation of Deformation and Hot Tear Formation Using a Visco-Plastic Model with Damage," a paper by C. Monroe, C. Beckermann and J. Klinkhammer in Modeling of Casting, Welding, and Advanced Solidification Processes – XII, 2009.

Appendix F: "Prediction of Hot Tear Defects in Steel Castings Using a Damage Based Model," a paper by Z. Lin, C. Monroe, R. Huff and C. Beckermann in Modeling of Casting, Welding, and Advanced Solidification Processes – XII, 2009.

Monroe, C., and Beckermann, C., "Development of a Hot Tear Indicator for Use in Casting Simulation," in Proceedings of the 58th SFSA Technical and Operating Conference, Paper No. 3.1, Steel Founders' Society of America, Chicago, IL, 2004.

Development of a Hot Tear Indicator for Use in Casting Simulation

C. Monroe
C. Beckermann
Department of Mechanical and Industrial Engineering
The University of Iowa, Iowa City, IA 52242

Abstract

A hot tear indicator based on the physics of solidification and deformaion is presented. This indicator is derived using available data from computer simulation of solidification and solid deformation. Hot tears form when the mushy zone is starved of liquid feeding and deformed in tension. The unfed tensile deformation causes a small additional porosity. A physical model based on mass balance is developed to find the additional porosity formed. This additional porosity or porosity due to solid deformation (PSD) is a locator for initiation sites for hot tears in the casting, not a full tear prediction. By evaluating this quantity on the whole geometry, an indicator consistent with physical intuition and past experimental results is found. Using a simulation study of hot tear castings developed in SFSA literature, conclusions are drawn about the usefulness of this indicator. In summary, reducing the strain in the casting, increasing the feeding of the section, decreasing the carbon content from 0.3% to 0.15%, decreasing the sulfur and phosphorus content from 0.08% combined to 0.02%, and eliminating core restraint all decrease the hot tear tendency.

Introduction

Once hot tears occur in steel castings, they must be fixed by welding or the casting must be scrapped. Considerable effort is spent to eliminate hot tears from castings. Hot tears are identified as cracks, either on the surface or internally in the casting. These cracks may be large and visible to the naked eye or small and found only by magnetic particle inspection. A valve casting shown in figure 1 is an example of a dramatic hot tear. They are caused by a combination of thermal effects, such as hot spot size, and casting restraint, such as cores in cylindrical castings [1]. In addition, composition can affect hot tearing tendency [2]. Physically, two factors contribute to hot tearing in the mushy zone. Hot tears are formed when the mushy zone is (a) cutoff from liquid feeding and is (b) under tensile loading [3].

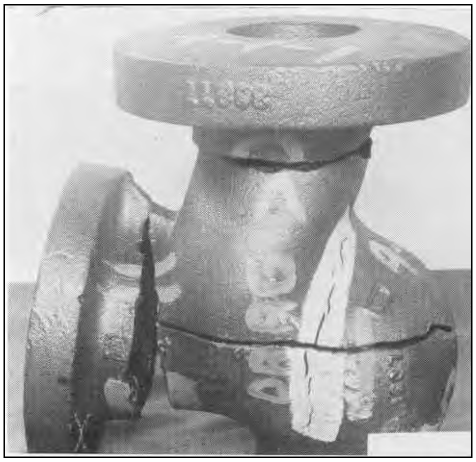

Figure 1 Dramatic Hot Tear Example [5].

Liquid feeding is caused because the material contracts upon solidification. This reduction in volume will create a pressure drop causing liquid feeding through suction. However, feeding may be cutoff because the solidified dendritic network may prevent flow; then porosity will form. Porosity formation signals that the liquid feeding is cutoff.

In addition to causing porosity during solidification, thermal contraction of the solid also causes deformation that creates hot tears. Thermal gradients from non-uniform cooling cause mechanical strains.

These strains create tensile or compressive stresses. Although each solid or liquid phase is incompressible, the mixture is compressible [4]. In compression, liquid is squeezed out. In tension, liquid may be sucked in. However if liquid is not available under tensile loading additional porosity may form. This porosity forms late in solidification along grain boundaries. This porosity is the initiation site for hot tears and is referred to as porosity due to solid deformation (PSD).

Experimental work done by the Steel Founders' Society of America is reported in Research Report #38. By changing casting lengths and section sizes, this report was able to test the effect of variation of hot spot size and strain on hot tears. This report concluded hot tears could be avoided by using filleted corners, smaller section size transitions, and an unrestrained casting and gating layout [5]. These methods enhance liquid feeding and reduce the tensile strain in the casting. Further work also demonstrated that chills and material composition have an effect on hot tearing tendency [1].

Phenomenological models of hot tearing in castings have been developed in the past. Features of these models are discussed in Rappaz et. al. [3]. However, Rappaz et. al. have gone a step further than the phenomenological modeling. Their RDG criterion is derived using a mass balance on a solidifying mushy zone. The authors solve for maximum sustainable strain rate. This is the strain rate beyond which cavitation, or porosity formation, occurs. The paper showed that this criterion agrees with typical "Λ curves" from phenomenological models and some experimental results. The "Λ curves" is a graph of hot tear criteria and composition. The peak occurs close to the maximum freezing range of that alloy. This model is developed using a one-dimensional control volume, which is not immediately applicable to three-dimensional situations. The RDG criterion also is sensitive to the definition of coherency temperature, i.e. temperature when the dentritic network can transmit stresses. In continuous casting, this criterion may be useful because the strain rate is directly related to the velocity of a symmetric casting. However, in shaped casting this criterion is not directly applicable.

In another model, Mo et. al. simultaneously solves the energy, liquid and solid momentum, and continuity equations. Using a method similar to RDG criterion, a hot tear criterion based on the liquid pressure drop is used [6]. However, this method also has limitations because porosity formation is not considered. The authors demonstrate the sensitivity of the liquid pressure drop to strain rate, solid to liquid velocity coupling, solid constitutive equations, etc.

In the following section, the method for obtaining the porosity due to solid deformation is developed. After the method is introduced, "T" section and cone castings from SFSA research reports are simulated. These simulations are compared to the experimental results. Also, the effect of feeding a hot spot and material composition on hot tearing is shown.

Method

The motivation for the method proposed here arises due to the available modules of MAGMAsoft. The modules used include MAGMAsoft porosity module, MAGMAstress, and MAGMAsoft API. The MAGMAsoft porosity module developed by Carlson et. al. calculates the temperature, liquid velocity, and porosity formation in solidifying casting geometries [7]. Note that in the MAGMAsoft porosity module the solid is assumed to be stationary. Then using the temperature results, MAGMAstress predicts the deformation and stress in a solidifying casting. Because MAGMAstress must be run after the MAGMAsoft porosity module, the solid velocity is not available in the solution of the liquid velocities, porosity formation, etc. In order to find hot tears, information from both MAGMAsoft porosity module and MAGMAstress must be used together. MAGMAsoft API module is a C programming language interface extracts data from and creates MAGMAsoft postprocessor files. Using MAGMAsoft API, data from MAGMAsoft porosity module and MAGMAstress can be used to create a hot tear indicator.

As previously noted, hot tears form when the mushy zone is cut off from liquid feeding and is deformed in tension. Similarly, microporosity and some macroporosity form when solidification shrinkage cannot be fed by liquid through the mushy zone. Therefore, hot tears begin as additional porosity formed in excess of the porosity formed with no solid movement. The various contributions to porosity in solidification are found using the continuity equation. The volume averaged multi-phase model under consideration assumes that three phases exist. The three phases considered are the solid metal (*s*), liquid metal (*l*), and porosity (*p*), such that $f_s + f_l + f_p = 1$. The statement of continuity or mass balance for the three-phase system is

$$\frac{\partial}{\partial t}\left(f_s\rho_s + f_l\rho_l + f_p\rho_p\right) + \nabla\cdot\left(f_s\rho_s\mathbf{v}_s + f_l\rho_l\mathbf{v}_l + f_p\rho_p\mathbf{v}_p\right) = 0 \tag{1}$$

where t, f, ρ, and $\boldsymbol{v}$ are the time, phase fraction, density, and velocity respectively. This equation states that the time rate of change of the mass per unit volume of each phase is equal to the flux of mass per unit volume of each phase in and out of the control volume.

Because the solid deformation is solved separately, the effect of the solid velocity on the continuity equation is not known. One way to estimate this effect is to assume that solid deformation will create or destroy porosity. Under this assumption, the pore fraction can be split into two components, or

$$f_p = f_p^l + f_p^s. \tag{2}$$

The first component, f_p^l, is referred to as porosity or original porosity and includes contributions of solidification shrinkage, liquid mass flux, etc. The second component, f_p^s, is referred to as additional porosity or porosity due to the solid deformation (PSD).

Substitute these two porosity fractions from eq. (2) into eq. (1). Neglect the mass flux of the porosity, $f_p\rho_p\mathbf{v}_p = 0$, because the density of the porosity is several orders of magnitude less than the solid and liquid density. Rearrange the continuity equation in order to identify the contributions; then eq. (1) becomes

$$\underbrace{\left[\frac{\partial}{\partial t}\left(f_s\left(\rho_s - \rho_l\right) + \rho_l + f_p^l\left(\rho_p - \rho_l\right)\right) + \nabla\cdot\left(f_l\rho_l\mathbf{v}_l\right)\right]}_{\text{A}} + \underbrace{\left[\frac{\partial}{\partial t}\left(f_p^s\left(\rho_p - \rho_l\right)\right) + \nabla\cdot\left(f_s\rho_s\mathbf{v}_s\right)\right]}_{\text{B}} = 0. \tag{3}$$

The MAGMAsoft porosity module solves part A of eq. (3) equal to zero. Part A is the continuity equation if the solid phase is assumed to be stationary. If the solid is stationary then the continuity equation is a balance of the solidification shrinkage, liquid density changes, porosity formation (f_p^l), and liquid mass flux. If part A is zero, then part B must also equal zero. Part B represents a balance between the additional porosity (f_p^s) and the solid mass flux. Again, setting each part equal to zero means that the liquid velocity of part A is uninfluenced by the solid velocity in part B, i.e. solid deformation cannot squeeze out or pull in liquid.

In eq. (3), set part A equal to zero. Also assume that the pore density is negligible in comparison to the liquid density and assume that the liquid density is a constant equal to the density at liquidus. Then, solving for the time rate of change in PSD yields

$$\frac{\partial}{\partial t}\left(f_p^s\right) = \frac{1}{\rho_l}\nabla\cdot\left(f_s\rho_s\mathbf{v}_s\right) \tag{4}$$

This equation must be integrated to find the porosity due to solid deformation. The integration limits are found by noting the events that happen as hot tears form. First, hot tears form when liquid feeding is cut off from the mushy zone. So the start of the integration is set to the instant when porosity increases from zero, or $f_p^l > 0$. Second, all solid deformation may not contribute to creation of PSD. Once the material is completely solid then PSD formation stops and all of the mechanical properties become important. Then crack growth and propagation become the dominate hot tear mechanisms. Therefore, the solidus temperature is used as an estimation of the temperature when the mushy zone develops adequate strength to resist PSD formation, or $T < T_S$. Integrating eq. (4) using these integration limits, the equation for PSD is

$$\text{PSD} = f_p^s = \frac{1}{\rho_l} \int_{f_p^l > 0}^{T < T_s} \left(\boldsymbol{v}_s \cdot \nabla \left(f_s \rho_s \right) + f_s \rho_s \nabla \cdot \left(\boldsymbol{v}_s \right) \right) dt \,. \tag{5}$$

For eq. (5), MAGMAsoft porosity module provides results for the temperature, porosity fraction (f_p^l), liquid density, solid fraction, and solid density. However, the solid velocity must be obtained from MAGMAstress. The MAGMAstress module uses a simple temperature dependent elastic-plastic mechanical model for a solidifying metal. However even with a simple mechanical model, it is believed that the thermal strains are useable. The thermal strains are given by the thermal expansion / contraction coefficient and the temperature field. Thermal strain drives the deformation in hot tearing.

Two terms are needed from MAGMAstress in eq. (5). The first is the solid velocity, which is multiplied by the gradient of the solid fraction and the solid density. Note that the gradient of the solid fraction and solid density is small and could be neglected. The solid velocity is found by dividing the change of the displacement, $\boldsymbol{u}$, by the time step, or

$$\boldsymbol{v}_s = \frac{\Delta \boldsymbol{u}}{\Delta t} \,. \tag{6}$$

Second term needed from MAGMAstress is the divergence of the solid velocity. The divergence of the solid velocity is the sum of the normal strain rate components and can be expressed as

$$\nabla \cdot \left(\boldsymbol{v}_s \right) = \text{trace}\left(\dot{\boldsymbol{\varepsilon}} \right) = \dot{\varepsilon}_{xx} + \dot{\varepsilon}_{yy} + \dot{\varepsilon}_{zz} \,. \tag{7}$$

The procedure to solve for PSD is completed in three steps. First, run the MAGMAsoft porosity module to solve for the temperature, porosity fraction, liquid density, solid fraction, and solid density. Then using the temperature results, run MAGMAstress to find the displacement and normal strain rate. Finally using MAGMAsoft API, gather these results, calculate PSD from eq. (5), and write new post-processing results showing the value of PSD on the geometry. Comparison of PSD with experimental hot tear results will be examined in the following sections.

Note that this indicator does not predict crack growth. The appearance of crack may change the course of stress development. For example, if a site that forms early tears then the stress will be relieved. Other sites may not appear at all if the casting tears. In the following analysis, the indications in the area known to tear will be ranked by the greatest PSD. This of course is not a definitive answer to whether a particular casting will tear or not. However, this will yield information as to whether or not this indicator gives physically reasonable results.

“T” section Casting

Simulation Setup

The test castings chosen for this study were based on Research Reports #38 [5] and #103 [8]. The following figure 2 shows some example castings of the proposed “T” section geometry. Thirteen “T” section castings are simulated with the following changes in the geometry and composition. Lengthening the arm will increase the amount of strain on the hot spot. Here, either 26” or 36” arm lengths are used as shown on figure 2. Increasing the arm width, dimension ‘C’ on figure 2, will increase the strength of the arm by providing more material to tear. The arm width is increased from 0.5” to 1.0” and then to 2.0” wide. Increasing the leg width, dimension ‘E’ on figure 2, will increase the hot spot size at the section transition. The leg width increased from 1.0” to 2.0” wide. Note that all of the castings have a thickness of 1.0”. All of the simulations are summarized in Table 1. In addition to eight simulations to test the effect of geometry effects, five simulations are run to show the effect of feeding and composition on hot tearing tendency. To show the effect of feeding on hot tearing, a riser is placed on top of the 2” wide leg section of the casting that has a 36” arm length and 1” arm width. Without the riser this casting is this is identical to simulation 8. Simulations 10 – 12 test the effect of composition on hot tearing. This is accomplished by using extreme compositions of a WCB alloy.

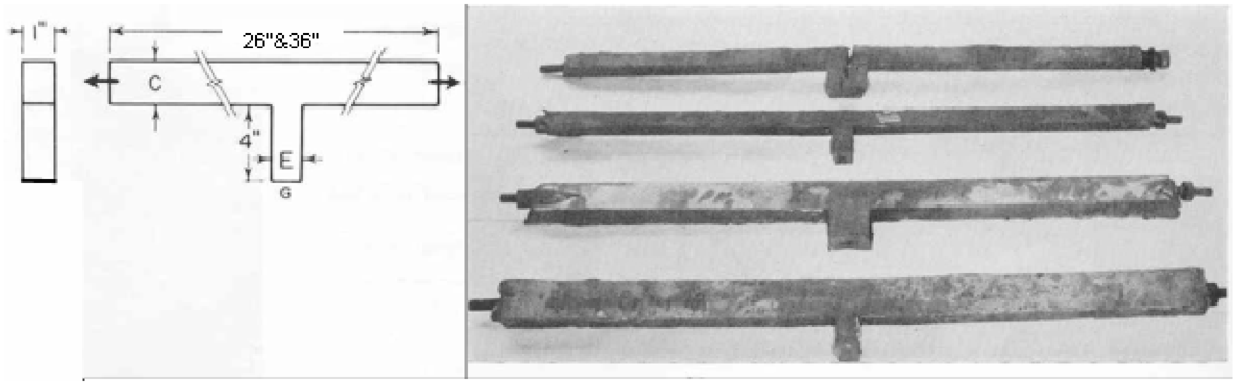

Figure 2 Example of "T" section casting [5].

Table 1 Geometric Simulation Setup

Simulation #	Arm Length	Arm Width Dim. ‘C’	Leg Width Dim. ‘E’	Composition of Carbon and Sulfur + Phosphorus%
1	26”	0.5”	1.0”	C 0.23% and S+P 0.044%
2	26”	0.5”	2.0”	C 0.23% and S+P 0.044%
3	26”	1.0”	1.0”	C 0.23% and S+P 0.044%
4	26”	1.0”	2.0”	C 0.23% and S+P 0.044%
5	26”	2.0”	1.0”	C 0.23% and S+P 0.044%
6	26”	2.0”	2.0”	C 0.23% and S+P 0.044%
7	36”	1.0”	1.0”	C 0.23% and S+P 0.044%
8	36”	1.0”	2.0”	C 0.23% and S+P 0.044%
9	36”	1.0”	2.0” w/ Riser	C 0.23% and S+P 0.044%
10	Same Geometry as Simulation # 8			C 0.3% and S+P 0.08%
11	Same Geometry as Simulation # 8			C 0.15% and S+P 0.08%
12	Same Geometry as Simulation # 8			C 0.3% and S+P 0.02%

In the Research Report #38, the composition of the steel for the castings was carbon 0.23%, silicon 0.5%, manganese 0.6%, sulfur 0.028%, and phosphorus 0.016%. This was the composition used in simulations 1-8. The compositions for the final four simulations were chosen to represent a WCB alloy with extreme levels of carbon, sulfur, and phosphorus. Carbon is varied from 0.3% to 0.15%. Sulfur and Phosphorus is added together and varied from 0.08% to 0.02%. The other constituents of the WCB alloy were obtained from the ASM Worldwide Guide to Equivalent Irons and Steels, 4th edition, 2000. All the material properties, except the yield strength, elastic modulus, Poisson ratio, and hardening coefficient were obtained using IDS Solidification Analysis Package, version 1.3.2. The properties that took exception were obtained from extrapolating MAGMAsoft database information. The variation of composition is summarized in Table 1.

The gating was constant for all cases; it consisted of a small riser 2” in diameter connected by a runner that was 0.5” thick and 1” wide. In the simulation, the ends of the bar were restrained by a mechanical boundary condition of zero displacement and the leg and gating system are not restrained. Figure 3 shows the simulation geometry for three 36” arm length simulations 7-9, gating included. Filling is not simulated; instead the entire casting is initialized above the liquidus at 1600 ^{o}C. The results were all generated using the commercial code MAGMAsoft.

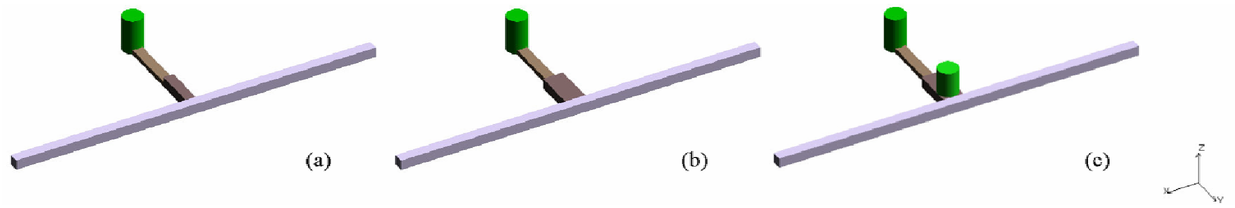

Figure 3 Simulation casting and gating for 36” bar length at (a) 1.0”, (b) 2.0”, (c) 2.0” with Riser.

Grid and Time Step Independence

All of the reported results were run at ~150,000 cells in the casting geometry. Additional simulations at ~40,000 cells in the casting geometry were run on the “T” section casting to demonstrate the grid independence of the results. Figure 4 shows the comparison of 40,000 cells to 150,000 cells. This figure shows the PSD average for each simulation. The average PSD was calculated by summing the total amount of void space generated by PSD and dividing by the space occupied by PSD. To filter out small values of PSD that would dilute the average, a minimum cut off of 0.5% PSD was used.

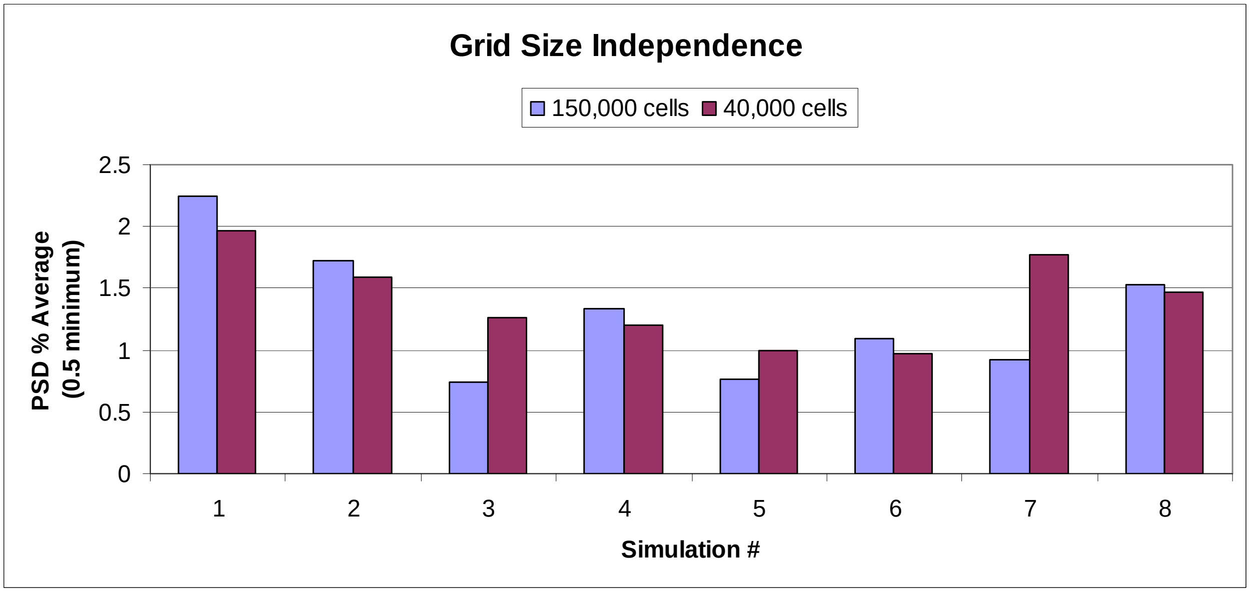

Figure 4 Comparison of Two Grids for simulations 1-8.

Notice that in two cases, simulation 3 and 7, the change in grid size makes significant difference. The strain field between the 40,000 cells and 150,000 cells in these two cases are different and causes the change in average PSD. However, in the rest of the reported cases the results are independent. This demonstrates that a fine grid is important when solving for PSD.

Also additional simulations were run to demonstrate time step independence. Simulation 8 with 150,000 cells was used to test other effects such as feeding and composition and chosen here to run the time step independence study on. Three different time steps were run including 5, 1, and 0.5 seconds. The results are shown in figure 5. These results appear to be independent of time step.

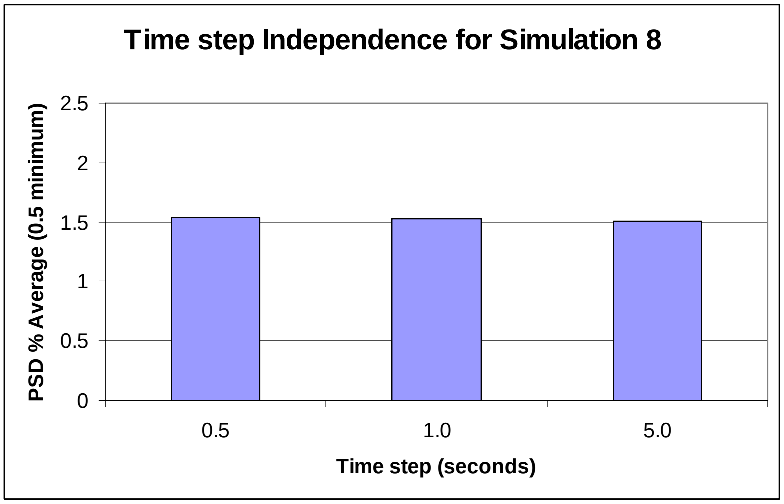

Figure 5 Time Step Independence for simulation 8.

Results

As expected, the section is approximately isothermal across the thin 1" sections. Therefore the temperature gradient is aligned with the straining direction of interest. An example of the fully solid temperature profile is illustrated in Figure 6 for simulation 8. The gating freezes off in ~50 seconds. In all cases the majority of the bar is solidified in ~100 seconds. The entire casting solidified in ~230-250 seconds. Strain is concentrated to the hot spot region because it has the highest temperature and therefore the least resistance to deformation.

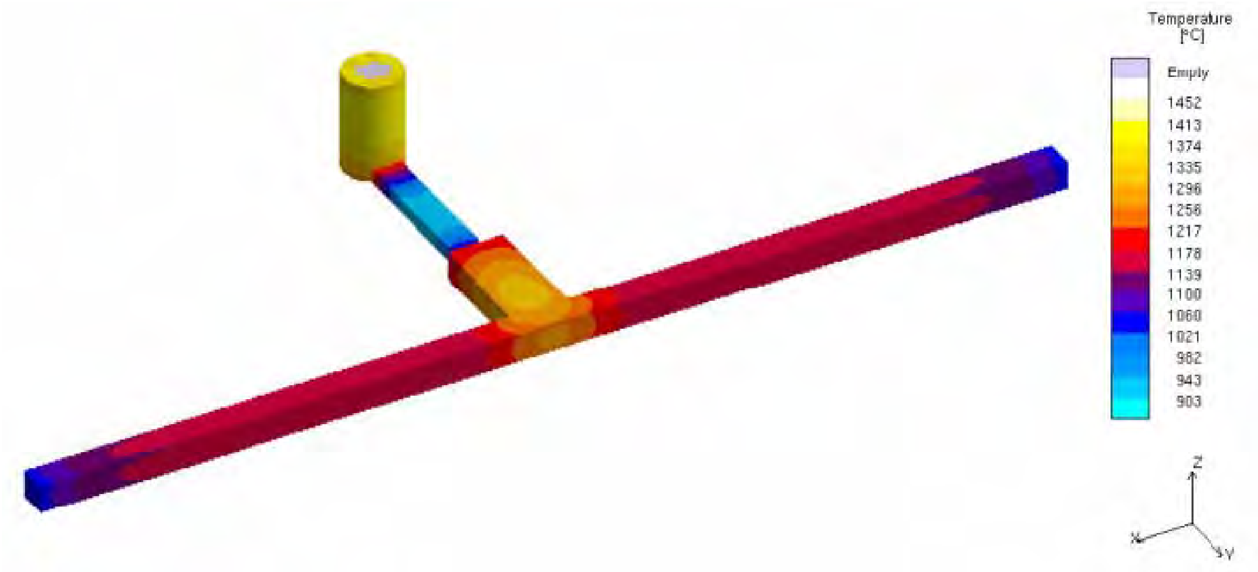

Figure 6 Temperature gradient at 100% solidified.

The amount of porosity due to solidification shrinkage and liquid flows, f_p^l, in the casting was calculated using the porosity module developed by Carlson et. al. [7]. The distribution of porosity in the casting is shown in Figure 7. The scale is from 0-100%. Although not shown here, the Niyama indications confirm that there will be centerline porosity.

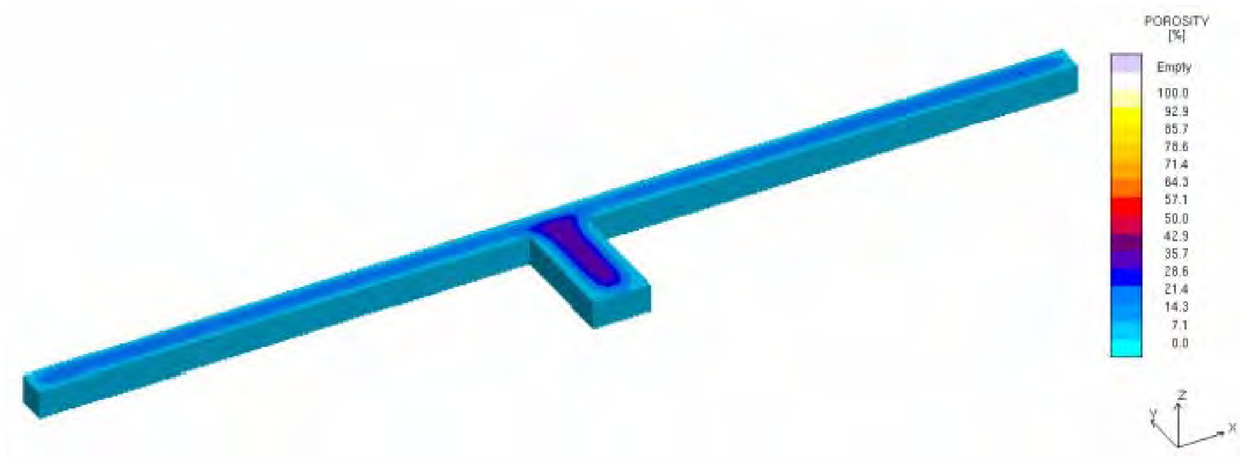

Figure 7 Porosity due to Solidification Shrinkage and Liquid Flows.

Geometry Effects

The porosity due to solid deformation (PSD), f_p^s, is a measure the creation of initiation sites for cracks. In the test casting, most of the PSD occurs at the hot spot. In order to characterize each simulation an average PSD value will be used. The average was calculated by finding the volume of the PSD in the casting and dividing by the volume of the cells that the PSD occupies. In order to filter out small values of PSD, every PSD location above a 0.5% minimum is used.

Table 2 shows the results of the “T” section simulations and prior experimental work. The three castings that showed actual tears are also the simulations with the greatest average PSD. Assuming that PSD acts as a stress concentration, further investigation could be made to associate particular PSD values to crack initiation at various stress levels. This is a promising result showing the use of the PSD indicator. Figure 8 shows two castings from the prior experimental results corresponding to simulations 7 and 8. In the experimental results, simulation 8 tears while simulation 7 does not. Figure 9 shows the PSD for simulations 7 and 8. This figure is an isometric, x-ray view showing indications of PSD that are 0.5% and greater, also cut at mid-plane. The scale in the figure is 0.0% - 6.0% PSD.

Table 2 Summary of results for “T” section Castings.

Simulation #	Arm Length	Arm Width Dim. ‘C’	Leg Width Dim. ‘E’	PSD Ave. (min 0.5%)	Casting Trials [5]
1	26”	0.5”	1.0”	**2.247%**	**Heavy Tear**
2	26”	0.5”	2.0”	**1.724%**	**Multiple Tears**
3	26”	1.0”	1.0”	0.742%	Untorn
4	26”	1.0”	2.0”	1.334%	Untorn
5	26”	2.0”	1.0”	0.762%	Untorn
6	26”	2.0”	2.0”	1.087%	Untorn
7	36”	1.0”	1.0”	0.923%	Untorn
8	36”	1.0”	2.0”	**1.530%**	**Heavy Tear**

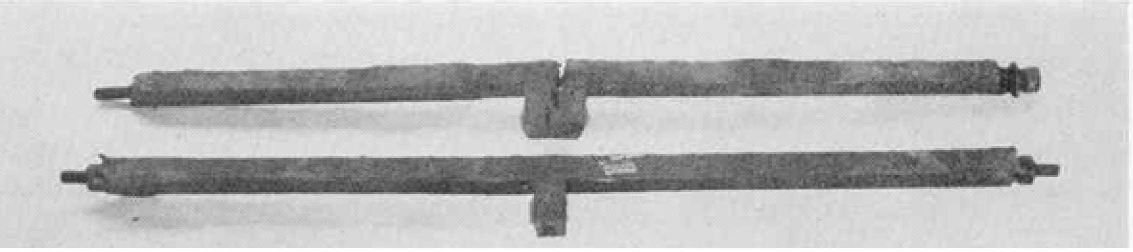

Figure 8 Experimental Results of 36” arm length and 1.0” arm width with 2.0” (top) and 1.0” (bottom) legs [5].

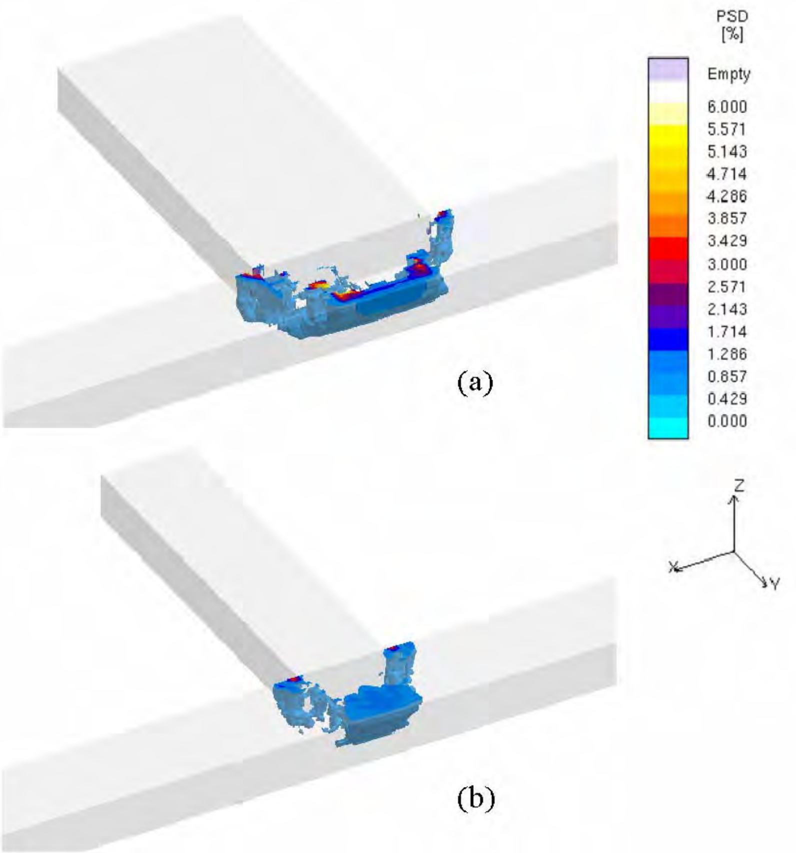

Figure 9 Simulation results of 36” arm length and 1.0” arm width with 2.0” (a) and 1.0” (b) legs. X-ray view showing 0.5% PSD and greater cut at z midplane.

Feeding Effects

Simulations 8 and 9 show the relationship of PSD to feeding effects. In simulation 9, a riser is added on top of the 2.0” leg width. Here two PSD calculations are made. The first is the same as the originally developed PSD. The second PSD changes the integration from the start of porosity formation to a coherency temperature, or from $f_p^l > 0$ to $T < T_{coherent}$. Coherency temperature is the temperature where the solid dendritic network will transmit stresses. Here the temperature at 0.82 solid fraction is chosen based on discussion in Rappaz et. al. [10]. Table 4 shows the results for the two PSD calculations. Figure 10 shows the PSD for simulation 8 and 9 illustrating the use of the original integration limits and the coherency temperature integration limit. The figure shows a mid-plane cut and an x-ray view of the geometry, the visible areas are 0.5% and greater PSD. The scale in Figure 10 is from 0.0% -

6.0% PSD. Notice the change in the average PSD from the original integration limit to the coherency temperature integration limit.

Table 3 Feeding Effect – Simulation 8 and 9 results

Simulation #	Average PSD ($f_p^l > 0$)	Average PSD ($T < T_{coherent}$)
8	1.530%	1.589%
9	0.780%	1.564%

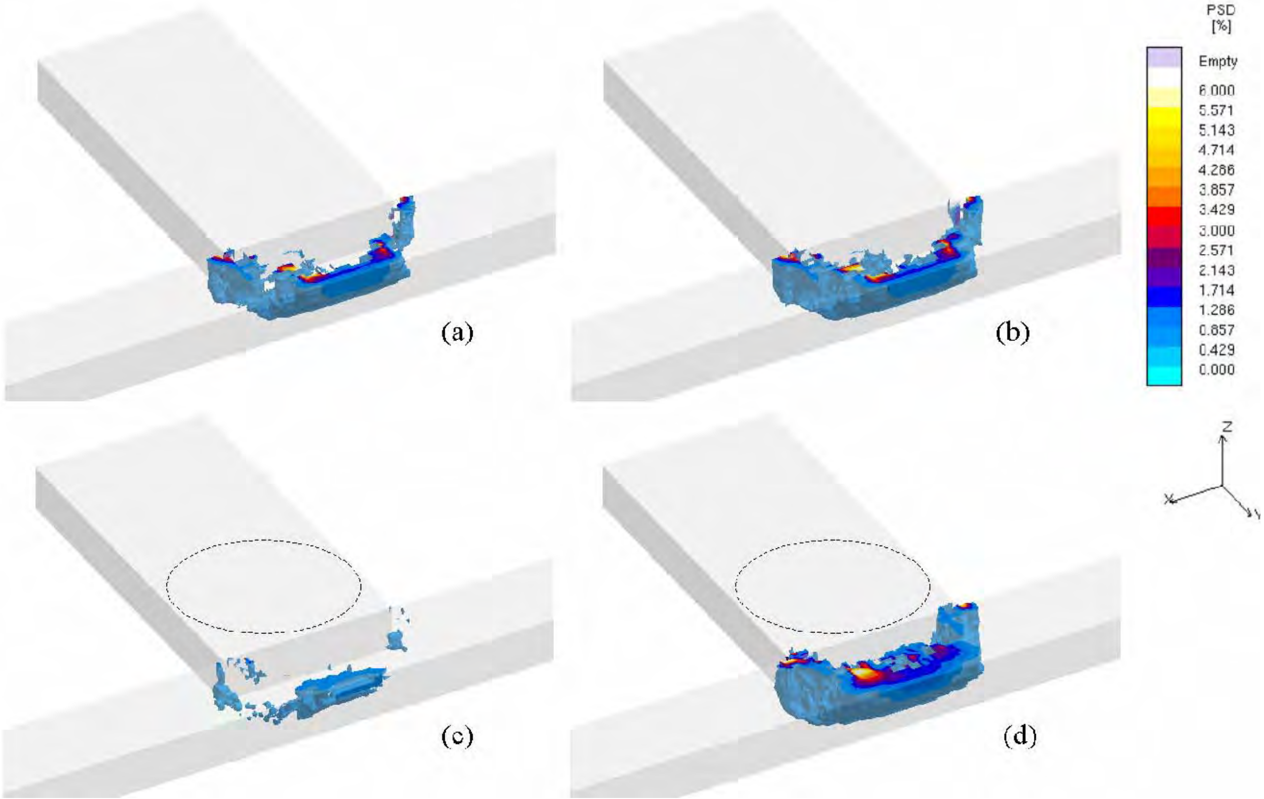

Figure 10 Simulation 8 (top) and 9 (bottom) showing original PSD (a) and (c) and modified PSD (b) and (d). X-ray view showing 0.5% PSD and greater, cut at z midplane.

Compositional Effects

Compositional changes are also known to affect hot tearing by increasing / decreasing the solidification interval. An increase in the solidification interval lengthens the time that the hot spot region is weak. In particular additional carbon, sulfur, and phosphorus should increase the hot tearing tendency. Using some extreme values in WCB steel, this effect can be shown. Table 5 summarizes these results. Note that the value of average PSD in simulation 8 and 10 is indistinguishable. The increase of carbon from 0.15% to 0.3% increases the average PSD a small amount from 1.459% to 1.521%. Increasing the sulfur and phosphorus content from 0.02% to 0.08% increases the PSD more significantly from 1.292% to 1.521%. These results confirm the prior understanding of the influence of composition on hot tears.

Table 4 Composition Effect simulation results

Simulation #	Compositon	Average PSD
8	C 0.23% and S+P 0.044%	1.530%
10	C 0.3% and S+P 0.08%	1.521%
11	C 0.15% and S+P 0.08%	1.459%
12	C 0.3% and S+P 0.02%	1.292%

Cone Casting

Simulation Setup

In addition to "T" section castings, an additional two castings were simulated based on Research Report #103. This was work done by Charles Bates at the University of Alabama and tests the variation of hot tearing with various binders and core materials [8]. This casting is a cone casting illustrated in Figure 11. The casting develops a hot tear where the ingate meets the cone. This test casting is simulated using a WCB, 1022 alloy using IDS solidification analysis package and MAGMAsoft database to calculate the material properties similar to the previous "T" section simulation setup. The composition of the 1022 alloy is 0.23% carbon, 0.4% silicon, 1.25% manganese, 0.045% phosphorus, 0.045% sulfur, and 0.2% chromium. Two types of cores are simulated. The strong core is simulated using thermal expansion coefficients for furan sand [9]. The weak core is simulated using a zero stress boundary condition. The heat transfer is the same in both cases.

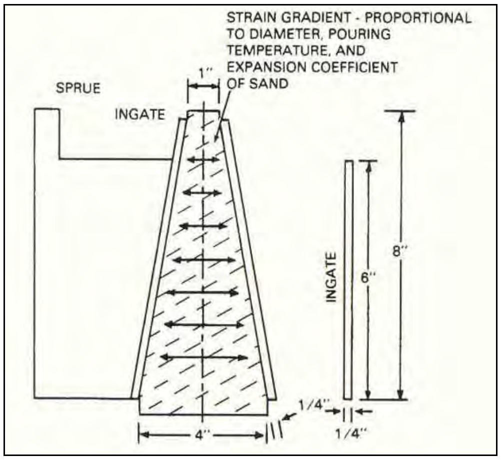

Figure 11 Cone Casting [8].

Results

The tearing of the cone casting occurs at the junction of the ingate and the cone. Figure 12 shows a result from the experimental work [8]. This graph shows that the hot tear length is dependent on the density of the core. The hot tear length reduces to zero at smaller core densities. In the simulation this density effect is included. By using experimentally calculated thermal expansion coefficients, the high-density, strong core is modeled. By using a zero stress condition boundary at the core surface, the low-density, weak core is modeled. Figure 13 shows the results of the simulation. This figure is an x-ray view showing indications of PSD that are 0.5% and greater. The scale in the figure is 0.0% - 2.0% PSD.

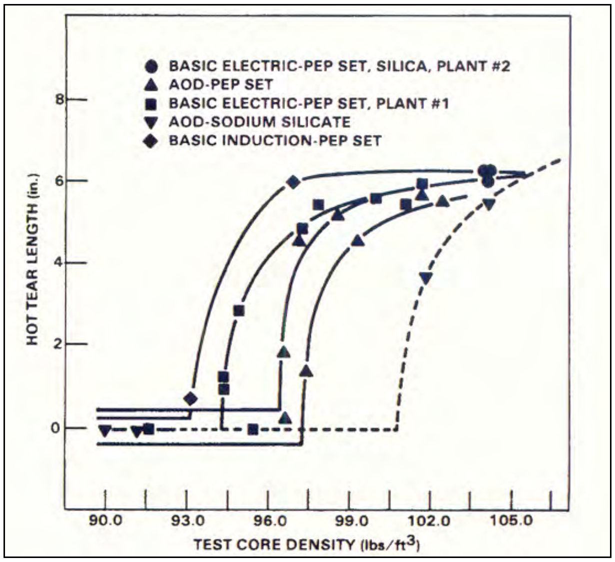

Figure 12 Cone Casting Result[8].

Figure 13 Cone Casting with (a) strong core and (b) weak core.

Conclusion

A new hot tear indicator based on a continuity approach is introduced. The porosity due to solid deformation is demonstrated to be sensitive to the known factors affecting hot tearing. The indications increase for increasing strain, unfed hot spots, increasing carbon, sulfur and phosphorus, and core restraint. If this indicator is used in defect analysis for simulated casting geometries, careful attention should be paid to regions containing significant PSD. This porosity due to solid deformation is a physically sensible explanation for hot tears and may lead to a development of a reasonable prediction of hot tearing of castings.

Acknowledgments

We wish to thank the Steel Founders' Society of America for their assistance in this work.

Bibliography

1. C.W. Briggs: *Hot Tears in Steel Castings,* Steel Founders' Society of America, Crystal Lake, IL, 1968

2. A. Chojecki, I. Telejko, and T. Bogacz, Influence of chemical composition on the hot tearing formation of cast steel, *Theoretical and Applied Fracture Mechanics*, volume 27, 1997, pg 99-105.
3. M. Rappaz, J.-M. Drezet, and M. Gremaud, A New Hot-Tearing Criterion, *Metallurgical and Materials Transactions A*, volume 30A, February 1999, pg 449-455.
4. C. L. Martin, M. Braccini, and M. Suery, Rheological behavior of the mushy zone at small strains, *Materials Science and Engineering A*, volume A325, 2002, pg 292-301.
5. C.W. Briggs, Elements of Design for Prevention of Hot Tearing in Steel Castings, *Steel Founders' Society of America Research Report*, No. 38, Technical Research Committee, SFSA, February 1957.
6. A. Mo, M. M'Hamdi, and H. G. Fjaer: "Mushy Zone Rheology and Hot Tearing in Aluminum DC Casting", pp. 199-206, *Modeling of Casting, Welding and Advanced Solidification Processes X,* edited by D. M. Stefanescu, J.A. Warren, M.R. Jolly, and M J.M. Krane, Warrendale, PA, 2003.
7. K. Carlson, Z. Lin, R. Hardin, C. Beckermann, G. Mazurkevich, M. Schneider: "Modeling of Porosity Formation and Feeding Flow in Steel Casting", pg 295-302, *Modeling of Casting, Welding and Advanced Solidification Processes X,* edited by D. M. Stefanescu, J.A. Warren, M.R. Jolly, and M J.M. Krane, Warrendale, PA, 2003.
8. C. E. Bates, Effects of Melt Practice, Core Binder, and Core Density on Hot Tearing of Cast Steel, *Steel Founders' Society of America Research Report* , No. 103, Techincal Research Committee, SFSA, January 1991.
9. S. Ou and C. Beckermann, "Simulation of Dimensional Changes in Steel Casting", in *Proceedings of the Steel Founders' Society of America Technical and Operating Conference*, Chicago, IL, November 2003.
10. M. Rappaz, J.-M. Drezet, P.-D. Grasso, and A. Jacot: "Hot Tearing and Coalescence: Two Deeply-Connected Phenomena", pg 53-60, *Modeling of Casting, Welding and Advanced Solidification Processes X,* edited by D. M. Stefanescu, J.A. Warren, M.R. Jolly, and M J.M. Krane, Warrendale, PA, 2003.

ELSEVIER

Materials Science and Engineering A 413-414 (2005) 30–36

MATERIALS SCIENCE & ENGINEERING A
www.elsevier.com/locate/msea

Development of a hot tear indicator for steel castings

Charles Monroe, Christoph Beckermann [*]

Department of Mechanical and Industrial Engineering, University of Iowa, Iowa City, IA 5224, USA

Received in revised form 14 July 2005

Abstract

A hot tear indicator based on the physics of solidification and deformation is presented. This indicator is derived using available data from computer simulation of solidification and solid deformation. Hot tears form when the mushy zone is starved of liquid feeding and deformed in tension. The unfed tensile deformation causes a small additional porosity. A physical model based on a mass balance is developed to find the additional porosity formed. This additional porosity or porosity due to solid deformation (PSD) is a locator for initiation sites for hot tears in the casting, not a full tear predictor. Simulation results for various "T"-shaped steel castings show good agreement with previous experimental findings. Reducing the strain in the casting and increasing the feeding of the section are found to decrease the hot tear tendency.

Keywords: Hot tears; Casting simulation; Steel

1. Introduction

Once hot tears occur in steel castings, they must be repaired by welding or the casting must be scrapped. Considerable effort is spent to eliminate hot tears from castings. Hot tears are identified as cracks, either on the surface or internally in the casting. These cracks may be large and visible to the naked eye or small and found only by magnetic particle inspection. They are caused by a combination of thermal effects, such as hot spot size and casting restraint, such as cores in cylindrical castings [1]. In addition, composition can affect hot tearing tendency [2]. Physically, two factors contribute to hot tearing in the mushy zone. Hot tears are formed when the mushy zone is cut off from liquid feeding and is under tensile loading [3].

Liquid feeding flows are induced by the contraction of liquid steel during cooling and shrinkage upon solidification. The friction that the liquid experiences, as it flows through the mush creates a significant pressure drop, such that the pressure deep inside the mushy zone is close to vacuum. Such a vacuum can also form inside a hot spot region, even if the solid fraction is still small. If the pressure is sufficiently small, porosity can form. In steel, the amount of dissolved gases is typically very small. Therefore, any porosity formation will signal that the feeding flow is cut off.

Mechanical loading, tensile or compressive, is caused by restrained thermal contraction. Restraint is the consequence of cores, geometry constraints and other factors, which act to resist the movement of the casting surface during solidification. To accommodate the restraint of a surface, mechanical strains are generated inside the casting. It is these mechanical strains and not the thermal strain that can transmit the compressive or tensile loads. In the mushy zone, the individual solid and liquid phases are incompressible but the mixture is compressible, as noted by Martin et al. [4]. In compression, liquid is squeezed out. In tension, liquid may be sucked in. If liquid is not available under tensile loading, due to the feeding flow being cut off, additional porosity may form. This porosity forms late in solidification, along grain boundaries. It is the initiation site for a hot tear and is referred to in this study as porosity due to solid deformation (PSD).

Experimental work by the Steel Founders' Society of America (SFSA) [5] demonstrated the effect of casting design on hot tearing. By changing various section lengths and thicknesses of a "T"-shaped steel casting, the effects of variation in hot spot size and strain on hot tearing was investigated. It was concluded that hot tears could be avoided by using filleted corners, smaller section size transitions and an unrestrained casting and gating layout. These methods enhance liquid feeding and reduce the tensile strain in the casting.

Numerous hot tear indicators have been reported in the literature. Critical strain has been one measure of hot tearing susceptibility [6]. However, the critical strain is dependent on

---

[*] Corresponding author. Tel.: +1 319 335 5681; fax: +1 319 335 5669.
E-mail address: becker@engineering.uiowa.edu (C. Beckermann).

0921-5093/$ – see front matter © 2005 Elsevier B.V. All rights reserved.
doi:10.1016/j.msea.2005.09.047

many other parameters, such as the availability of liquid metal feeding and strain rate and cannot be used alone as an indicator of hot tears [7]. A recently developed, physically based indicator is the RDG criterion developed by Rappaz et al. [3]. The RDG criterion is derived using a mass balance on a solidifying mushy zone. The mass balance is solved for the maximum sustainable strain rate. This is the strain rate beyond which cavitation or porosity formation occurs. The authors show that this criterion agrees with the well-known "Λ curves" for hot tearing from phenomenological models and experimental results. These "Λ curves" are graphs of certain hot tear criteria against solute concentration. A peak is observed at a composition close to the maximum freezing range of an alloy. The model is developed using a one-dimensional domain, across the mushy zone and is thus, not immediately applicable to three-dimensional situations. The RDG criterion also is sensitive to the definition of the coherency temperature, i.e., the temperature at which the dendritic network can transmit stresses. In continuous casting, this criterion is useful because the strain rate is directly related to the casting speed. However, it is not clear how the RDG criterion can be applied to shaped castings.

Mo et al. [8] recently developed a two-phase model for hot tearing, where the energy, liquid and solid momentum and continuity equations are solved simultaneously. Similar to the RDG criterion, a hot tear criterion based on the liquid pressure drop is used. However, this model also has limitations because porosity formation is not considered. The authors demonstrate the sensitivity of the liquid pressure drop to strain rate, solid to liquid velocity coupling, solid constitutive equations, etc.

In the following section, the present hot tear indicator for shaped steel castings is developed and the method used for calculating the indicator as part of a casting simulation is described. Then, the "T"-shaped castings from the SFSA experiments [5] are simulated. The simulation results are compared to the measurements. Also, the effect of feeding a hot spot on hot tearing is demonstrated.

2. Method

The present hot tear indicator is calculated from the results of relatively standard casting simulations in a two-step process. As a first step, the equations for energy, liquid momentum, continuity and gas species are solved using the commercial software package MAGMAsoft [9]. Second, the MAGMAstress module, which uses temperature results from the first simulation, is employed to model the deformation. The results from both of these simulations are then used to form the present hot tear indicator. The advantage of this methodology is that it is straightforward for industry to implement using available simulation technology. The disadvantage is that it is only an approximate solution to this coupled problem.

The solution in the first step is based on the multi-phase model for porosity formation developed by Carlson et al. [10] and implemented within MAGMAsoft. This model calculates the porosity formation and final distribution in the casting due to volume changes, but considers feeding by the liquid phase only. The solid is assumed to be rigid and stationary.

The stress analysis in the second step is based on a standard small-strain, thermo-elastic formulation that considers both the metal and the mold. This simulation yields the stresses and the thermal and elastic strains and strain rates in the solidifying casting geometry. The neglect of inelastic contributions to the total strain is believed to be a reasonable approximation in the present application, because the stresses encountered are small. In steel casting, the extent of the mushy zone is relatively short and the thermal strains of the fully solid material (e.g., the shell) control the deformations during solidification. Since the fully solidified portions of a casting are much more rigid than the liquid or the mushy zone, the weaker areas will simply conform to the thermal contractions of the adjacent solid. The mechanical properties of the mush are discussed later in this section.

The above two-step method decouples the liquid and solid phase movements inside the mushy zone. In the first step, any effect that solid deformation may have on the flow of the liquid in the mush and on the formation of porosity is neglected. In the second step, liquid flows and porosity formation are not considered when calculating the solid deformation. The coupling of all of these effects can be better understood by examining the complete statement of continuity or mass balance for the mushy zone. The mush is considered to be a mixture of three phases: solid metal (s), liquid metal (l) and porosity (p), such that the volume fractions add up to unity, i.e., $f_s + f_l + f_p = 1$. The volume averaged mixture continuity equation is then given by:

$$\frac{\partial}{\partial t}(f_s\rho_s + f_l\rho_l + f_p\rho_p) + \nabla \cdot (f_s\rho_s\boldsymbol{v}_s + f_l\rho_l\boldsymbol{v}_l + f_p\rho_p\boldsymbol{v}_p) = 0 \tag{1}$$

where t, ρ and $\boldsymbol{v}$ are time, density and velocity, respectively. Note that the densities of the three phases are all different. Hence, Eq. (1) states that changes in the volume fractions of any of the three phases inside a control volume can be balanced by mass fluxes of any of the three phases in or out of the control volume. If the phase volume fractions do not change, solid deformation ($\boldsymbol{v}_s \neq 0$) can be accommodated by flow of liquid. This full coupling of all effects cannot be accounted for with the present two-step solution procedure.

In order to make progress, the above mixture continuity equation is split into two parts: one that is solved as part of the porosity model of the first step and another one that only accounts for porosity formation due to solid deformation. This split is accomplished by defining the total pore fraction to consist of two components:

$$f_p = f_p^l + f_p^s \tag{2}$$

The first component, f_p^l, is referred to as porosity or original porosity and includes all contributions due to shrinkage and flow of liquid. The second component, f_p^s, is referred to as additional porosity or porosity due to the solid deformation and includes only contributions due to movement of solid. PSD is, thus, the porosity that is created or destroyed by solid deformation. It is this additional porosity that constitutes potential initiation sites for hot tears.

Substituting Eq. (2) into Eq. (1) and neglecting the terms associated with the pore density (i.e., $f_p \rho_p \boldsymbol{v}_p = 0$ and $f_p \rho_p = 0$), Eq. (1) is rearranged as follows:

$$\frac{\partial}{\partial t}(f_s(\rho_s - \rho_l) + \rho_l - f_p^l \rho_l) + \nabla \cdot (f_l \rho_l \boldsymbol{v}_l) = \frac{\partial}{\partial t}(f_p^s \rho_l) - \nabla \cdot (f_s \rho_s \boldsymbol{v}_s) \qquad (3)$$

A decoupling is now introduced by setting both sides of Eq. (3) equal to 0. The left side of Eq. (3), equal to 0, is the mixture continuity equation if the solid phase is assumed to be rigid and stationary; this continuity equation is solved for f_p^l as part of the multi-phase model for porosity formation in step one of the present solution procedure. Setting the left side equal to 0 requires a balance between the additional porosity f_p^s and the solid mass flux on the right side of Eq. (3). The consequence of this decoupling is that the solid deformation in the mushy zone has no effect other than to create or destroy additional porosity, i.e., solid deformation cannot squeeze out or pull in liquid. This decoupling is believed to be a good approximation for steel castings because hot tears form only when the liquid feeding flow is already cut off.

Setting the left side of Eq. (3) equal to 0 and assuming, as a first approximation that the liquid and solid metal densities are constant, yields:

$$\frac{\partial}{\partial t}(f_p^s) = \frac{\rho_s}{\rho_l} \nabla \cdot (f_s \boldsymbol{v}_s) \qquad (4)$$

Eq. (4) must be integrated to find the porosity due to solid deformation. The integration is started at the point in time when the porosity increases from 0, i.e., $f_p^l > 0$. This time indicates when the liquid feeding is cut off and the pressure is low enough to form a pore. When liquid feeding is still available, solid deformation is not expected to create any porosity. The integration is stopped at the point in time when the mush is locally solidified, i.e., $T < T_s$. Further crack growth and propagation in the fully solidified material are not modeled by this approach. Using these integration limits, Eq. (4) becomes:

$$\mathrm{PSD} = f_p^s = \frac{\rho_s}{\rho_l} \int_{f_p^l > 0}^{T < T_\mathrm{s}} \nabla \cdot (f_s \boldsymbol{v}_s) \mathrm{d}t \qquad (5)$$

Eq. (5) states that the local solid dilatation, after liquid feeding is cut off, will cause PSD formation. The local solid dilatation rate is found from the stress analysis in the second step of the present solution procedure. As noted in Section 1, the thermal contractions of the mushy zone do not contribute to the deformation of the solid, but only to liquid feeding. Therefore, only the mechanical strains and strain rates are used in the calculation of PSD. The solid velocity multiplied by the solid fraction is known as the superficial velocity. As a first approximation, the divergence of this superficial velocity is identified with the trace of the mechanical strain rate tensor, i.e.,

$$\nabla \cdot (f_s \boldsymbol{v}_s) = \mathrm{trace}(\dot{\varepsilon}^{\mathrm{m}}) = \dot{\varepsilon}_{xx}^{\mathrm{m}} + \dot{\varepsilon}_{yy}^{\mathrm{m}} + \dot{\varepsilon}_{zz}^{\mathrm{m}} \qquad (6)$$

The superscript m denotes that only the mechanical contribution of the strain is used. Substituting Eq. (6) into Eq. (5), the final expression for PSD is given by:

$$\mathrm{PSD} = f_p^s = \frac{\rho_s}{\rho_l} \int_{f_p^l > 0}^{T < T_s} [\dot{\varepsilon}_{xx}^{\mathrm{m}} + \dot{\varepsilon}_{yy}^{\mathrm{m}} + \dot{\varepsilon}_{zz}^{\mathrm{m}}] \mathrm{d}t \qquad (7)$$

Eq. (7) constitutes the present hot tear indicator. The integration of the strain rates over time in Eq. (7) shows that PSD is nothing but a volumetric strain. However, PSD is more than an indicator that is solely based on the notion of a critical strain for hot tear formation [6,7]. Because the integration is started at the point in time when the regular porosity starts to form ($f_p^l > 0$), PSD accounts for the effect of liquid feeding. This is critical for the prediction of hot tears in shaped castings. Since liquid feeding is affected by many factors, including the freezing range and the permeability of the mush [10], PSD should yield predictions that are not dissimilar to the ones from the RDG criterion developed by Rappaz et al. [3]. Note that Eq. (7) does not explicitly contain the coherency temperature, consideration of grain boundaries or other effects associated with the structure of the mush; these parameters must generally be accounted for in the mechanical model (i.e., the constitutive equation) for the mush that is used to calculate the strain rates in Eq. (7).

It must be emphasized that the PSD found through Eq. (7) provides only an indication for the initiation of hot tears in the mushy zone. It does not predict tear or crack growth and the extent of a hot tear in the solidified casting at room temperature. The appearance of a crack can change the course of stress development in the casting during cooling. For example, if a hot tear develops at a certain location in a casting, stresses may be relieved and hot tears may not appear in other areas of the casting. However, the PSD indicator given by Eq. (7) can provide the initiation sites for hot tears and the locations with the greatest relative PSD percentages can be expected to have the greatest potential for hot tears.

The standard MAGMAstress module is used in the present study to calculate the mechanical strain rates for use in Eq. (7). This module requires the specification of the thermal expansion coefficient and the mechanical properties as a function of temperature throughout the casting process. Here, only the properties for the mush are discussed. The thermal expansion coefficient is found using the mixture density, $\bar{\rho} = f_s \rho_s + (1 - f_s)\rho_l$, where the individual phase densities and the solid fraction are given as a function of temperature. The relationship between the density and the thermal expansion coefficient is:

$$\alpha = -\frac{1}{\bar{\rho}} \frac{\partial \bar{\rho}}{\partial T} \qquad (8)$$

Full consideration of the complex mechanical behavior of the mush as a function of its structure and coherency [4] is beyond the scope of the present study. As discussed in Section 1, the mush must generally be viewed as a compressible mixture. A standard viscoplastic constitutive model for an incompressible material could not be used to describe the mechanical behavior of the mush, because it would yield a zero trace of the strain rate tensor and, hence, no PSD. In the MAGMAstress module utilized here, the same elastic model is used for the mush as for the fully solid regions. The elastic modulus for the mush is assumed to obey a law of mixtures such that $E = f_s E_S$, where E_s is the elastic modulus at the temperature T_s (100% solid). In other words, the mush is assumed to behave like a sponge where the solid provides the stiffness and the liquid is allowed to flow in or out. As the solid fraction approaches 0 and in the fully liquid, a small minimum value for E is used to avoid singularities in the stress calculations. A non-zero trace of the strain rate tensor is obtained in an elastic analysis for a Poisson ratio that is different from 1/2. This property of an elastic material is used here to model the compressibility of the mush. The Poisson ratio is simply assumed to be the same as for the fully solid. Due to this very approximate treatment of the mechanical behavior of the mush, the calculated trace of the strain rate tensor in the mush is likely to be inaccurate. However, hot tearing susceptibility can still be evaluated by comparing the relative magnitude of the PSD values, as shown below.

3. Simulation setup

The present hot tear indicator is validated using the “T”-shaped steel casting experiments of Ref. [5]. The composition of the steel was 0.23% carbon, 0.5% silicon, 0.6% manganese, 0.028% sulfur and 0.016% phosphorus. Fig. 1 shows a schematic of the casting geometry. The two ends of the arm were mechanically fixed in the mold, resulting in a zero displacement condition at the ends. Due to the contractions during cooling of the casting, this creates a large amount of thermal strain in the arm. The strain is concentrated in the center of the arm (i.e., at the mid-length) by the addition of the leg. The leg creates an unfed hot spot in the center of the “T”, such that any hot tears would be expected at that location. In all cases, the thickness of the “T” was 1.0″ (2.54 cm).

Nine “T”-shaped castings were simulated with the following changes in the geometry. The arm length was either 26″ (66.04 cm) or 36″ (91.44 cm); lengthening the arm increases the amount of strain in the hot spot region. The arm width, dimension ‘C’ in Fig. 1, was increased from 0.5″ (1.27 cm) to 1.0″ (2.54 cm) and then to 2.0″ (5.08 cm); this increases the strength of the arm by providing more material to tear. The leg width, dimension ‘E’ in Fig. 1, was increased from 1.0″ (2.54 cm) to 2.0″ (5.08 cm); this increases the hot spot size at the section transition. These geometry changes constitute a total of eight test cases, as summarized in Table 1. An additional test case was created by placing a riser on top of the leg section of test casting 8 (see Table 1); this ninth case illustrates the effect of feeding on hot tearing.

Fig. 2 shows the casting simulation geometry for the three cases with a 36″ (91.44 cm) arm length (cases 7–9). The castings were gated at the end of the leg section using a runner that was 0.5″ (1.27 cm) thick and 1″ (2.54 cm) wide. At the end of the runner, a small riser, 2″ (5.08 cm) in diameter, was used to affect the filling of the mold and create a connection to the atmosphere

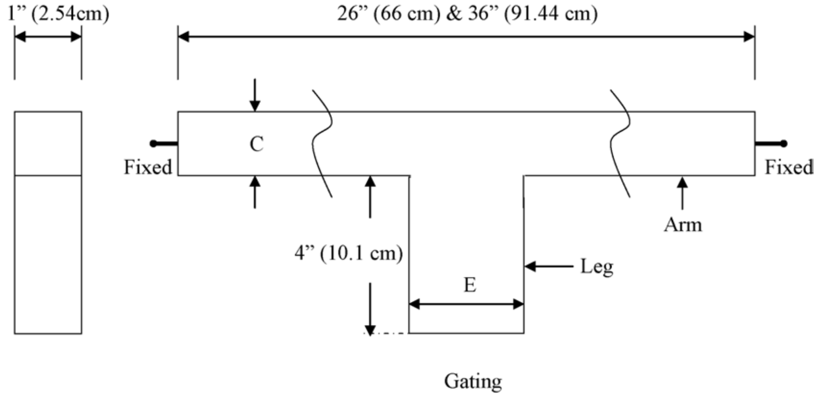

Fig. 1. Schematic of “T”-shaped casting [5].

Table 1
Summary of hot tearing predictions and experimental results for the “T”-shaped steel castings of Ref. [5]

No.	Arm length	Arm width, ‘C’	Leg width, ‘E’	PSD average (%)	Casting result [5]
1	26″ (66)	0.5″ (1.27)	1.0″ (2.54)	**2.247**	**Heavy tear**
2	26″ (66)	0.5″ (1.27)	2.0″ (5.08)	**1.724**	**Tears**
3	26″ (66)	1.0″ (2.54)	1.0″ (2.54)	0.742	Untorn
4	26″ (66)	1.0″ (2.54)	2.0″ (5.08)	1.334	Untorn
5	26″ (66)	2.0″ (5.08)	1.0″ (2.54)	0.762	Untorn
6	26″ (66)	2.0″ (5.08)	2.0″ (5.08)	1.087	Untorn
7	36″ (91.4)	1.0″ (2.54)	1.0″ (2.54)	0.923	Untorn
8	36″ (91.4)	1.0″ (2.54)	2.0″ (2.54)	**1.530**	**Heavy tear**
9	36″ (91.4)	1.0″ (2.54)	2.0″ (2.54) w/riser	0.780	
Using coherency temperature integration limit					
8b	36″ (91.4)	1.0″ (2.54)	2.0″ (2.54)	1.589	
9b	36″ (91.4)	1.0″ (2.54)	2.0″ (2.54) w/riser	1.564	

Values in parentheses are in cm.

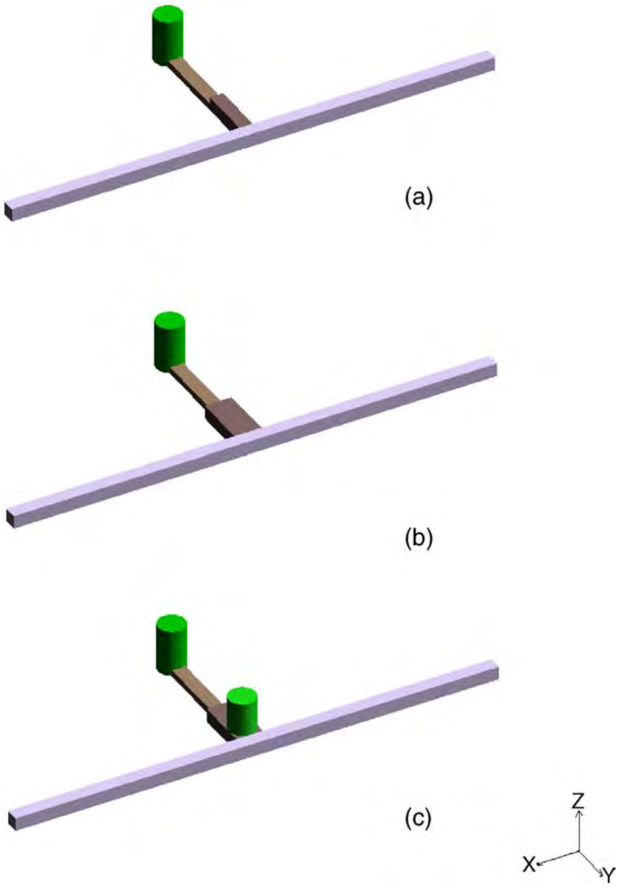

Fig. 2. Casting and gating geometry for a 36″ (91.44 cm) arm length and leg widths of: (a) 1.0″ (2.54 cm); (b) 2.0″ (5.08 cm); (c) 2.0″ (5.08) with riser.

surrounding the sand mold. The runner freezes off within a short time after filling, such that the riser at the end of the runner plays no role in the feeding of the "T" section. The riser on top of the leg in case 9 (Fig. 2c) is, however, intended to feed the hot spot at the center of the "T" section.

4. Results and discussion

An example of a predicted porosity distribution from the first step of the present simulation methodology is shown in Fig. 3a. This porosity, denoted as f_p^l in Section 2, is solely due to solidification shrinkage and the lack of feeding. As expected, a large amount of porosity, up to about 30%, can be observed in the leg section at the location of the hot spot. In addition, strong centerline porosity is present throughout the arm. Recall that the local time when this porosity starts to form during solidification constitutes the lower integration limit for calculation of the present hot tear indicator, PSD, as given by Eq. (7). An example of the predicted deformation from the second step of the present method is shown in Fig. 3b. This result corresponds to the point in time when the casting is just solidified. The deformation is magnified by 20 times to highlight the deflections. The predicted distortion pattern shows that the area of the bar near the hot spot is in tension due to the convex bending. In the following, the calculated PSD results are presented for each of the cases in Table 1 and compared to the corresponding casting experiments from Ref. [5].

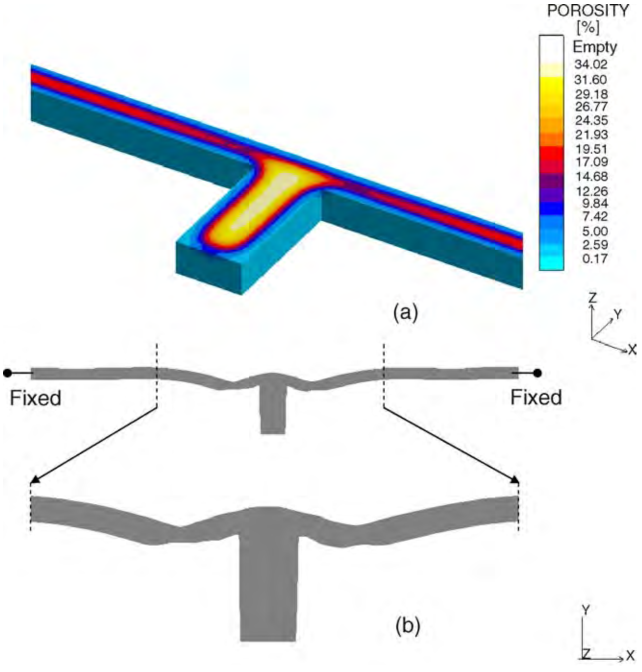

Fig. 3. Predicted MAGMAsoft results for a 36″ (91.44 cm) bar length and leg width of 2.0″ (5.08 cm) at fully solid: (a) distribution of porosity, f_p^l, neglecting solid deformation and (b) deformation magnified by a factor of 20.

4.1. Effect of geometry changes

Example casting trial results are provided in Fig. 4 for cases 7 and 8. The photograph shows that a heavy hot tear developed in the hot spot of the casting with the larger leg width (case 8, top), while the casting with the smaller leg width (case 7, bottom) is untorn. The formation of the hot tear can be explained by the fact that the large leg in case 8 keeps the center section partially liquid for a longer time than in case 7. During this time, the arm experiences a large strain at the location of the hot spot, which leads to the hot tear.

The corresponding simulation results for cases 7 and 8 are shown in Fig. 5. This figure is an X-ray view showing only indications of PSD that are 0.5% and greater, cut at mid-plane. The scale in figure is 0–6% PSD. It can be seen that for case

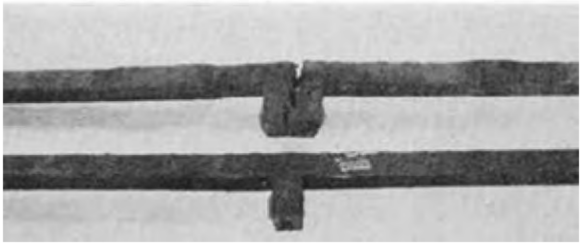

Fig. 4. Example casting trial results for a 36″ (91.44 cm) arm length and 1.0″ (2.54 cm) arm width; the casting at the top with a leg width of 2.0″ (5.08 cm) shows a heavy tear, while the casting at the bottom with a leg width of 1.0″ (2.54 cm) is untorn [5].

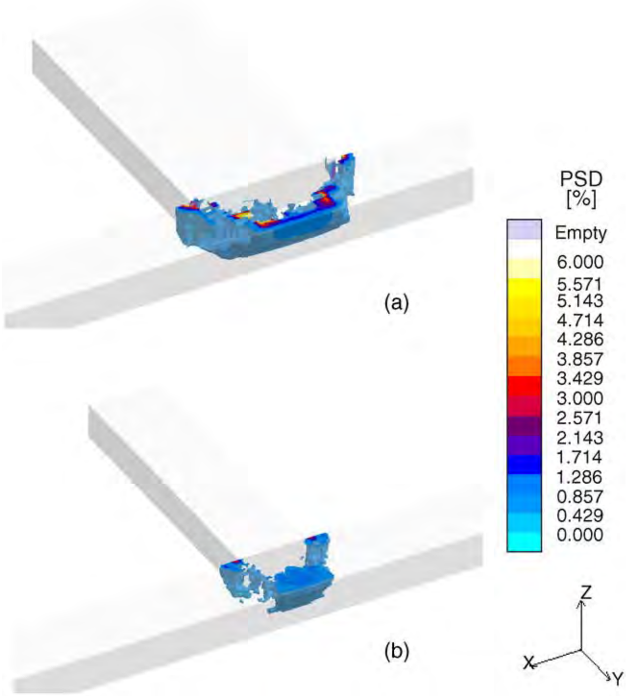

Fig. 5. Predicted PSD distribution for a 36″ (91.44 cm) arm length and 1.0″ (2.54 cm) arm width, with 2.0″ (5.08 cm) (a) and 1.0″ (2.54 cm) (b) wide legs; the two X-ray views are cuts at the mid-plane and only show PSD percentages greater than 0.5%.

8 (Fig. 5a), a large region of PSD is predicted at the location of the hot tear in the corresponding casting experiment (Fig. 4). Fig. 5b shows that a region of PSD is also predicted for case 7, but the PSD values are much smaller than in case 8. This indicates that lower PSD values do not lead to hot tears. Note that the PSD indications will not look like the final hot tear from the experiment. This is because PSD is only an initiation site locator for hot tears and not a crack prediction.

In order to characterize and rank the PSD predictions for each simulation, an average PSD value is calculated by integrating all PSD values above 0.5% over the entire casting. Thus, only the PSD values visible in the X-ray views of Fig. 5 (and similar figures for the other cases) are used in forming the average. Table 1 provides the average PSD values for all cases. It can be seen that PSD averages above approximately 1.5% correspond to castings with hot tears, while for PSD averages below that value, no hot tears were observed in the casting experiments. It is emphasized that the actual magnitude of the PSD average has no physical significance; only their relative values are of importance here. As shown in Table 1, there are three castings that showed hot tears. Two of the castings (cases 1 and 2) have the smallest arm width of 0.5″ (1.27 cm). The small arm width causes the accumulated strain to be larger than in the other cases. Ultimately, the arms with the smaller cross section will yield more easily and form a crack. The third casting that tore in the experiments was case 8 with the longest arm length (and intermediate arm width) and largest leg width. As mentioned before, the long arm length causes a large strain, while the large leg width increases the hot spot size and thus, the time over which the critical area is vulnerable to hot tearing. All of these effects appear to be captured by the present hot tear indicator.

4.2. *Effect of feeding*

Cases 8 and 9 illustrate the effect of feeding on the PSD predictions. In case 9, a riser is added on top of the 2.0″ wide leg of case 8 (see Fig. 2). The resulting PSD predictions are compared in Fig. 6a (case 8) and Fig. 6c (case 9). As expected,

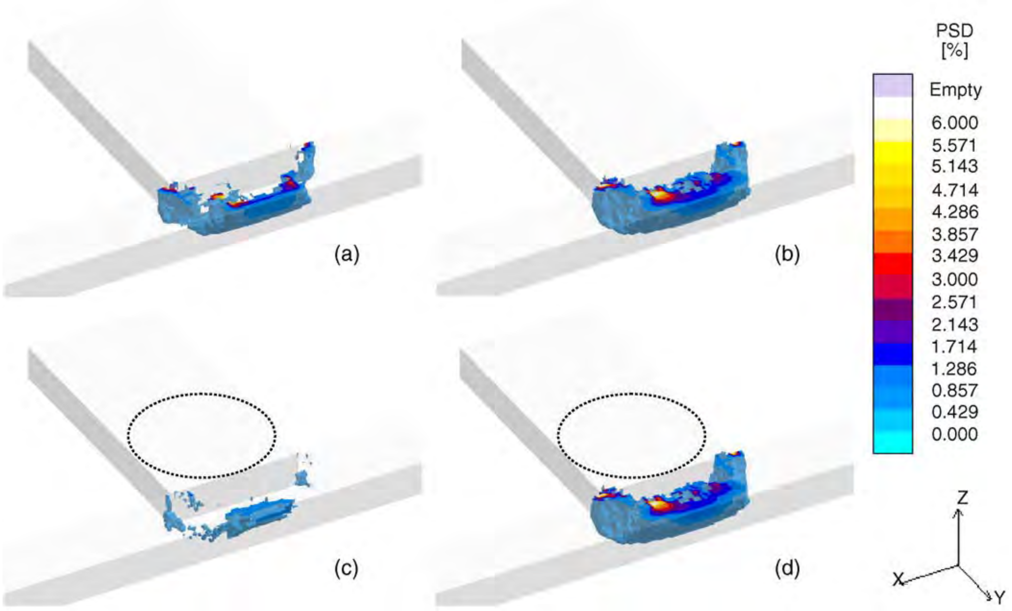

Fig. 6. Comparison of predicted PSD distributions for: (a) case 8; (b) case 8b; (c) case 9; (d) case 9b; cases 8b and 9b (right panels) use a coherency temperature integration limit that does not consider liquid feeding; cases 9 and 9b (lower panels) use a riser on top of the leg section as indicated by the circle; all four X-ray views are cuts at the mid-plane and only show PSD percentages greater than 0.5%.

the feeding of the hot spot area by the riser significantly reduces the PSD predictions relative to the case without a riser. The present hot tear indicator can predict this effect because the strain rates are only integrated, when the feeding flow is cut off (i.e., $f_p^l > 0$). Table 1 shows that the average PSD value due to the addition of the riser decreases from 1.53 to 0.78%.

To further demonstrate the importance of including the feeding effect in the present hot tear prediction, another two simulations (cases 8b and 9b) were performed, where the lower integration limit in Eq. (7) (i.e., $f_p^l > 0$) was replaced by a limit that is based on a critical mush coherency temperature. The new lower integration limit is the time at which the local temperature reaches the coherency temperature, i.e., $T < T_{\text{coherent}}$, regardless of the availability of liquid feeding. The coherency temperature is defined here as the temperature where the solid fraction is equal to 0.82; it can be expected that approximately at this solid fraction the dendritic network begins to transmit stresses [3]. By changing the integration limit as described above, the strain rate may be integrated when feeding is still available and the hot tear may be healed; furthermore, integration will not start until the coherency temperature is reached even if feeding is already cut off. Fig. 6 shows that the change in the lower integration limit has little effect on the PSD predictions in the absence of the riser (compare Fig. 6a and b). This simply indicates that in the absence of the riser the time at which the coherency temperature is reached is approximately the same as the time when porosity starts to form. On the other hand, in the presence of the riser (case 9), the change in the lower integration limit has a large effect on the PSD predictions (compare Fig. 6c and d). When using the lower integration limit based on the coherency temperature, the PSD predictions are relatively unchanged by the addition of the riser (compare Fig. 6b and d). The average PSD values in Table 1 further support the above observations. The average PSD for cases 8b and 9b with the coherency temperature integration limit are of the same magnitude, indicating that the presence of feeding is not taken into account when using this integration limit. Thus, incorporating liquid metal feeding into the hot tear indicator, through the use of the $f_p^l > 0$ integration limit, is of great importance. Certainly, a more detailed consideration of the mechanical behavior of the mush and the mush coherency is nonetheless warranted for future studies.

5. Conclusions

A new hot tear indicator, PSD, based on a continuity approach is introduced. The PSD indicator is the integration of the volumetric mechanical strain rate after liquid metal feeding is cut off. The PSD indications are initiation sites for hot tears. PSD is demonstrated to be sensitive to some known factors affecting hot tearing. The indications increase for increasing strain and unfed hot spots.

This indicator can be used in defect analysis for simulated casting geometries and careful attention should be paid to regions containing significant PSD. This porosity due to solid deformation is a physically sensible explanation for hot tears and may lead to a development of a reasonable prediction of hot tearing of steel castings.

Acknowledgements

We wish to thank the Steel Founders' Society of America for their assistance in this work. This work was prepared with the support of the U.S. Department of Energy (DOE), Award No. DE-FC36-04GO14230. However, any opinions, findings, conclusions or recommendations expressed herein are those of the authors and do not necessarily reflect the views of the DOE.

References

[1] C.W. Briggs, Hot Tears in Steel Castings, Steel Founders' Society of America, Crystal Lake, IL, USA, 1968.
[2] A. Chojecki, I. Telejko, T. Bogacz, Theor. Appl. Fract. Mech. 27 (1997) 99–105.
[3] M. Rappaz, J.-M. Drezet, M. Gremaud, Metall. Mater. Trans. A 30A (1999) 449–455.
[4] C.L. Martin, M. Braccini, M. Suery, Mater. Sci. Eng. A325 (2002) 292–301.
[5] C.W. Briggs, Steel Founders' Society of America Research Report, No. 38, Technical Research Committee, Crystal Lake, IL, USA, February 1957.
[6] H. Hiebler, C. Bernhard, Steel Res. 70 (1999) 349–355.
[7] K. Nakayama, M. Kinefuchi, K. Tsutsumi, in: B.G. Thomas, C. Beckermann (Eds.), Modeling of Casting, Welding and Advanced Solidification Processes, vol. VIII, Warrendale, PA, 1998.
[8] A. Mo, M. M'Hamdi, H.G. Fjaer, in: D.M. Stefanescu, J.A. Warren, M.R. Jolly, M.J.M. Krane (Eds.), Modeling of Casting, Welding and Advanced Solidification Processes, vol. X, Warrendale, PA, 2003, pp. 199–206.
[9] MAGMAsoft, MAGMA GmbH, Kackerstrasse 11, 52072 Aachen, Germany.
[10] K. Carlson, Z. Lin, R. Hardin, C. Beckermann, G. Mazurkevich, M. Schneider, in: D.M. Stefanescu, J.A. Warren, M.R. Jolly, M.J.M. Krane (Eds.), Modeling of Casting, Welding and Advanced Solidification Processes, vol. X, Warrendale, PA, 2003, pp. 295–302.

Monroe, C., and Beckermann, C., “Simulation of Hot Tearing and Distortion During Casting of Steel: Comparison with Experiments,” in Proceedings of the 60th SFSA Technical and Operating Conference, Paper No. 5.7, Steel Founders' Society of America, Chicago, IL, 2006.

Simulation of Hot Tearing and Distortion during Casting of Steel: Comparison with Experiments

C. Monroe
C. Beckermann
Department of Mechanical and Industrial Engineering
The University of Iowa, Iowa City, IA 52242

Abstract

Hot tears are defects that occur during solidification of a casting that is subjected to mechanical restraints. Several key factors are known to aggravate the hot tearing of cast steel. These factors include: increasing the duration of a hot spot without increasing the feeding, increasing the strain, and increasing the solidification range through alloying elements. The effects of these factors have been evaluated during solidification through the use of a T-section test casting. The T-section test castings provide measurements of distortion and stresses during solidification and during further cooling of the casting. The results confirm previous findings and provide new data for analysis and comparison for accurate hot tear prediction.

Introduction

Hot tearing in any steel casting is disastrous. Extensive rework is required with the appearance of any small linear indication on the casting. Either design or process changes will be proposed to eliminate this defect. However, even the normal process fluctuations can cause random appearances of this defect during production. It is possible that previous successful changes may not help eliminate future hot tear problems. Improved hot tear prediction and a more fundamental understanding of hot tearing is important when trying to eliminate this defect from any part or process.

Fundamentally, two local phenomena are working in the mushy zone to create hot tears. These two phenomena are a lack of liquid feeding and tensile solid deformation. First, liquid feeding is the flow of liquid metal into or away from the mushy zone to account for volumetric changes in the mushy zone. The mushy zone is analogous to a sponge shown in the insert in Figure 1. Initially liquid may flow through the sponge but as the liquid flows it also solidifies. Eventually the flow may be cut off because the liquid pockets become isolated. As long as the liquid pressure is sufficient to drive liquid into the pockets, no porosity will form. But when the pockets become isolated then the liquid will not feed the contraction during solidification and porosity will form. Second, tensile solid deformation is also necessary for the creation of hot tears. In the sponge analogy, this tensile deformation is like stretching the sponge. Alternatively, compressive deformation is like squeezing the sponge and may eliminate porosity and hot tears. Tensile deformation is caused by the restrained thermal contraction of the entire casting. Restrained thermal contraction may occur, for example, by a core surface or by another feature of the same casting. When the mushy zone is being deformed in tension, solid dendrites or grains are being pulled apart. As the solid pieces are pulled apart, additional liquid metal must flow into the mushy zone to fill this space. If the liquid metal cannot feed this deformation, then again porosity will form. Under ample deformation this initial porosity will propagate to form a hot tear.

The addition of Sulfur and Phosphorus will not change the fundamentals mentioned above. Instead, Sulfur and Phosphorus will segregate to the grain boundaries and depress the solidus temperature. This last liquid to solidify is on grain boundaries, which under tensile deformation will easily separate. The depressed solidus temperature increases the time that tensile strain may accumulate when flow is cut off.

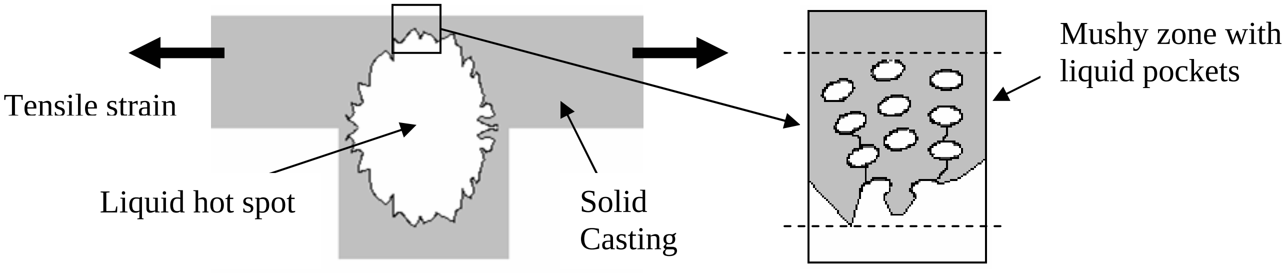

Figure 1. Schematic of a deforming mushy zone.

Many hot tear experiments have been performed to characterize this defect. One of the most complete summaries of steel hot tear test castings is in the Steel Founder's Society of America Research Report #38 by Charles Briggs [1]. In the report, a variety of geometries are investigated for hot tear tendency. Some of the different geometries considered include cylindrical designs (valve and pipe type castings), and straight designs with a transition (I-beams and T-sections). This report is the primary guide for elimination of hot tears through design of steel castings. Recommendations from this report include watching section size transitions and adding taper or radii to transitions.

From this report, the T-section test casting was determined as an excellent case study for evaluating hot tear models. In Figure 2, the original setup and results in the report for this test casting are summarized. These 36" length castings are restrained by cast in bolts which are attached to the flask. Depending on the ratio of the hot spot size to the width of the long section, the casting may or may not tear. The widths of the arm, dimension 'C', and leg, dimension 'E' are varied in each casting. Increasing the dimension of the arm, dimension 'C', will increase the compliance of the section, decrease hot tear tendency, and decrease the stress on the section. Increasing the dimension of the leg, dimension 'E', will increase the hot tear tendency by increasing the vulnerable time that the section may be strained to hot tear. In these results, the top casting in the picture with a 2" hot spot (dim E) and a 1" long section width (dim C) tore. The other geometries did not tear. From this experiment, it was concluded that to avoid hot tears restrained thin sections should not be joined to larger sections.

Two primary reasons make the T-section casting well suited for repeating and comparing to hot tear models. First, the properties of the mold play little role in the start or propagation of the tear. This is an advantage because mold properties are confounding parameters in many test castings that hot tear. In fact for cylindrical castings, the mold properties are the most significant factors that influence hot tearing behavior [2]. Second, the simplicity of this casting keeps the stressed direction almost completely in one dimension. For these reasons, this test casting provides an excellent comparison of model results to the actual distortions and stresses achieved. The previous results presented are limited to the picture shown above and a short table listing which castings tore. New experiments with additional measurements of the distortion and forces were repeated in order to attempt to gather data to compare to simulation.

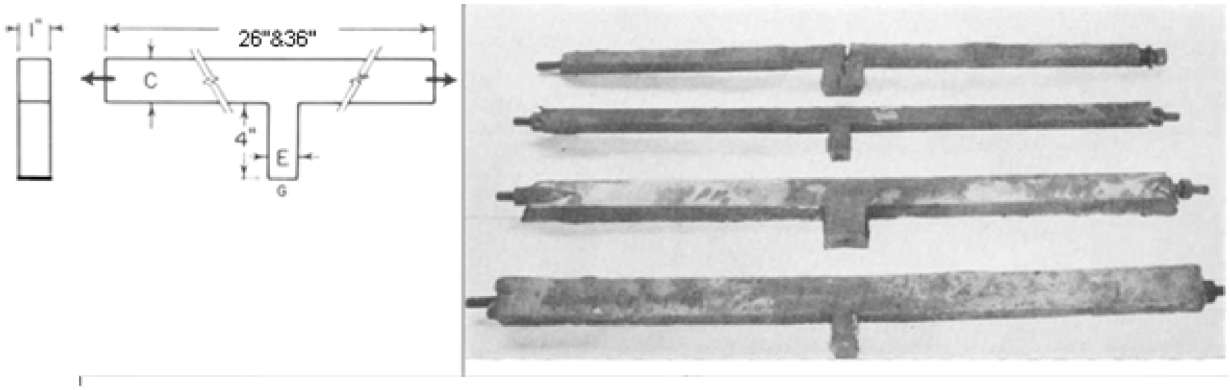

Figure 2. T-Section Hot Tear Test Casting setup and results.

New Experimental Setup

The T-section is a test casting with many desirable features for understanding the basics of hot tears. Figure 3 provides a schematic of the features in the new experimental setup. Table 1 lists the parameters of the different castings poured. Added to the old design, two small location tabs were included. These tabs were located where the greatest casting distortion was expected so that the probes would measure it. All of the new probes added to the experimental setup are designated on Figure 3. The longest length of this casting was 36” and the thickness was 1”, these dimensions were constant for every casting. Surrounding this mold was a flask used for mounting instrumentation and restraining the cast-in bolts. Therefore, this flask did not come in contact with the mold surface. The bolts extended from the flask to the mold cavity where they were cast-in upon pouring. These bolts resisted the thermal contraction of the casting and therefore provided the restraint which was needed for hot tearing.

Table 1. Castings Poured using the New Experimental Setup

Casting #	Arm	Leg	Composition	Restraint	Tear
1	2”	1”	Low Sulfur	Bolts	None
2	2”	2”	Low Sulfur	Bolts	None
3	1”	1”	Low Sulfur	Bolts	None
4	1”	2”	Low Sulfur	Bolts	None
5	1”	2”	High Sulfur	Bolts	Large Tear
6	2”	2”	High Sulfur	Bolts	Linear Indication
7	1”	2”	High Sulfur	None	None

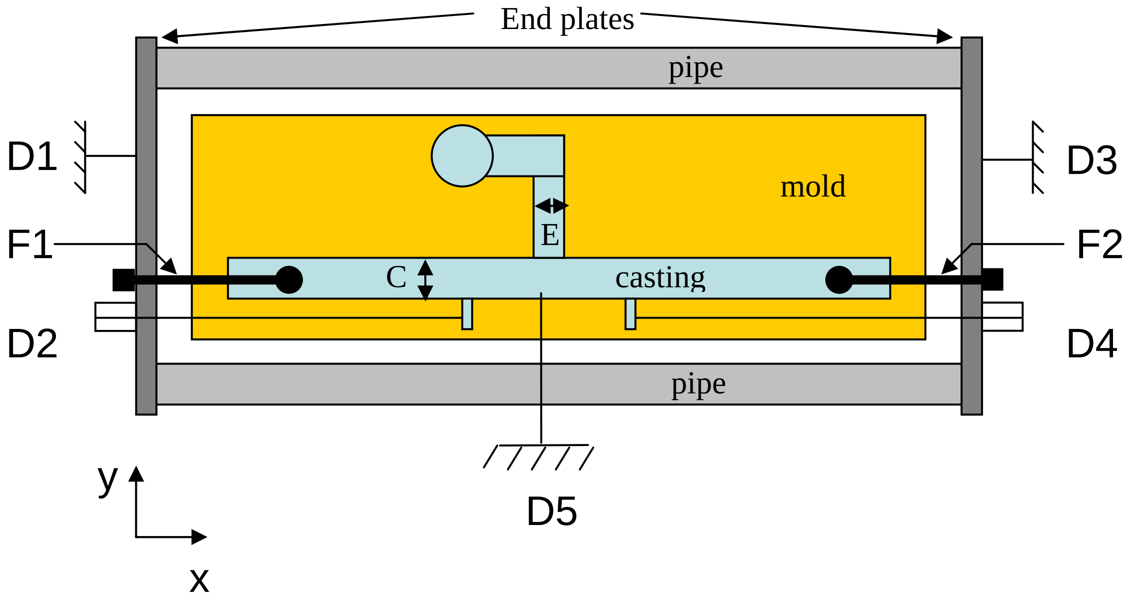

Figure 3. Schematic of the T-section setup with measurement probe locations.

The molds were made of furan sand, horizontally parted. The mold size was 60” long, 18” wide, and 12” deep (6” cope and 6” drag). During assembly, the cope and drag were “sanded” across each other to ensure that the flash due to mismatch was eliminated. Figure 4 is included to show the drag and the placeholders for instrumentation which will be discussed later. The castings were poured without a typical flask, but with the surrounding box used to mount the instrumentation and the restraining bolts. This surrounding box or flask is shown assembled around a mold in Figure 5. The cast-in bolts extended to the plates on either side and were tightened onto four 1” diameter steel pipes. The end plates were stiffened using two pieces of angle iron at the top and bottom where the pipes join the plates. Note that there was a large ~12” gap on both sides between the end plates and the mold. This space provided room to install the force gauges. This end plate and pipe assembly will be referred to as the flask.

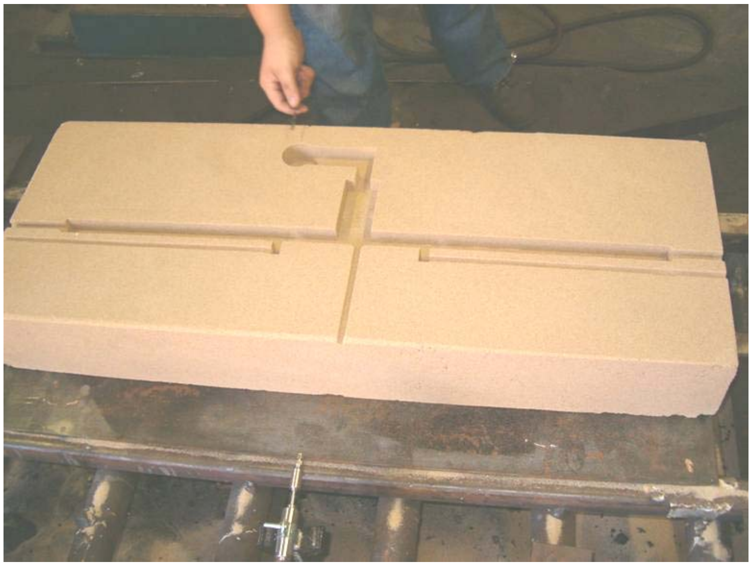

Figure 4. Drag side for the T-section casting mold.

Figure 5. Flask assembled around the T-section casting mold.

The casting was poured from a 200 lb heat, prepared in an induction furnace. The intended major alloy change between the first four castings and the final three castings was in the sulfur and phosphorus content. An increase in the Sulfur and Phosphorus content increases the likelihood of a hot tear. The alloy targeted was a low alloy, WCB, the final compositions for each casting is listed in Table 2.

Table 2. Alloy Composition

Casting #	C	Si	Mn	S	P
Briggs	0.23	0.5	0.6	0.028	0.016
1 and 3	0.22	0.46	0.39	0.012	0.015
2 and 4	0.29	0.54	0.47	0.009	0.007
5	0.20	0.6	0.64	0.028	>0.084
6 and 7	0.24	0.66	0.54	0.047	0.037

Force Measurement

In order to capture the transient deformation, force, and temperature for this casting, several measurement devices were used. The casting was restrained by bolts which extended from the casting to the flask. To ensure the mechanical contact from the bolt to the casting a nut was threaded on the bolt which was placed in the mold cavity. Load cells were used to measure the force and must be placed in line with the bolts. The load cells used were made from a 0.5" bolt with strain gauges attached to a flat surface, which was ground onto the bolts. This is shown in Figure 6. Similar load cells are rated to ~9000 lbs. In Figure 3, the load cell locations are shown in the schematic form and labeled F1 and F2.

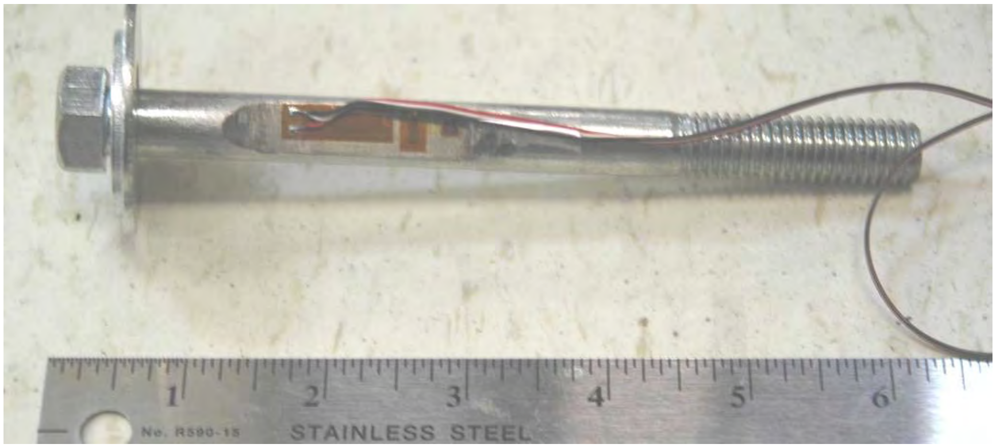

Figure 6. Load Cell bolt.

Distortion Measurement

In order to measure the deformation, linear voltage displacement transducers (LVDT) were used. The temperatures nearby the casting were too high to place the LVDT arrangement in the mold; therefore quartz rod and tube assemblies were used to transmit the deformation outside the mold. This was originally proposed by researchers measuring the expansion of graphite in cast iron, because quartz has low thermal expansion [3]. The assembly is illustrated in Figure 7, where a quartz rod of 0.08" (2mm) diameter is inserted through a quartz tube which is secure at the parting line. The rod is free to translate back and forth within the tube thus translating the movement to the LVDT. One end of the 0.08" (2mm) rod was placed inside the mold cavity where the liquid metal would solidify around it. In order to ensure optimum mechanical contact, this end was bulged. Without this bulge, the contracting solid metal would release the quartz rod due to the differences in expansion between the steel and quartz. Outside the mold the 0.08" (2mm) rod is attached to the LVDT by means of a Swagelock fitting using a Teflon ferule. This LVDT was attached to the flask outside of the mold. A total of three transient LVDT measurements were recorded per casting. In Figure 3, the LVDT locations are shown in the schematic form and labeled D2, D4, and D5.

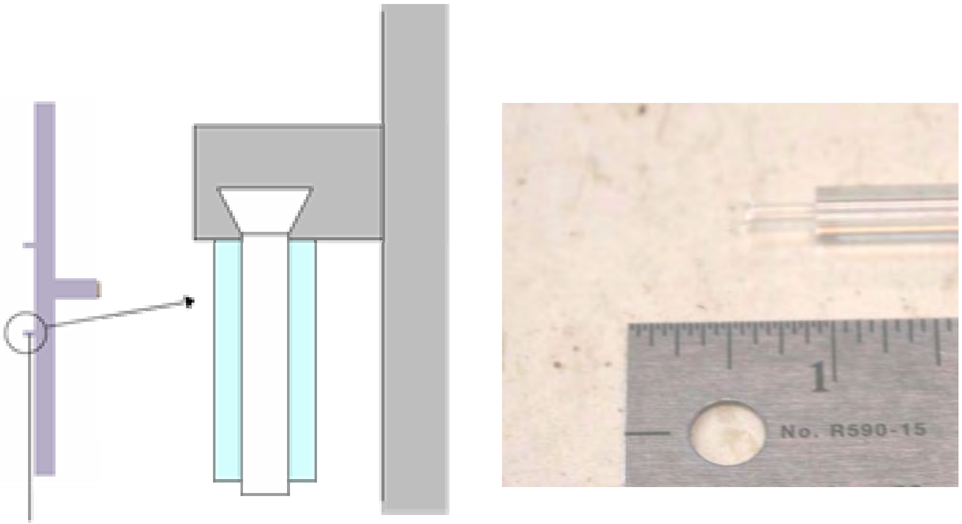

Figure 7. Quartz rod and tube assembly illustrating the bulged end.

The flask was not fixed to the mold or the ground; therefore its movement was also measured to correct the LVDT probes which were attached to the flask. To accomplish this proximity probes were mounted on either side of the flask near the bolt. In Figure 3, the proximity probe locations are shown in the schematic form and labeled D1 and D3.

All of the transient probe measurements were recorded in volts using a DAQbook USB data logger. The sampling rate was every ~1.5 seconds. The voltage signals were then converted to displacements or forces using calibration curves obtained before the experiment.

Results

First, the hot tears found in all castings will be discussed. Then, a detailed review of one casting will be made to show an example of the individual curves and results typical for all castings. In addition, a summary of all the castings will be shown. Finally, comparisons between the experimental results and the simulation results will be shown.

Summary of Hot Tearing for all test castings

Table 1 shows the changes in the parameters for the various test castings. As discussed in the introduction, the increase in the leg width increases the hot spot size and thereby increasing the hot tearing tendency. Larger arm widths increase the compliance of the casting and decrease the stress in the casting, thereby decreasing the hot tearing tendency. The addition of Sulfur and Phosphorus depress the solidus temperature and therefore increase the time that the section may hot tear. From the table it is shown that only two of the seven castings poured had linear indications. Casting 5, which was anticipated to hot tear, had a large crack. The other casting with an indication, Casting 6, was not reported to crack although conditions were sufficient for hot tear.

This binary (on-off) effect of hot tearing between castings can be seen to turn on or off just by the addition of Sulfur and Phosphorus or by increasing the hot spot size. In the previous results from Briggs, it is reported that the increase of hot spot size alone will cause the transition from no tear to tear. However the new results show that the hot tear depends on the addition of Sulfur and Phosphorus. This does not mean that Sulfur and Phosphorus is necessary for hot tearing, but it does mean that this alloy addition will certainly aggravate hot tear issues. Figure 8 shows a magnified view of the crack in the inset.

Detailed review of Casting 5 - 1” arm and 2” leg

The following Figure 8 shows the final casting shape from this heat. No temperature measurement was taken on this casting. The data was collected over the course of ~1.75 hours. This casting solidified in approximately ~2 minutes. The measurements were in the desirable range for the probes. The heat was poured at 2966 degrees Fahrenheit. A large hot tear was found. This tear initiated on a flat surface opposite the gating and not in the interior corners as one might expect. The tear propagated into the hot spot ~2” and opened to a width of ~0.25”. The movement of the probes D2 and D4 are shown in Figure 9.

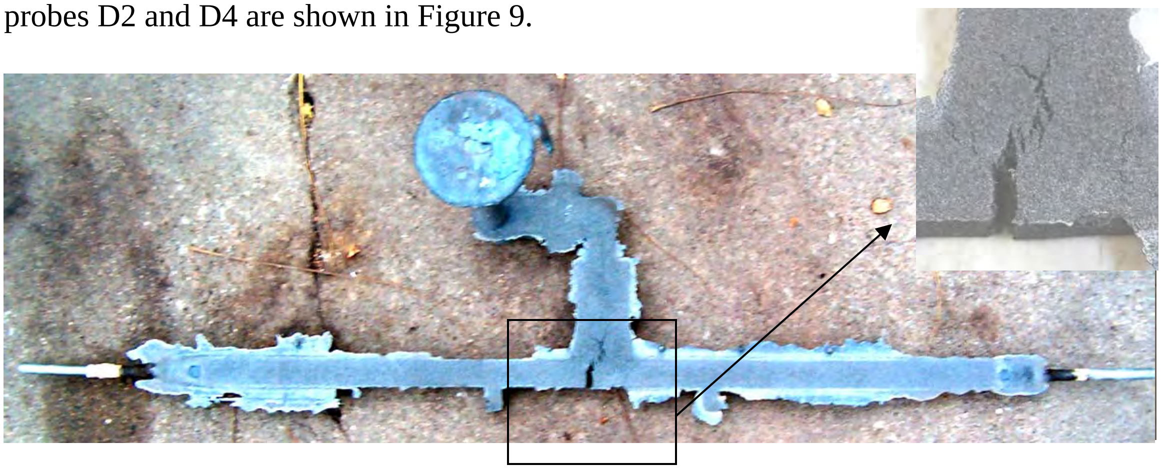

Figure 8. Final shape for Casting 5 with magnified view of crack in inset.

In Figure 9, the displacement curves separate early into solidification. This movement is almost symmetric, indicating that the flask did not shift much relative to the mold. The measurements D2 and D4 separate, indicating that the forces are building and that the gap is widening. The crack initiated early in solidification, therefore no crack event can be seen in this figure. The change in displacement direction about 15 minutes into cooling is due to a phase change in low alloy steel from austenite to pearlite at about 1100 degrees Fahrenheit (600 degrees Celsius). During that phase change, the solid expands which is picked up by the measurement. After the phase change is complete, and with additional cooling, the displacement resumes. In Figure 10 below, the displacement of D1 and D3 are shown. This movement mimics the deformation shown by D2 and D4 is the movement/distortion of the flask and not crack opening. As the stresses build, the end plates are expected to bend inward. This inward bending accounts for approximately 0.04” (1mm) of the final movement of probes D2 and D4. Again the phase transformation can be seen to relax the displacement of the end plates.

Figure 11 shows the movement of D5 which tracks the movement in the direction of the gating. This probe is moving toward the gating system showing that the gating is providing some restraint in spite of the casting’s design to minimize this movement. This probe breaks ~10 minutes into cooling, due to shearing possibly due to the crack growing or the phase change. It has been estimated from the other experiments that the magnitude of this deformation should be 0.04”-0.06” (1 - 1.5 mm).

Using the displacements from probes D1-D4 the displacement of the casting was corrected for distortions of the flask. This “zeroed” measurement is shown in Figure 12. The zeroed measurements for probes D2 and D4 show the same pattern from before but exhibit that the final distortions are likely due to the end plates flexing and not further opening of the crack. Perhaps this reveals that the crack reaches the final size during or just after the phase change.

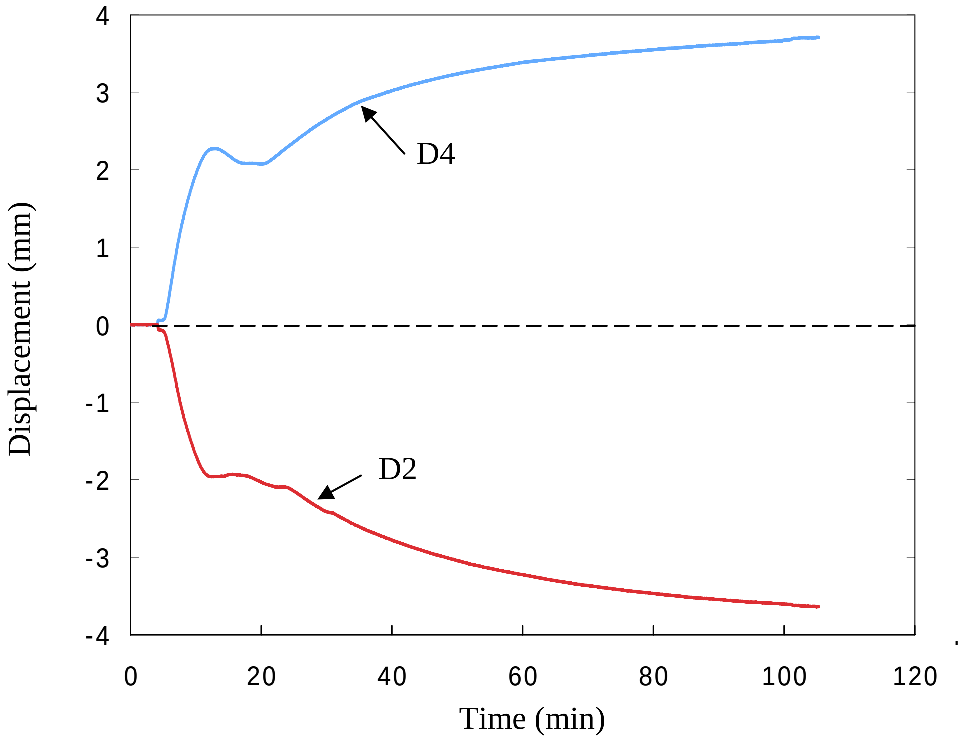

Figure 9. D2 and D4 displacement curves for casting 5.

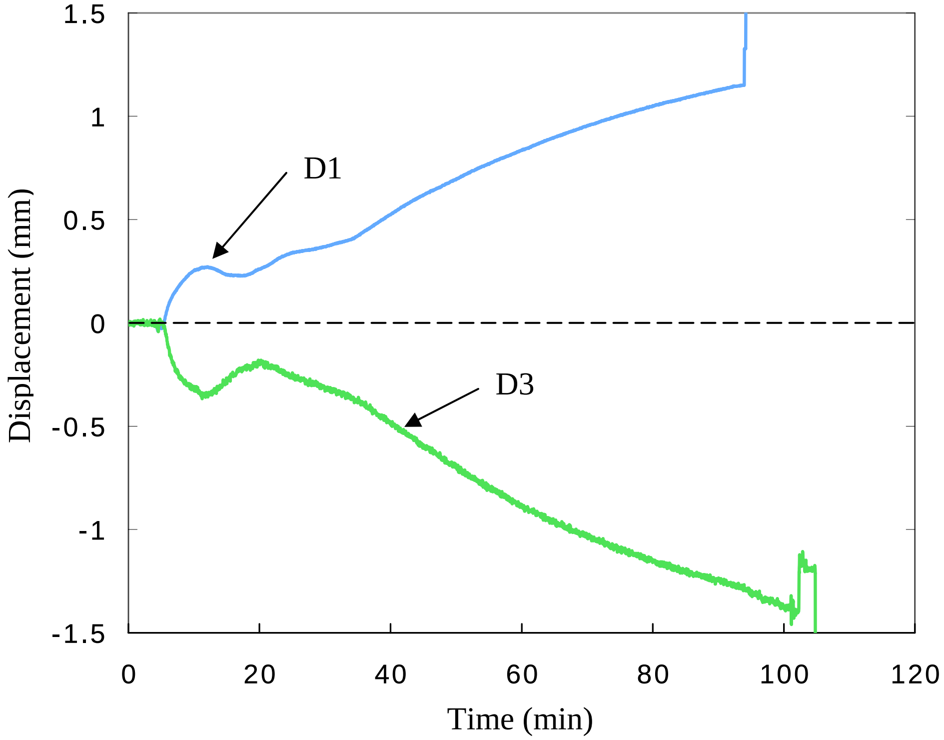

Figure 10. D1 and D3 displacement curve for casting 5.

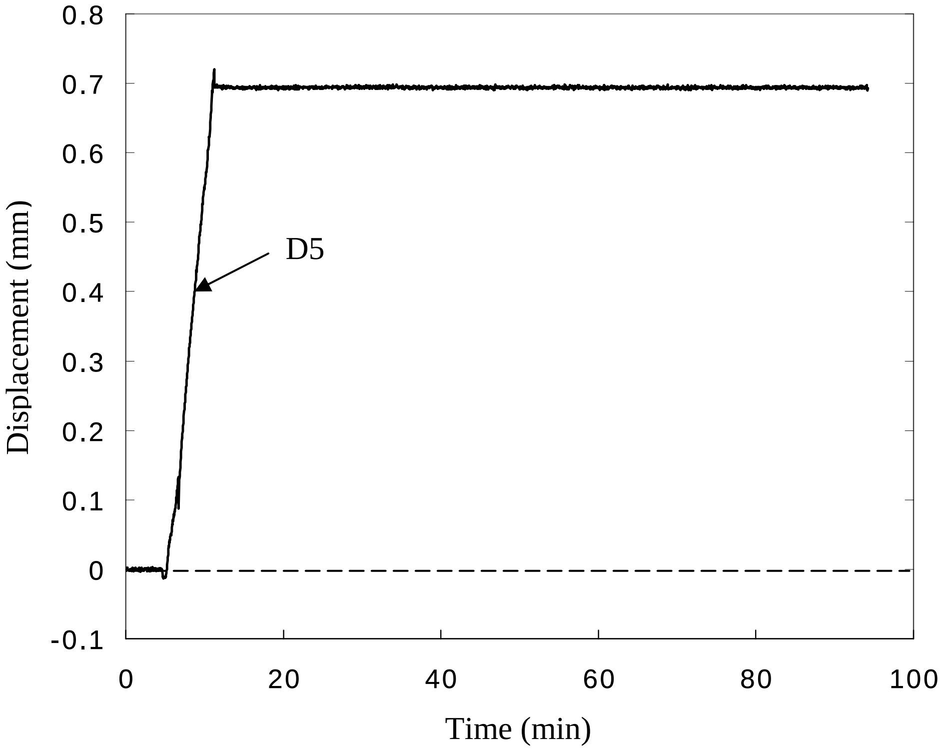

Figure 11. D5 displacement curve for casting 5.

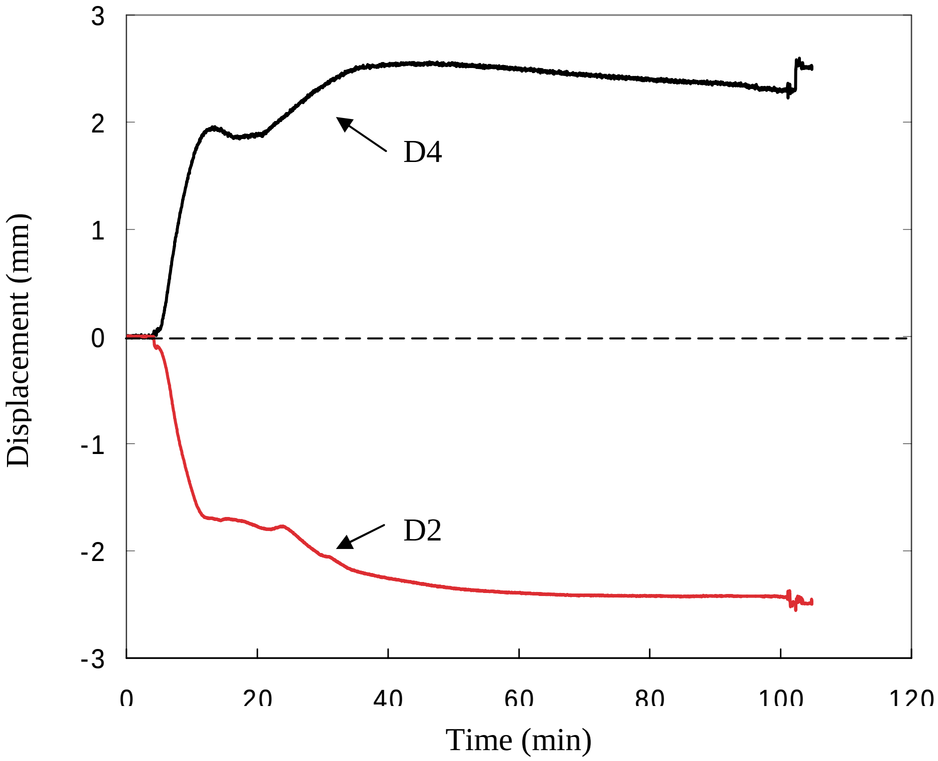

Figure 12. Zeroed D2 and D4 displacement curves for casting 5.

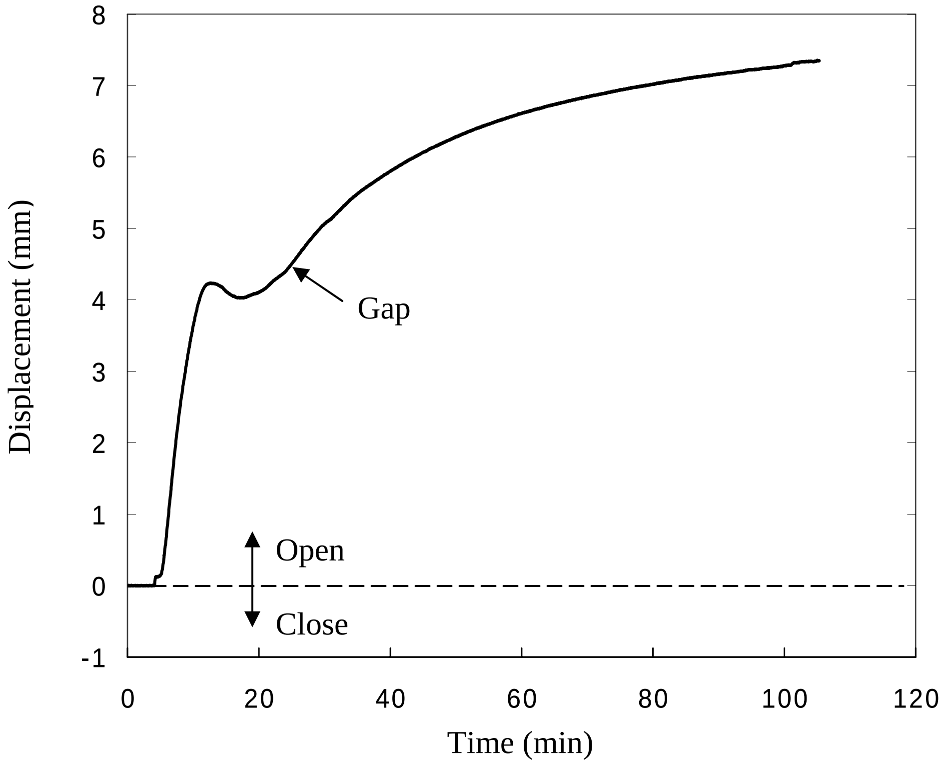

Figure 13. Gap displacement curve for casting 5.

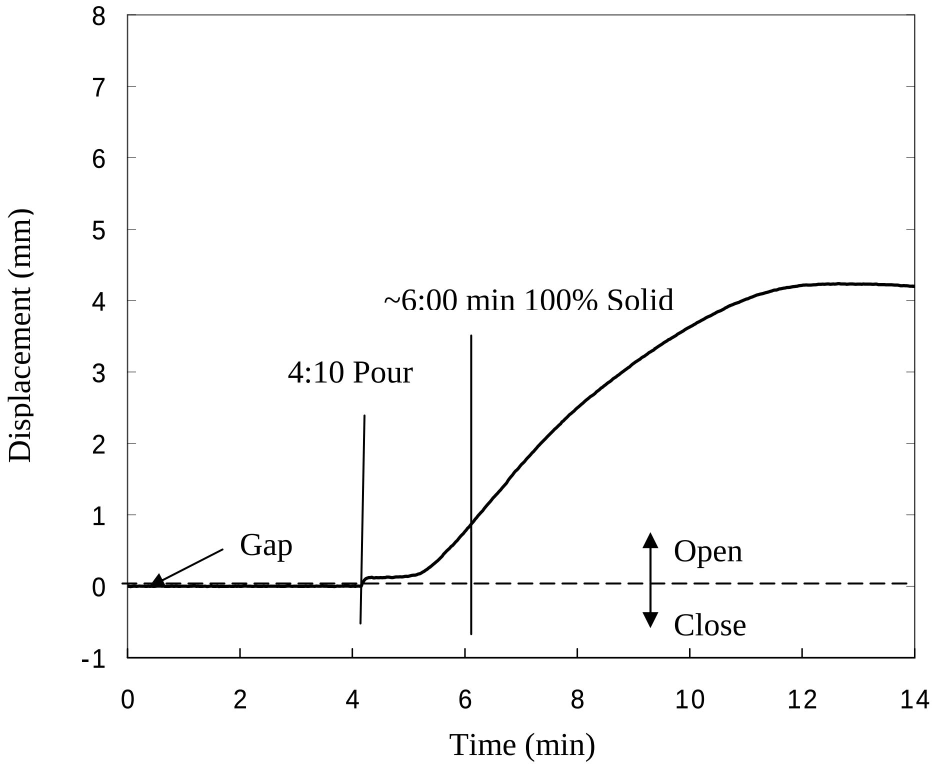

Figure 14. Gap displacement curve zoomed in for first 14 minutes for casting 5.

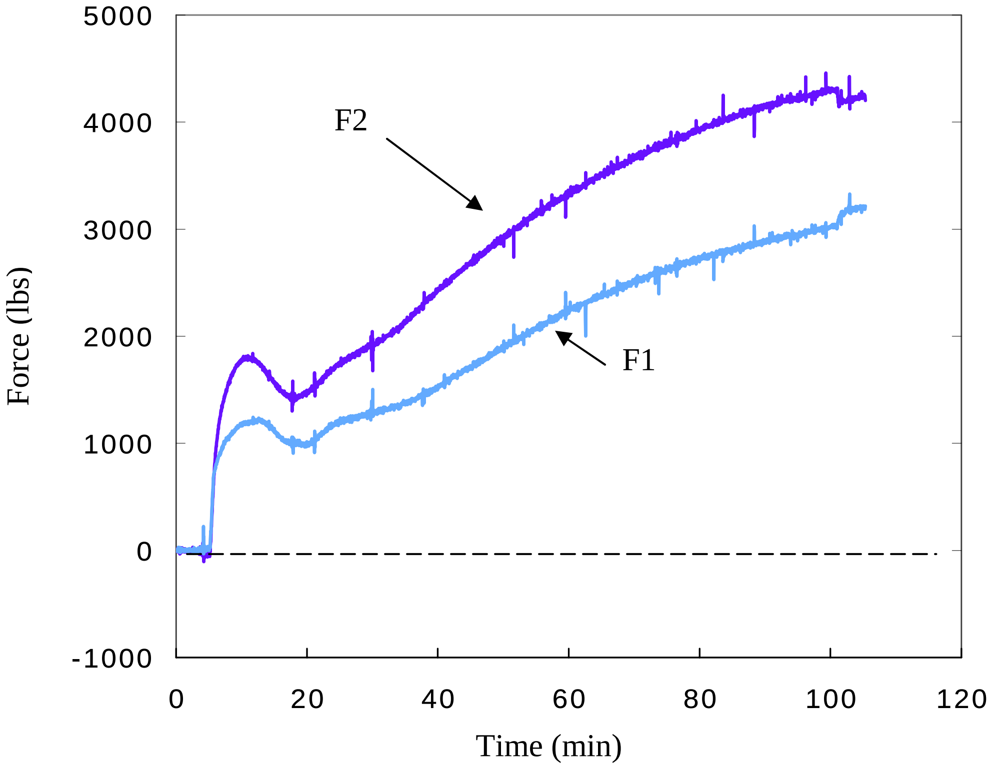

Figure 15. Force curve for casting 5.

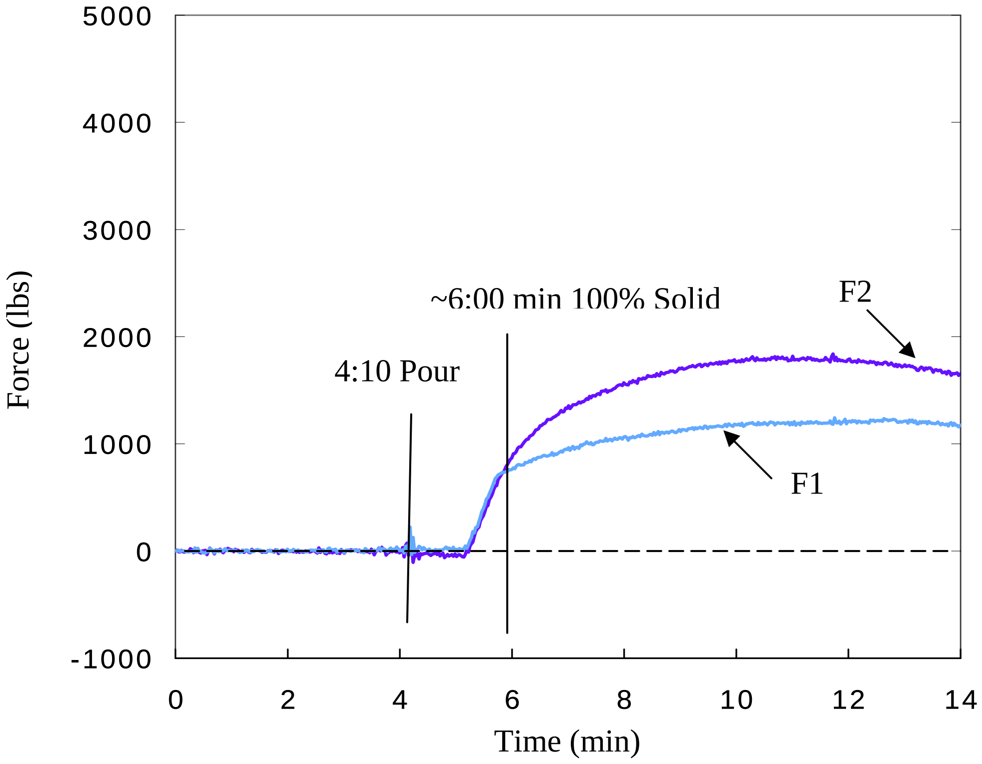

Figure 16. Force curve zoomed in for the first 14 minutes for casting 5.

Figure 13 shows the evolution of the gap size during the experiment. The gap displacement is the change in the “gauge section” of this experiment or the difference in the D2 and D4 probe displacement. The gap displacement measurement for this casting is analogous to a monotonic tension or Gleeble to determine mechanical properties. Although the boundary conditions are different, this test casting measures the forces and strains around a “gauge section” and from the results, temperature dependent yield strength, elastic, and creep properties can be determined. This curve demonstrates many of the previous features of the individual curves including the phase change, crack opening, and growth. Figure 14 looks at the first 14 minutes of Figure 13, showing the gap displacement during solidification. The crack appears to begin to open up about 1 min into solidification.

Figure 15 shows the development of forces for the casting. Two force gauges are used for redundancy. In a perfect test environment, both forces should be the same. However, the forces are different late into cooling. It is believed that this is due to the flask hanging on the mold in an unexpected way. In Figure 16 showing the zoomed-in region, the forces are seen to be identical early in experiment and then deviate roughly at the end of solidification. Although the crack may further confound the force direction, the primary reason for this deviation is believed to be due to some hanging of the flask on the mold.

Comparison of all Castings

Figure 17 shows the comparison of the gap displacement for all the 1” wide arm section castings. The gap displacement is a measure of change in the “gauge section” which directly translates to mechanical properties. Note that all of the castings go through the phase change mentioned in the detailed results section at about the same time. This is expected considering the similarity of the section for all the 1” arm sections. All the gap displacements grow with time; this is expected for the restrained castings. The unrestrained casting contracts, this means that the gap is shrinking. Casting 5 develops the hot tear and has the greatest gap opening. Comparing castings 3 and 4, even though casting 4 did not hot tear the larger hot spot contributed to a larger gap opening than in casting 3.

Figure 18 shows the comparison of the gap displacement for all of the 2” wide arm section castings. The gap opens early in cooling. This is similar to the previous figure but less in magnitude, after which the phase change occurs and the gap closes. The additional mass of the 2” arm lengthens the phase change period by about double the time. The gap closes about 0.08” (2mm) which is approximately double the 1” arm. The total gap displacement is smaller than the 1” arm sections, but this is probably due to the difference in the early displacement which is smaller.

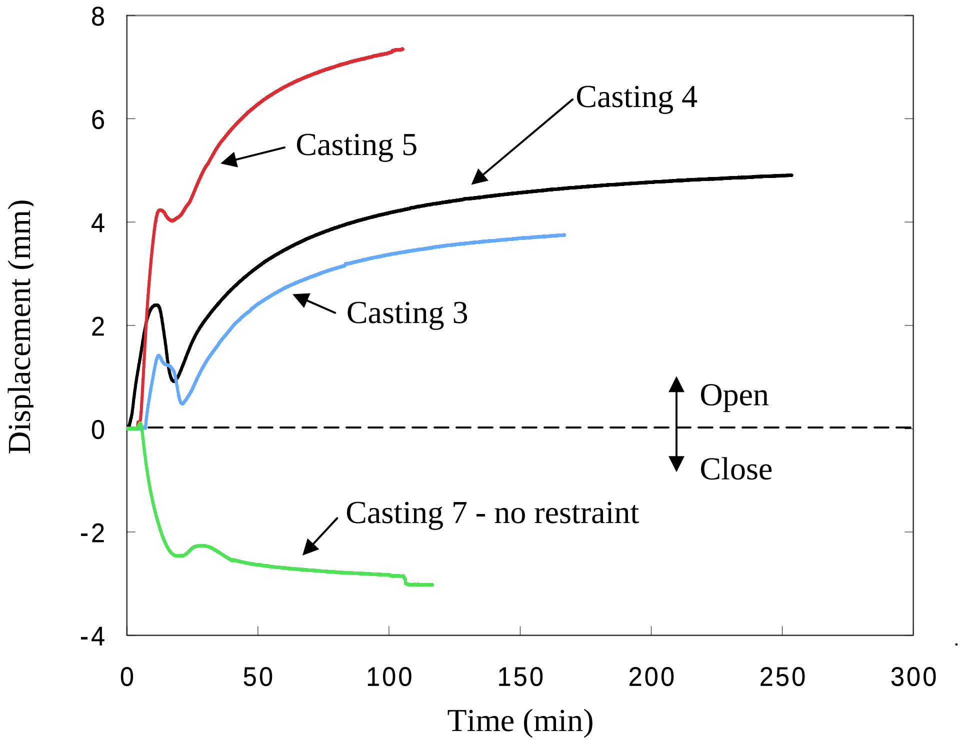

Figure 17. Gap displacement curve for 1” arm castings 3, 4, 5 and 7.

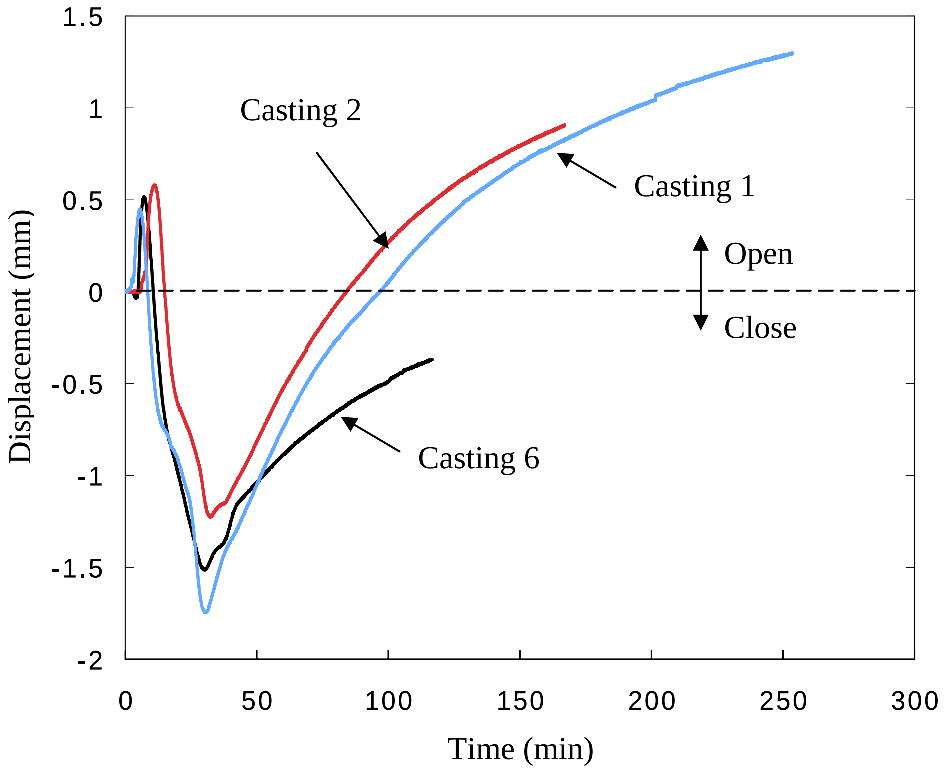

Figure 18. Gap displacement curve for 2” arm castings 1, 2 and 6.

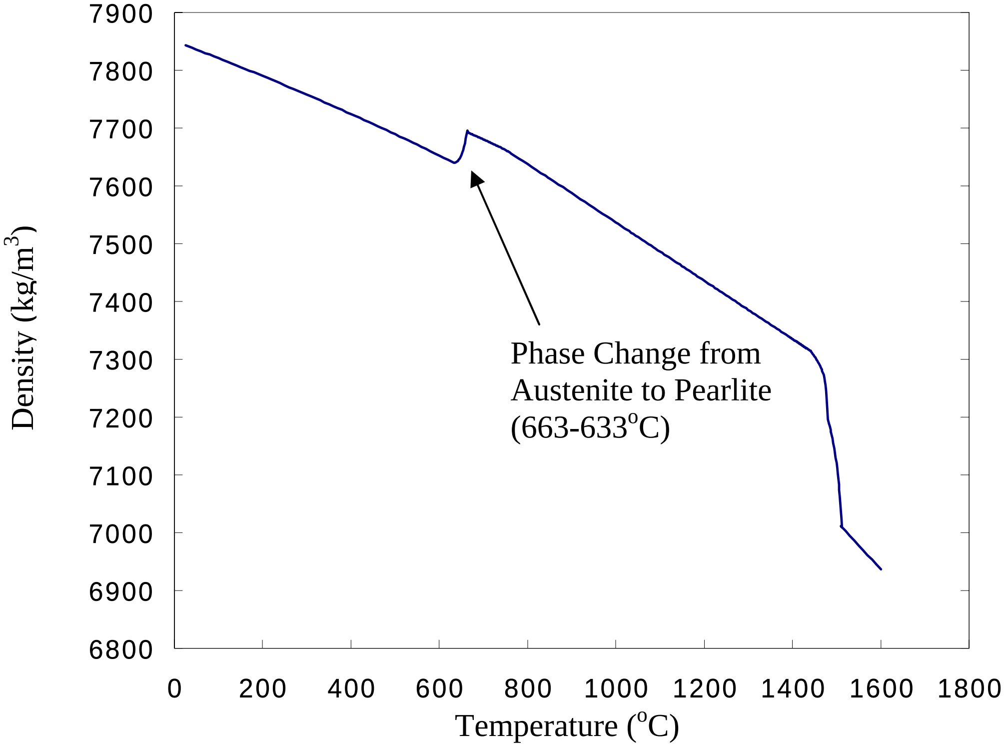

Figure 19. Density curve used in simulation illustrating the phase change region.

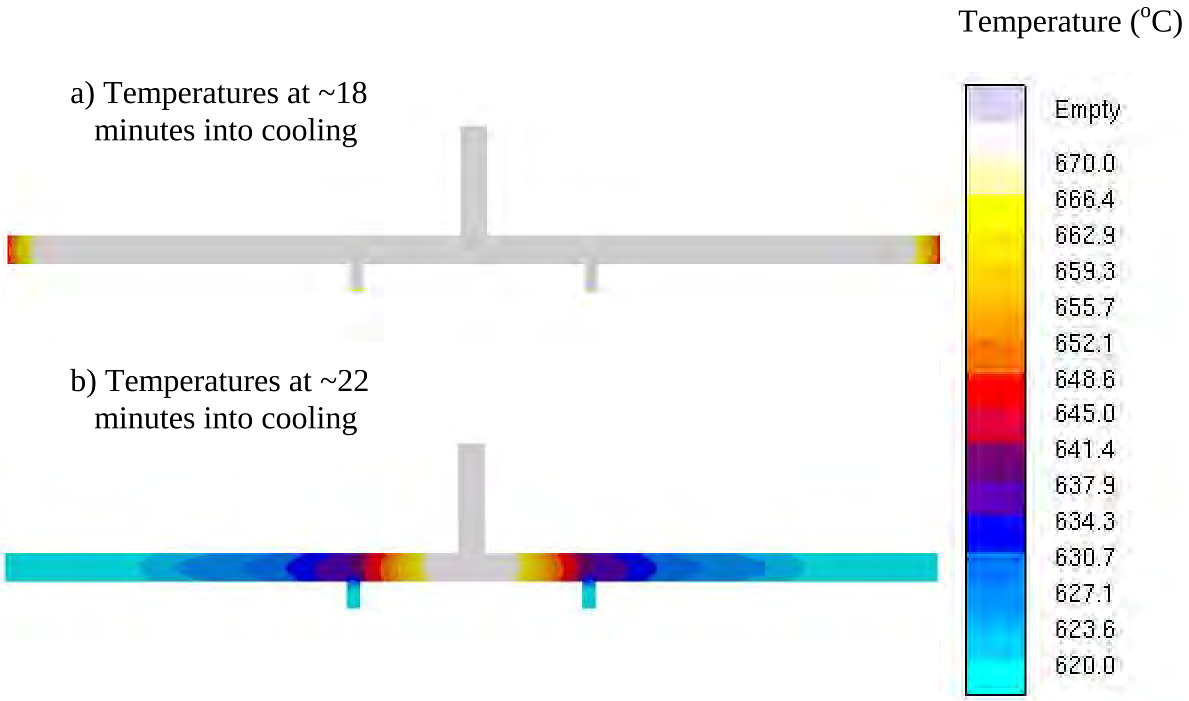

Figure 20. Temperature profiles from the simulation for times before phase change (a) and after (b).

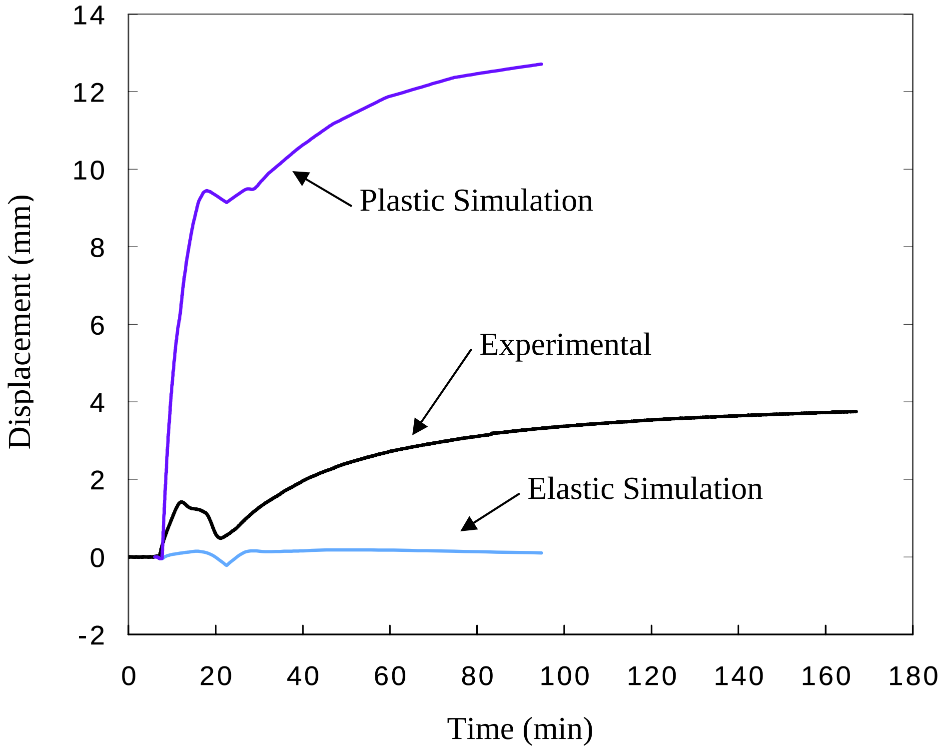

Figure 21. Gap displacement curve comparing experimental and simulated results.

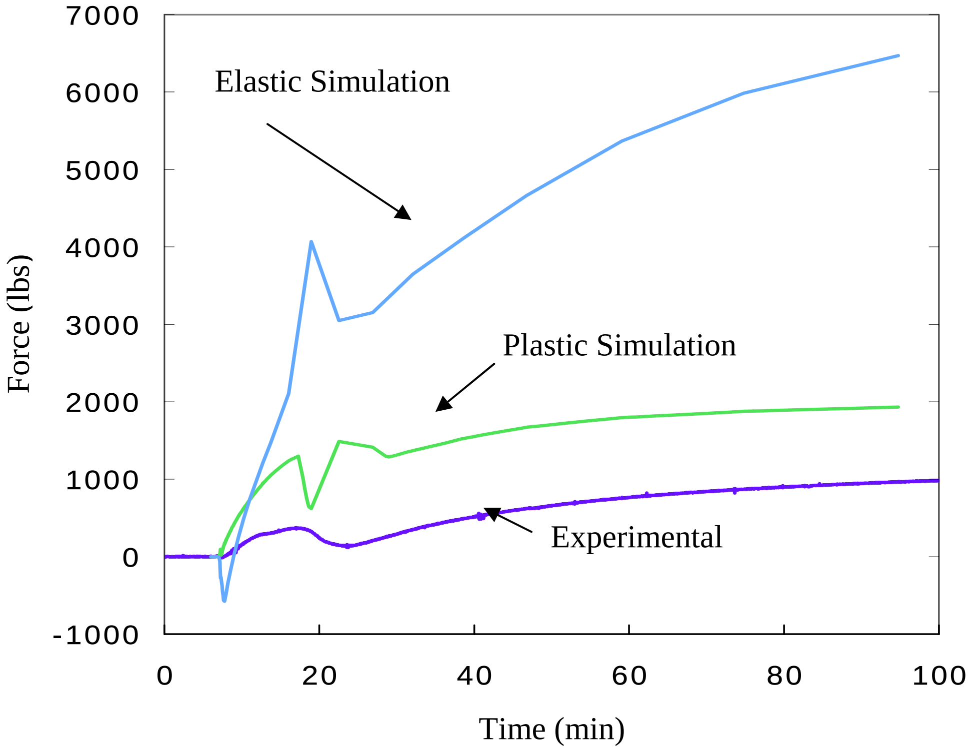

Figure 22. Force curve comparing experimental and simulated results.

Comparison of simulation

Two simulations were run to make a quick comparison to the experimental results. A more sophisticated model which also considers hot tears is in development but this full model is not yet complete. Therefore, the comparison will be made for a casting that does not hot tear. The temperature and solidification simulation was run using MAGMAsoft. The displacement and force simulation was run using the finite element program, ABAQUS. Two different material models were used, the first was a completely elastic model and the second was a plastic model. Both had temperature dependent properties and the same thermal expansion curves. The thermal properties were generated using the code IDS for the chemistries poured. The temperature dependent mechanical properties were obtained from the general MAGMAsoft property dataset. The density curve is shown in Figure 19 for low alloy chemistry. The phase change from Austinite to Pearlite can be seen at around 650 degrees Celsius. The temperature profiles in the simulated casting are also shown in Figure 20. Two times, one before the onset of phase change and another after phase change, illustrate that the phase change happens almost completely in four minutes.

Figure 21 shows the comparison of the gap displacement for the experimental results and simulation of casting 3. All of the deformation and stress development in the casting is due to the accumulation of thermal strains upon cooling. The temperature simulation is used as an input to the stress simulation. Then using the density curve, the temperature is changed to thermal strain and the deformation and stress is calculated. In the elastic simulation, the gap displacement is small. This small displacement is attributed to the nearly isothermal cooling of this casting. If the casting were to cool at only one temperature then the casting would also uniformly contract and the elastic deformation would show no gap movement. Even though the casting is nearly isothermal, the non-homogenous temperature does cause a slight feature in the gap displacement near the phase change region showing that something is happening during the cooling.

In the plastic simulation, the gap displacement is much larger than seen in the experiment. This is due to the poor agreement between the simulation and actual properties. When the simulated yield stress is artificially low compared to the actual yield stress, the gap deformation is expected to be greater than anticipated. In addition, the boundary conditions used in simulation were zero displacement at the ends; this may over-constrain the simulation. In an over-constrained simulation, the forces will be higher and then again the deformation will be greater than expected. Both issues are being investigated. However, the plastic deformation curve shows that the phase change can be accounted for in a simple way. Also the gap is always opening which is also consistent with the experimental results.

In Figure 22, the forces are also compared for the simulation and experimental results. The force is much harder to match to the experimental results because small changes in the boundary conditions may change both the measured or simulated force. Consider the detailed review of casting 5; in that case the forces were not equal because it is suspected that the flask hung up on the mold. For casting 3 only one force measurement is available, therefore no judgment can be made about this. Also in the simulation, a fully constrained boundary is used to ensure that no rigid body motions are calculated. However, this may over constrain the casting, causing higher forces internally. These issues are currently being investigated. The elastic curve is greater than the plastic because of the plastic yielding. In a qualitative sense, the forces both simulated and experimental behave similarly; always rising except during the phase change.

Discussion

Since the first successful hot tear test casting, the T-section casting has been poured again with refined instrumentation in order to further investigate the distortion and hot tearing of steel castings. The additional measurements provide insights into the fundamentals of hot tearing and also allow comparison to developing simulation. The initial results agree with current understanding.

Comparisons of these results to the simulation show the need to improve the model. First, improvement of the mechanical properties is necessary for better agreement. Second, the understanding of the boundary conditions applied must be improved. Additional improvement could be gained by including a model for prediction of hot tears, or mechanical porosity creation if no crack propagates.

Acknowledgements

This work was prepared with the support of the U.S. Department of Energy (DOE) Award No. DE-FC36-04GO14230. However, any opinions, findings, conclusions, or recommendations expressed herein are those of the authors, and do not necessarily reflect the views of the DOE. The authors wish to thank the Steel Founder’s Society of America, especially Malcom Blair and Raymond Monroe for their assistance in this work. Also, we thank the member foundry and the University of Northern Iowa, which participated to make the pattern, castings, and to work out the bugs in the experiment.

References

1. C.W. Briggs, Elements of Design for Prevention of Hot Tearing in Steel Castings, *Steel Founders’ Society of America Research Report*, No. 38, Technical Research Committee, SFSA, February 1957.

2. C. E. Bates, Effects of Melt Practice, Core Binder, and Core Density on Hot Tearing of Cast Steel, *Steel Founders’ Society of America Research Report*, No. 103, Technical Research Committee, SFSA, January 1991.

3. P. Alexandre, A. Goudot, A. Ben Cheikh, J.B. Dalin Renault, D. Celentano, S. Oller, E. Onate: “Experimental and Numerical Analyses of Thermomechanical Behavior of Sand Cast Iron During Solidification”, pg 237-244, Modeling of Casting, Welding and Advanced Solidification Processes V, edited by M. Rappaz, M.R. Ozgu, and K.W. Mahin, The Minerals, Metals, & Materials Society, 1991.

Monroe, C., and Beckermann, C., “Deformation During Casting of Steel: Mold and Material Properties,” in Proceedings of the 61st SFSA Technical and Operating Conference, Paper No. 5.6, Steel Founders' Society of America, Chicago, IL, 2007.

Deformation during casting of steel: model and material properties

C. Monroe
C. Beckermann
Department of Mechanical and Industrial Engineering
The University of Iowa, Iowa City, IA 52242

Abstract

Dimensional differences between a final casting and its design are casting distortions. Distortion is created by the deformation occurring throughout solidification and further cooling during the casting process. Accurate prediction of casting distortion should be found through modeling the entire deformation. Modeling requires the knowledge of casting process conditions, material properties, mold restraint, and other factors. Solidification and further cooling simulation uses above process details to obtain temperatures. From the temperatures, the transient deformation and final distortions can be calculated. A generic mechanical property data set for low alloy steel is presented and the result of simulating deformation is compared to experimental measurements. This property data set was developed for a yield stress model that includes strain hardening and strain rate dependence.

Introduction

Distortion in any steel casting is costly. Added operations are required to finish the casting. Corrective changes to the design or the pattern tooling is done by trial and error. Process fluctuations can cause episodic appearances of unacceptable distortion during production. Prediction and a fundamental understanding of distortion are important when trying to control any part or process.

Casting simulation is used to predict solidification and cooling results. Understanding the process allows a casting designer or producer to make decisions that affect either the part or the rigging to optimize quality. Casting simulation tries to use physically realistic models without overtaxing the computer. The simulations need to give usable results in the shortest time possible. Simulating casting distortion has been done using (fast to simulate) simplified mechanical models that gave incorrect simulation results. This is true for hot tear modeling, where inadequate mushy zone modeling limited our ability to predict hot tears. Improving the mechanical models has been an incremental process. With each improvement, the predictions become a challenge to calculate in a fast and robust manner.

The latest progress in improvement is a yield stress model that incorporates isotropic strain hardening and strain rate dependent hardening. Temperature dependent material properties will be presented for this yield stress model. Then a casting example from a previous T&O illustrates the simulation process [1]. The new yield stress model is progress toward a more realistic model; but a final model with validation is not presented.

Method

The summary in Figure 1 shows an overview of the sequence of casting simulation modules. Casting simulation starts with a geometry defined by a CAD model of the casting, mold, gating, chills, risers, padding, etc. Geometric features and other variables are specified. Using the Preprocessor, this geometry is input into the casting simulation software where other information relating to the molten metal chemistry, pouring temperature, flow properties, thermodynamic properties, and mechanical properties must be set.

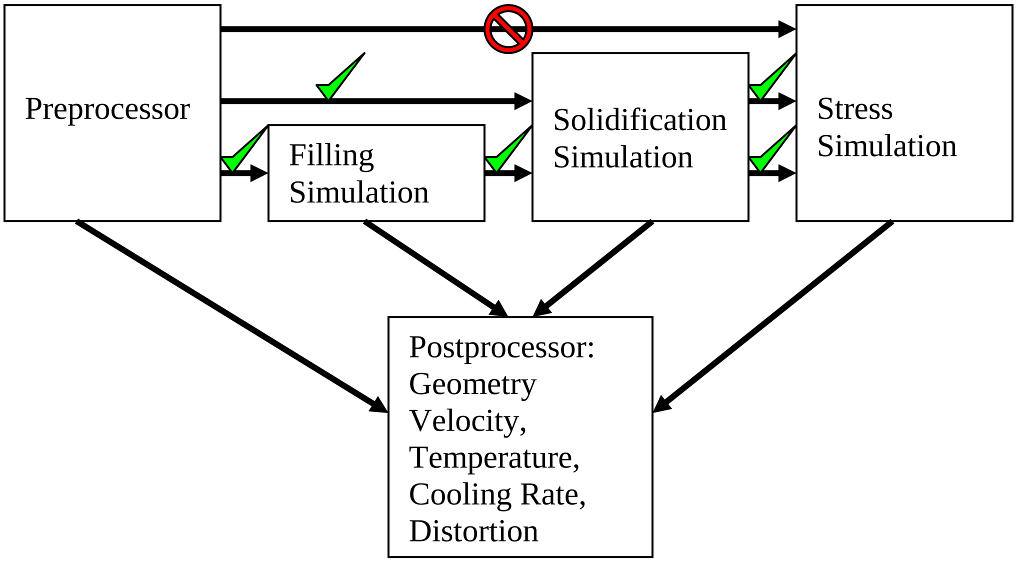

Figure 1. Flow diagram of the interrelationship of casting simulation modules.

After the CAD geometry is entered, the filling of the casting can be simulated. Once the filling event is modeled, the heat transfer during casting can be solved. The heat transfer calculation gives the temperature and porosity during solidification and further cooling. Porosity results are used to evaluate the casting soundness. Only after computing the temperatures and porosity can the deformation be evaluated. When deformation prediction is needed, an additional simulation is run. Temperature and porosity both drive deformation by casting shrinkage. In reality, deformation occurs at the same time as the temperatures are dropping and porosity is forming. It is usually accepted to calculate the deformation in a sequence and not as a codependent calculation. The validity of the distortion prediction is dependent on representative simulation results obtained for the temperature and porosity. Not only representative final results are needed, but the entire calculated history must be validated to predict the final casting shape and residual stresses.

Process measurements may verify the accuracy of the calculated values. For example, the temperature determined by a thermocouple is a check on the heat transfer calculation. The thermocouple data comparison ensures that the properties, simulation setup, and the calculation are all accurate. For deformation calculations, a “distortion probe” is necessary to check the simulation of strain. By checking the simulation of deformation against experimental measurement, again the properties, setup, and calculation may all be validated. Once the simulation of the distortion is confirmed, then unwanted distortion of the casting may be reduced through design changes in the model. Using the deformation model to minimize unwanted distortion is the same as using thermal modeling of solidification to reduce shrinkage porosity. Validation of the deformation simulation motivates the casting experiments.

Material Mechanical Model

Mechanical properties vary with temperature, composition, cooling rate, etc. Obtaining usable mechanical properties up to the mushy zone temperatures is one challenge in the simulation of deformation. Three uni-axial tensile tests are shown schematically in Figure 2. Test A in the figure shows a test with a constant yield stress. Because no hardening occurs, the loading path ramps up in stress along the elastic slope initially. After reaching the yield stress, the loading continues yielding at a constant value. Test B in the figure shows the same loading path with the same initial yield stress but with strain hardening. Hardening acts to increase the yield stress with additional deformation. Test C illustrates a test, which has the same conditions as test B, at a higher strain rate. At high temperatures, the strain rate dependence is a viscous or creep problem. Creep describes materials that accumulate strain faster at increasing constant loads. The difference between test C and test B shows that while the strain hardening is similar, the strain rate dependence or creep requires a higher yield stress at a higher strain rate.

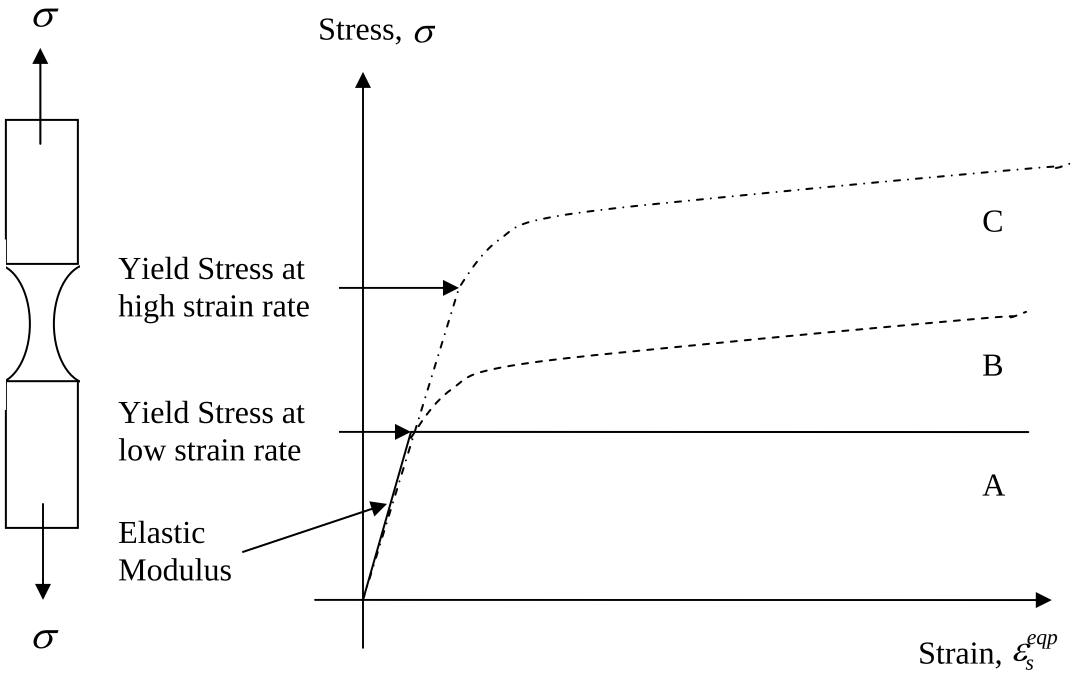

Figure 2. Schematic of a uni-axial stress-strain curve showing hardening and strain rate dependence.

The mechanical model used to describe the above process in uni-axial deformation begins with an assumption about the strains. This assumption is that the strain may be decomposed into three parts; the elastic, thermal, and inelastic (plastic or creep) parts. The equation is written as

$$\varepsilon = \varepsilon^{e} + \varepsilon^{th} + \varepsilon^{ie} .$$

The elastic strain behaves according to Hooke's law or

$$\sigma = C\varepsilon^{e} ,$$

where the elastic modulus is C and the stress is σ. The thermal strain is the integration of the change in density for the solid from the solidification temperature to the current temperature or

$$\varepsilon^{th} = \int_{T_{solidus}}^{T} -\frac{1}{\rho_s}\frac{\partial\rho_s}{\partial T}\,dT ,$$

where the solid density is ρ_s, the temperature is T, and the solidus temperature is $T_{solidus}$. The stress state is calculated using the elastic modulus until the stress exceeds the yield stress. Whether the yield state is reached is calculated using the equation

$$F = \sigma - Y ,$$

where the yield function is F and the yield stress is Y. This function is a scalar function that is always negative for elastic states, and is greater than zero when the inelastic strains are calculated. The inelastic strain is increased until the stress is reduced to match the yield stress. The inelastic strain required to keep the stress from exceeding the yield stress is found through the elastic equation above or

$$\sigma = C\left(\varepsilon - \varepsilon^{ie}\right).$$

A simple power law model may be used to describe the yield stress with hardening and creep. At lower temperatures, elastic properties are important. These properties are less determinative at high temperatures such as the temperatures in heat treatment or above. At high temperatures, yielding with hardening or creep dominates the deformation results. The following yield stress is used

$$Y\left(\varepsilon^{ie}, \dot{\varepsilon}^{ie}, T\right) = \sigma_o(T)\left(1 + \frac{\varepsilon^{ie}}{\varepsilon_o(T)}\right)^{n(T)}\left(1 + \frac{\dot{\varepsilon}^{ie}}{\dot{\varepsilon}_o(T)}\right)^{m(T)}$$

where the initial yield stress, $\sigma_o(T)$, the reference strain, $\varepsilon_o(T)$, the hardening exponent, $n(T)$, the reference strain rate, $\dot{\varepsilon}_o(T)$, and the strain rate exponent, $m(T)$, are all required to determine yielding. These values plus the elastic constants lead to a total of 7 temperature dependent properties that are needed to solve for deformation. This is not an unreasonable number of parameters. Many of these properties at room temperature are required to be determined for each heat by commercial specifications. Elastic modulus, initial yield stress, and hardening slope may all be obtained from a tensile specimen pulled at room temperature. The temperature dependent properties used for a generic low alloy steel will be presented. The model is similar to models proposed in any strength of materials book.

The above material mechanical model should be compared to previous yield definitions that are common in industry. The elastic modulus and Possion ratio, which are used to calculate the elastic strains, are the same as used historically. The yield stress model, however, is more elaborate. The additional features to account for hardening and creep effects may be turned off in this model by choosing the exponents that equal zero. In that case, the initial yield stress is the same as 0.2% yield stress that is obtained from room temperature tests. As a first approximation, the initial yield stress may always be chosen as the 0.2% yield stress. However as greater accuracy is required, especially at higher temperatures, the uni-axial tests should be fit at each temperature. The yield stress used when experimental curves are regressed may be much smaller than a 0.2% yield stress.

The material mechanical properties at room temperature up until 850 ^{o}C are obtained from the thermodynamic simulation software, Jmatpro 4.0 [2]. This software is supplemented at temperatures above 850 ^{o}C with experimental results of uni-axial tensile tests [3,4]. These two sources are joined piecewise at the common temperature to obtain consistent properties through the entire temperature range. The temperature dependent material inelastic properties above 850 ^{o}C are generated from completing a least-squares Levenberg-Marquardt minimization of simulated curves to the experimental points. A result comparing the experimental points to simulated uni-axial test is shown in Figure 3. The points represent the experimental measurement and the solid line is the calculated curve. Notice that the strain hardening is important in this test because the stress doubles from the small strain values to larger strains. The set of experiments consist of 102 uni-axial tensile tests which span 850 - 1450 ^{o}C, and 0.0 - 2.0 weight percent Carbon [wt%], 0.0 - 0.2 strain rate [in./in.]. Table 2 presents the linear fit of properties to the data as a function of temperature with the final coefficients.

Figures 4 and 5 show steel elastic properties, illustrating the property variation with temperature used in MAGMAsoft [5]. At low temperatures, the elastic modulus is high at about 205 GPa (29,700 ksi). As the temperature increases, the elastic modulus decreases to a low value at the highest temperature. As mentioned before, this variation is taken from Jmatpro 4.0 from room temperature to 850 degrees C. At higher temperatures, the property values are taken from the curve fit as given in published work [4]. These elastic properties are difficult to confirm. They may need additional revision based on experimental results relating the residual stresses to the high temperature deformation.

In Figure 5, the Poisson ratio increases in the solid from room temperature to the solidus temperature of the low alloy steel. Above the solidus temperature the ratio is not known. The variation of the Poisson ratio shown in the figure is multiplied by the solid fraction; note that the liquid, not the remaining solid, will be incompressible at the liquidus temperature (Poisson ratio equal 0.5).

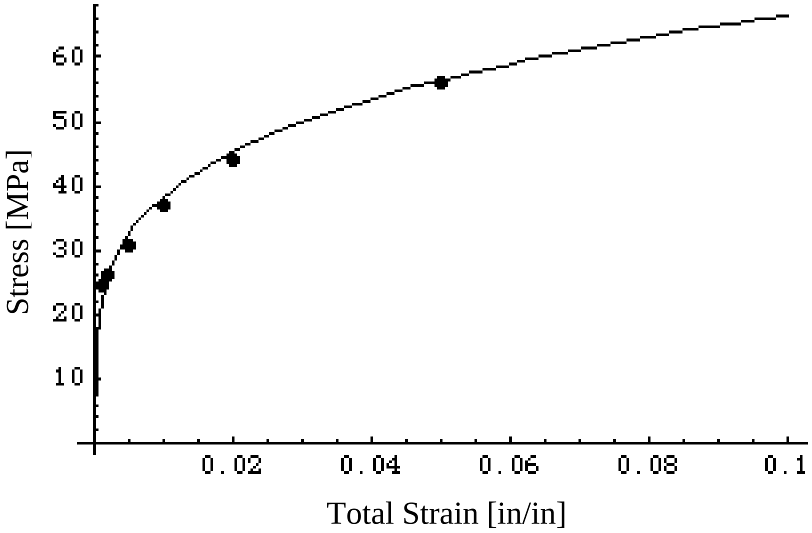

Figure 3. Typical result and curve fit for a single experiment.

Table 2. Equations for mechanical inelastic properties valid from 850 ^{o}C to 1400 ^{o}C

Property	Equation	Coefficient 1	Coefficient 2	Coefficient 3
Initial yield stress	$\sigma_o[\mathrm{MPa}] = a_1 + a_2 * T[K]$	$a_1 = 1.93993$	$a_2 = -8.75426 * 10^{-4}$	
Hardening exponent	$n = b_1 + b_2 * T[K] + b_3 * C[wt\%]$	$b_1 = 0.362363$	$b_2 = -1.05482 * 10^{-4}$	$b_3 = -2.67962 * 10^{-2}$
Reference strain	$\varepsilon_o = \dfrac{\sigma_o n}{E}$			
Creep exponent	$m = c_1 + c_2 * T[K] + c_3 * C[wt\%]$	$c_1 = -0.042048$	$c_2 = -1.38125 * 10^{-4}$	$c_3 = -7.32437 * 10^{-3}$
Reference strain rate	$\dot{\varepsilon}_o[\mathrm{s}^{-1}] = (d_1 + d_2 * T[K]) * \exp\left(\dfrac{Q}{T[K]}\right)$	$d_1 = 6438.2$	$d_2 = 11638.3$	$Q = 36000$

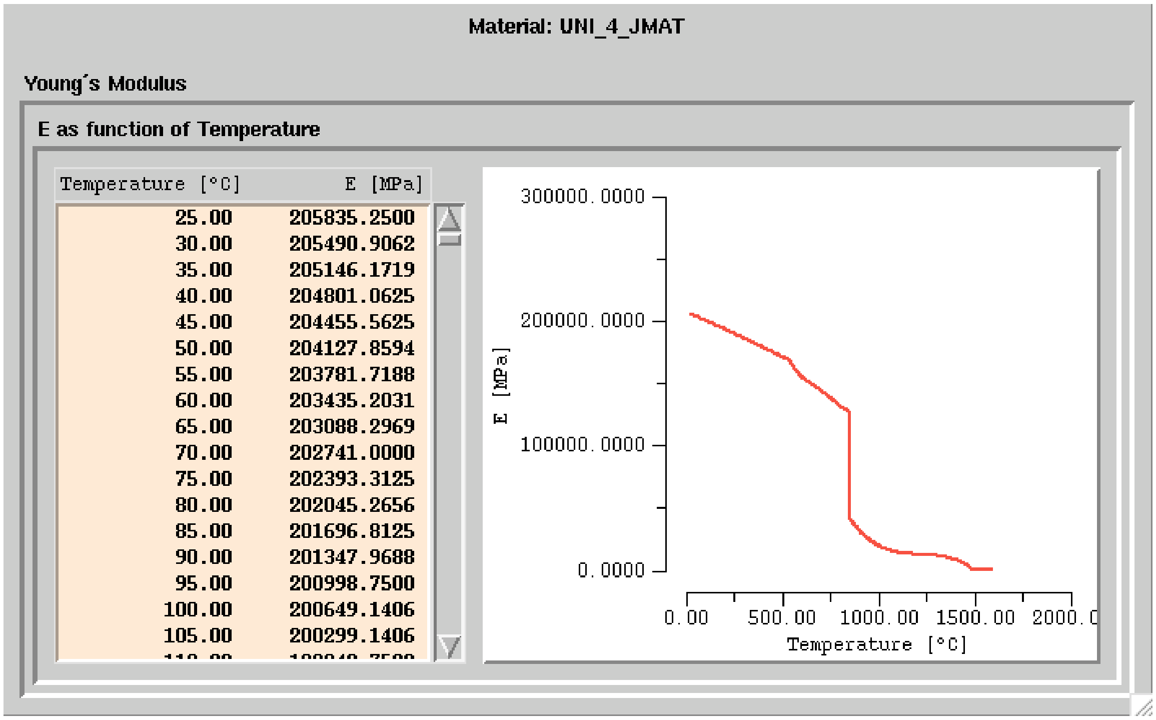

Temperature [°C]	E [MPa]
25.00	205835.2500
30.00	205490.9062
35.00	205146.1719
40.00	204801.0625
45.00	204455.5625
50.00	204127.8594
55.00	203781.7188
60.00	203435.2031
65.00	203088.2969
70.00	202741.0000
75.00	202393.3125
80.00	202045.2656
85.00	201696.8125
90.00	201347.9688
95.00	200998.7500
100.00	200649.1406
105.00	200299.1406

Figure 4. Low alloy steel elastic modulus curve variation against temperature. Note that at 850 ^{o}C the elastic modulus is joined piecewise from Jmatpro and previous published data [2,4].

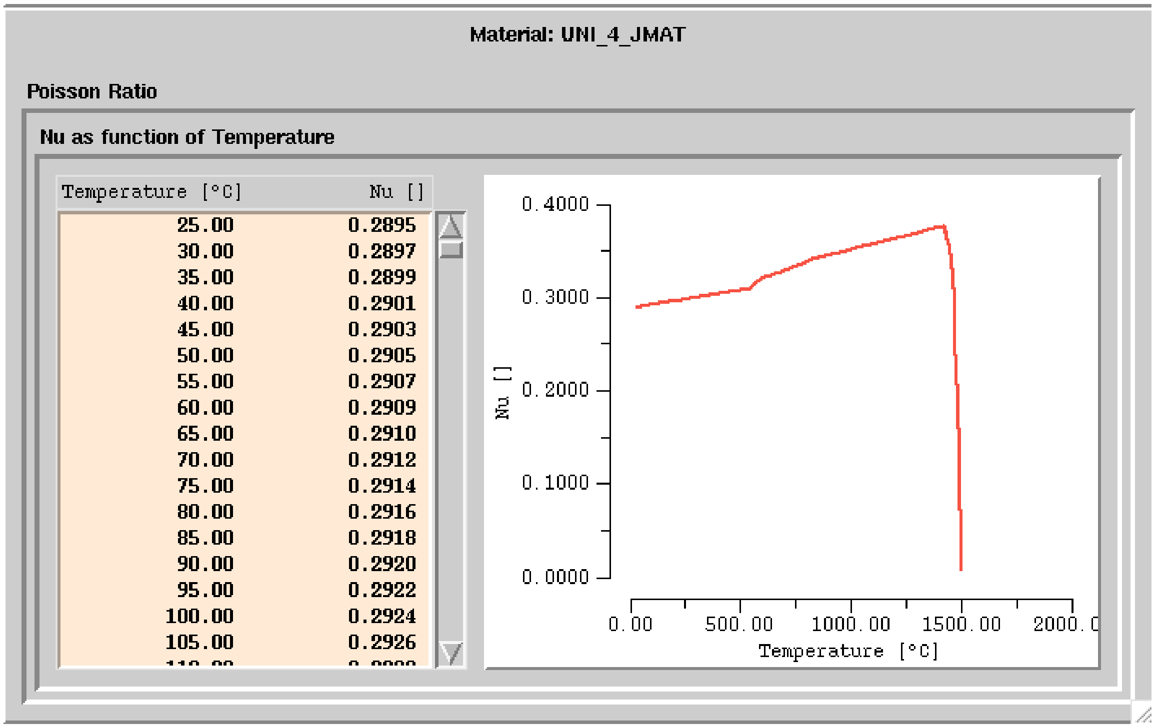

Temperature [°C]	Nu []
25.00	0.2895
30.00	0.2897
35.00	0.2899
40.00	0.2901
45.00	0.2903
50.00	0.2905
55.00	0.2907
60.00	0.2909
65.00	0.2910
70.00	0.2912
75.00	0.2914
80.00	0.2916
85.00	0.2918
90.00	0.2920
95.00	0.2922
100.00	0.2924
105.00	0.2926

Figure 5. Low alloy steel Poisson ratio curve variation against temperature.

Figures 6 and 7 show plastic steel properties. In Figure 6, the yield stress at room temperature is determined by a tensile test. This value taken from Jmatpro is about 250 MPa (36 ksi). At high temperatures, the value of the initial yield stress decreases. The yield stress above 850 ^{o}C is not the same as the 0.2% offset yield stress. The initial yield stress was found by analyzing the experimental data published in reference 3. In Figure 7, the inverse of hardening exponent is shown. In MAGMAsoft, the inverse hardening exponent is used rather than the exponent shown in the above equation for the yield stress. The inverse hardening exponent increases with temperature. The reference strain is not shown in a figure because it is calculated from the other parameters. The formula for the reference strain is shown in Table 2. These plastic parameters may be used without the rate dependent part by setting the rate dependent exponent to zero.

Figures 8 and 9 show the rate dependent or creep properties. Strain from creep causes heat treatment distortion and relaxation of the residual stresses. In casting, creep is not as significant due to the low strain rates from smaller cooling rates as compared to heat treatment. The strain rate exponent increases with temperature as shown in Figure 8. Below 850 ^{o}C, the strain rate exponent is set to zero. Figure 9 shows the reference strain rate, which assumes some activation energy and coefficient. The reference strain rate decreases according to an Arrhenius law to a constant minimum value at low temperatures. These are summarized in Table 2.

In the next section, the rate dependence is not considered. Instead the creep exponent is set to zero at all temperatures. All the other properties are used as shown. MAGMAsoft currently allows no rate dependence. Therefore, current capability is demonstrated pending further model improvement. The following casting example shows the temperature and distortion results for comparison but not for validation purposes.

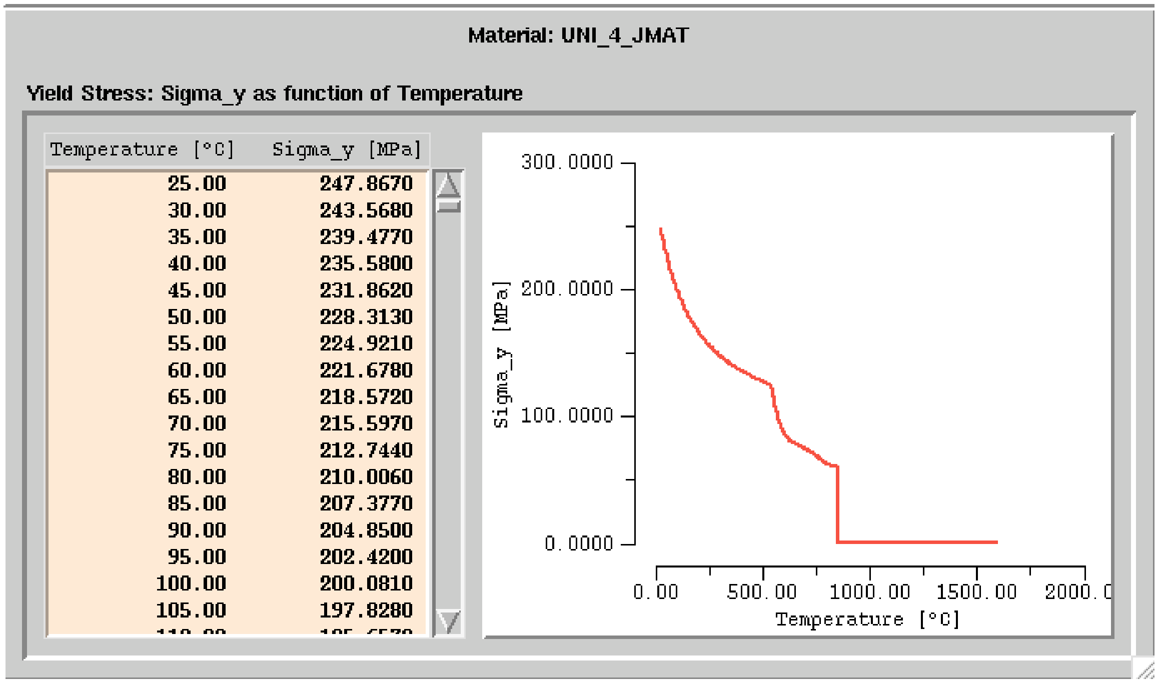

Material: UNI_4_JMAT

Yield Stress: Sigma_y as function of Temperature

Temperature [°C]	Sigma_y [MPa]
25.00	247.8670
30.00	243.5680
35.00	239.4770
40.00	235.5800
45.00	231.8620
50.00	228.3130
55.00	224.9210
60.00	221.6780
65.00	218.5720
70.00	215.5970
75.00	212.7440
80.00	210.0060
85.00	207.3770
90.00	204.8500
95.00	202.4200
100.00	200.0810
105.00	197.8280

Figure 6. Low alloy steel initial yield stress (not a 0.2% offset yield) curve variation against temperature.

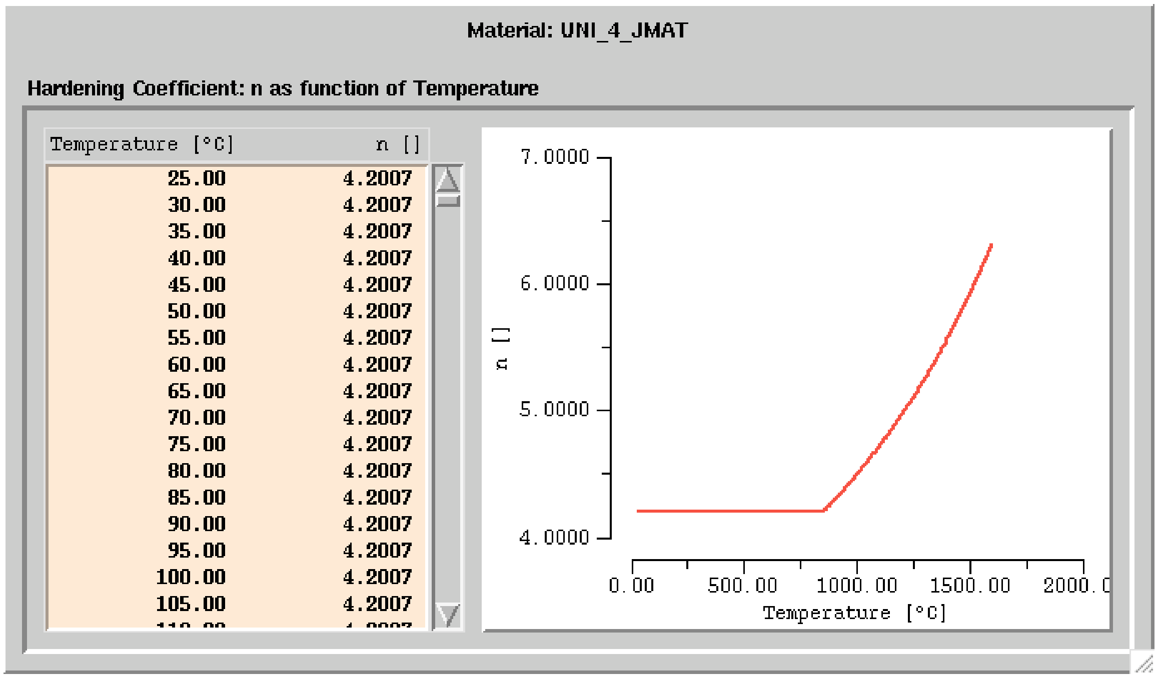

Material: UNI_4_JMAT

Hardening Coefficient: n as function of Temperature

Temperature [°C]	n []
25.00	4.2007
30.00	4.2007
35.00	4.2007
40.00	4.2007
45.00	4.2007
50.00	4.2007
55.00	4.2007
60.00	4.2007
65.00	4.2007
70.00	4.2007
75.00	4.2007
80.00	4.2007
85.00	4.2007
90.00	4.2007
95.00	4.2007
100.00	4.2007
105.00	4.2007

Figure 7. Low alloy steel inverse hardening exponent curve variation against temperature.

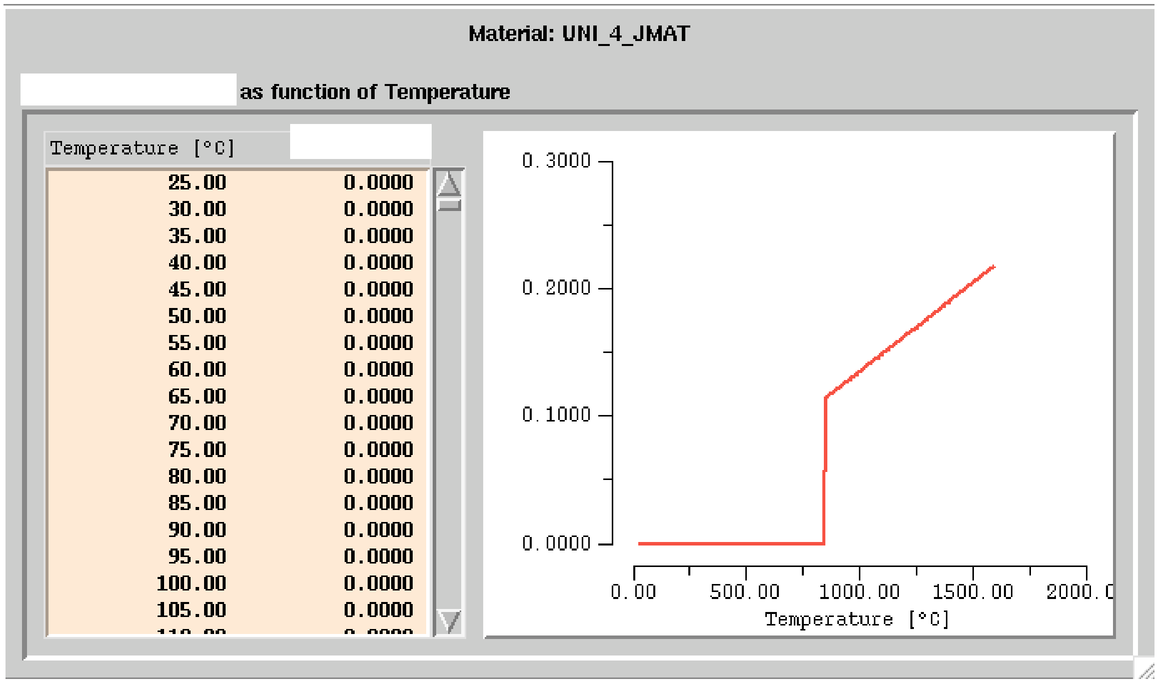

Material: UNI_4_JMAT

as function of Temperature

Temperature [°C]	
25.00	0.0000
30.00	0.0000
35.00	0.0000
40.00	0.0000
45.00	0.0000
50.00	0.0000
55.00	0.0000
60.00	0.0000
65.00	0.0000
70.00	0.0000
75.00	0.0000
80.00	0.0000
85.00	0.0000
90.00	0.0000
95.00	0.0000
100.00	0.0000
105.00	0.0000

Figure 8. Low alloy steel strain rate exponent curve variation against temperature.

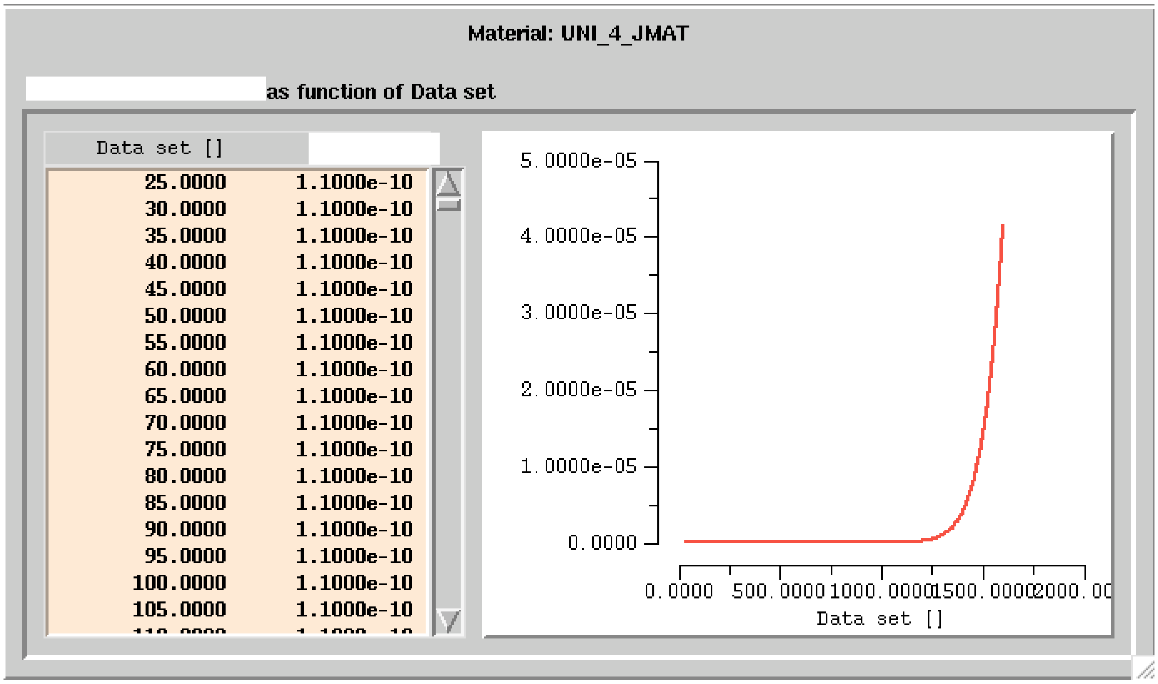

Material: UNI_4_JMAT

as function of Data set

Data set []	
25.0000	1.1000e-10
30.0000	1.1000e-10
35.0000	1.1000e-10
40.0000	1.1000e-10
45.0000	1.1000e-10
50.0000	1.1000e-10
55.0000	1.1000e-10
60.0000	1.1000e-10
65.0000	1.1000e-10
70.0000	1.1000e-10
75.0000	1.1000e-10
80.0000	1.1000e-10
85.0000	1.1000e-10
90.0000	1.1000e-10
95.0000	1.1000e-10
100.0000	1.1000e-10
105.0000	1.1000e-10

Figure 9. Low alloy steel reference strain rate curve variation against temperature.

Casting Example

The casting example shown demonstrates a comparison using a “distortion probe” which is a tool for validating the transient deformation simulation. The casting geometry and setup with results were presented at the last T&O [1]. The example was a result where no hot tears are expected because there was little restraint on the hot spot section. The setup of this casting is shown in Figure 10. The mold is shown in a light grey, the casting is in red, and the gating is in solid grey. The dimensions of the long bar section are 1” by 1” by 36”. This ASTM A216 Grade WCB carbon steel casting was poured at the University of Northern Iowa. This casting was expected to shrink to the unrestrained shrinkage factor, patternmaker’s shrink, across every dimension. In two locations dimensional data was measured during the casting process.

The experimental setup is shown in the schematic in Figure 11. Labels D2 and D4 indicate the locations of the dimensional probes. There are no bolts or force measurements in this casting trial. The probes are quartz rods that are installed in the mold running from outside the mold to the casting surface. On the end of the quartz rod that is outside the mold, a linear voltage displacement transducer (LVDT) records the location of the casting surface. In addition to the dimensional probes, a thermocouple is placed in the hot spot to record the temperature for validation of the temperature simulation.

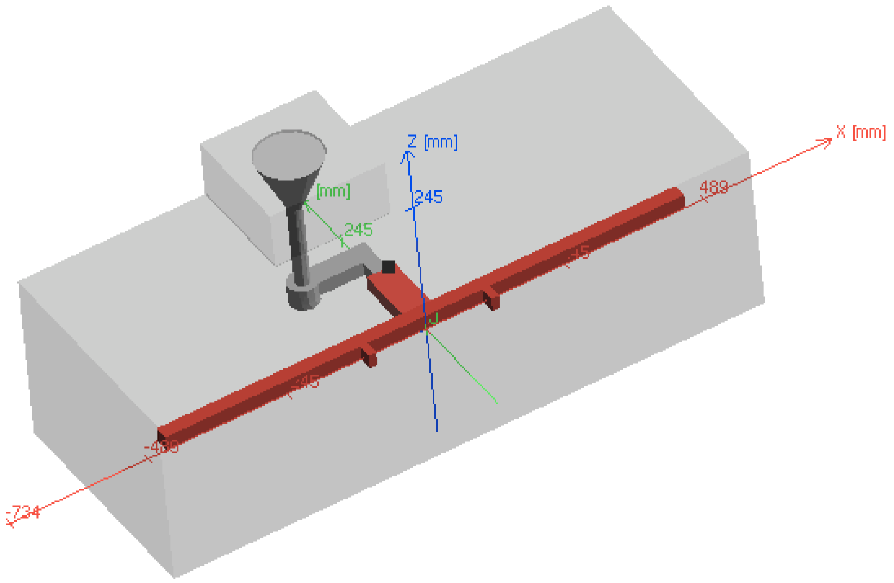

Figure 10. The isometric view of the casting setup in MAGMAsoft. The casting is in red and the gating is in solid grey. The mold is shown transparent in light grey.

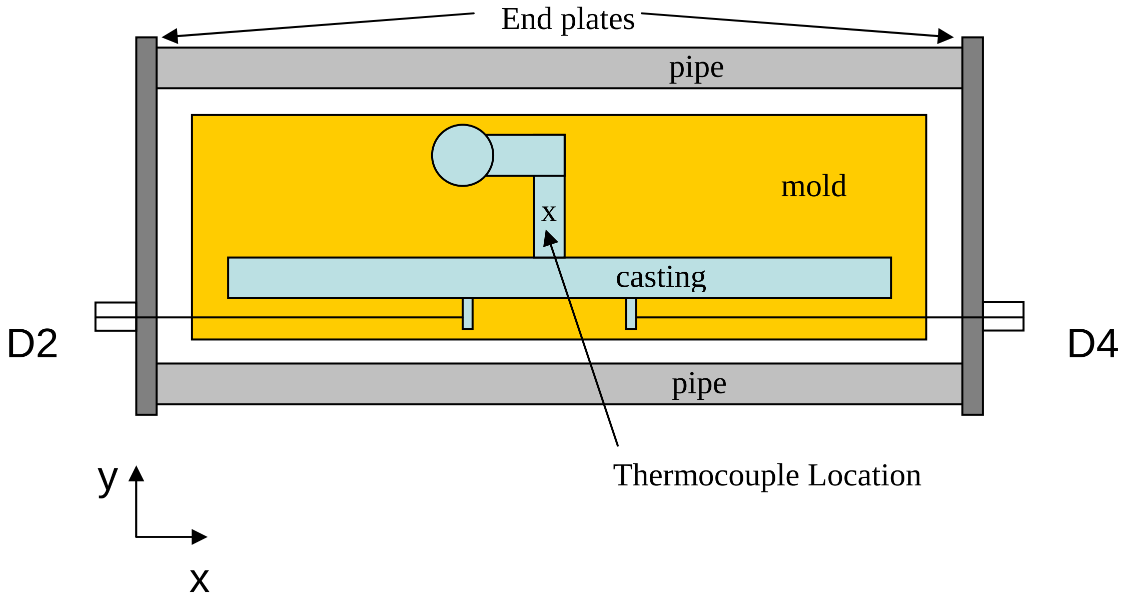

Figure 11. Schematic showing casting setup and probe locations.

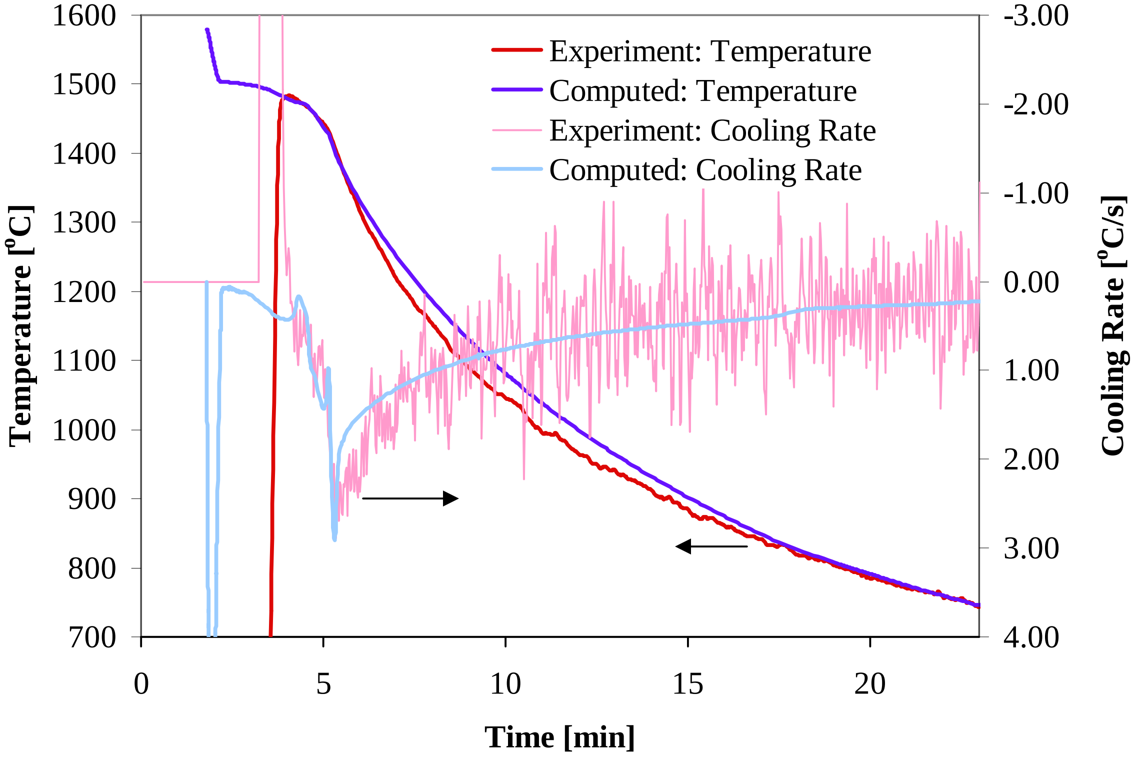

Figure 12. Comparison of the experimental thermocouple data to the simulation temperatures over the first 25 minutes of cooling.

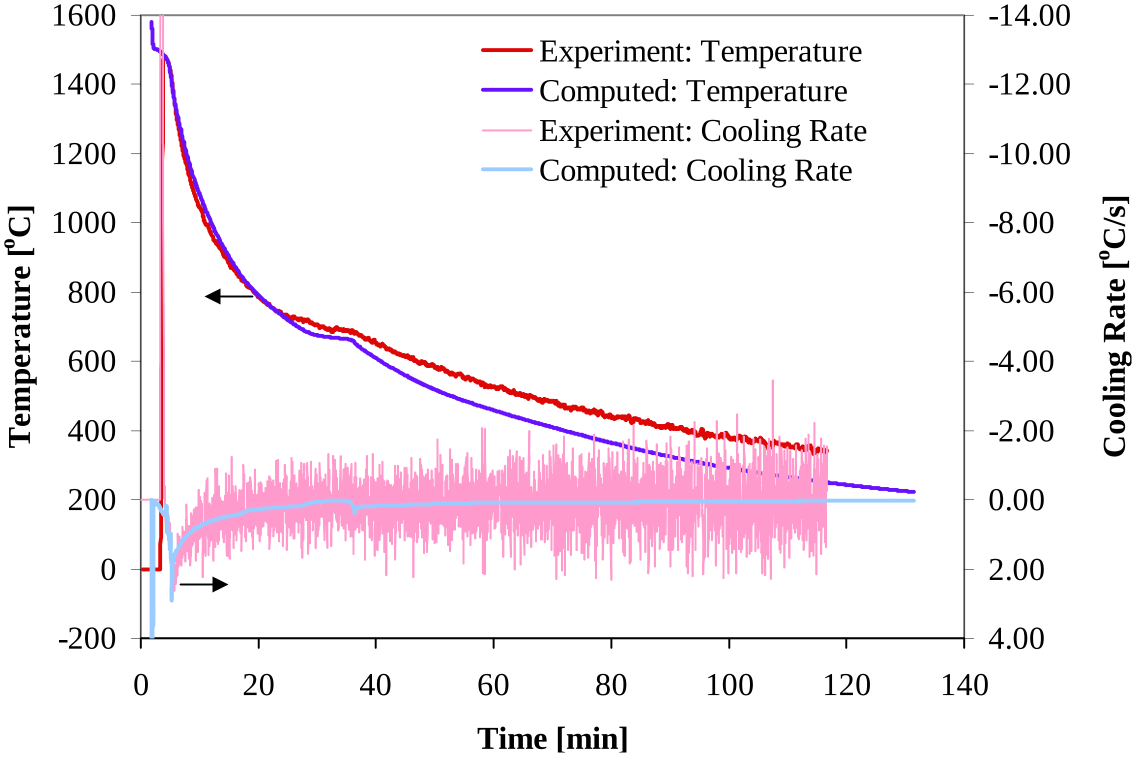

Figure 13. Comparison of the experimental thermocouple data to the simulation temperatures over the entire cooling.

Using the geometry in Figure 10, the filling event and heat transfer are calculated. Figures 12 and 13 show the temperature agreement of the thermocouple and the simulated temperature. This must agree not only in the solidification temperature interval but also down to the final temperature. This is needed for accurate prediction of the entire deformation behavior. The above temperature and cooling rate agreement is sufficient for the purposes of this comparison, however does not illustrate perfect agreement. The temperature arrests at both the solidus and again at the solid state transformation at around 30 minutes and about 650 ^{o}C in the experiment.

A new MAGMAstress algorithm is used for the simulation of the deformation. New features of this simulation include a finite element solution and new material models. One new feature is the contact model. The old contact model in MAGMAsoft joins two materials together as a single final material with fused contact. Where the material would always be in contact, such as around cores, this works well. In general, casting surfaces will pull away from the mold, core, or other interacting body. The new MAGMAstress algorithm has implemented a contact model with air gap formation and contraction around a core.

The temperature in the casting at ~1.5 hrs is shown in Figure 14. The undeformed geometry is shown at the top and a deformed casting geometry is shown on bottom. A magnification factor of 10 has been applied to the deformation. The simulation of deformation does not include the mold. This result indicates that the casting without the mold will uniformly contract. The space between the tabs off the long bar can be considered a gauge length. Figure 14 shows that the change from the original gauge length to the current gauge length, which changes in time, is the gauge displacement. Also it can be seen that the gauge displacement is a negative number indicating that the gauge length is contracting. In Figure 15, the simulation of distortion is shown with the mold contact included. Notice that an air gap does form in unrestrained dimensions. In restrained dimensions, the contraction of gauge length is restricted by the mold. If the mold is similar in strength to the metal this resistance may be expected to be important.

The change in the gauge length over time is shown in Figure 16. The experimental curve shows the change in position for the probe locations D2 and D4. The change in gauge length with time can be compared to similar points in a simulation. This transient data shows that the gauge closes over the entire experiment. At the Austenite to Ferrite decomposition temperature, an arrest in the closing behavior is seen at about 20 minutes into the experiment. At the phase transformation, the solid expands. After expansion, the solid continues to shrink during further cooling. In the case of no mold restriction, the gauge length shrinks to the expected patternmaker's shrink, ~2.4%, or 4.9 mm in this case. The mold was modeled using a single temperature independent elastic modulus. No thermal expansion or plasticity was included in modeling the mold deformation. In this small parametric study, the mold stiffness was varied from 1500 MPa to 3000 MPa. The final value of elastic modulus was set at 2250 MPa. For reference, the elastic modulus of silica is about 98000 MPa, and for unbonded sand about 150 MPa. Increasing the mold stiffness acts to restrict the shrinkage of the gauge length. This mold effect is most significant early in cooling, ~20min. After the casting cools to a low temperature with greater strength, the mold stiffness no longer prevents casting movement. A reasonable model for mold deformation and suitable properties must be included to predict casting distortion and hot tearing tendency.

The above simulations illustrate prediction of casting transient deformation and final distortion. The accumulated yielding, movement, stresses, etc. are all included from the pouring to final shakeout. All of the filling temperatures and heat transfer temperatures must be known to predict the deformation. In addition, the temperature dependent properties for the metal and the mold must be known. Although the simulation result appears reasonable with the appropriate choice of mold stiffness, it is not known whether this value for the elastic modulus of the mold is correct or even if modeling the mold as elastic is correct. Further validation is being studied to continue improving the models, properties, and simulations. The goal is to have a prediction that may be used as an engineering tool to improve casting design and optimize for more robust casting process with minimum defects.

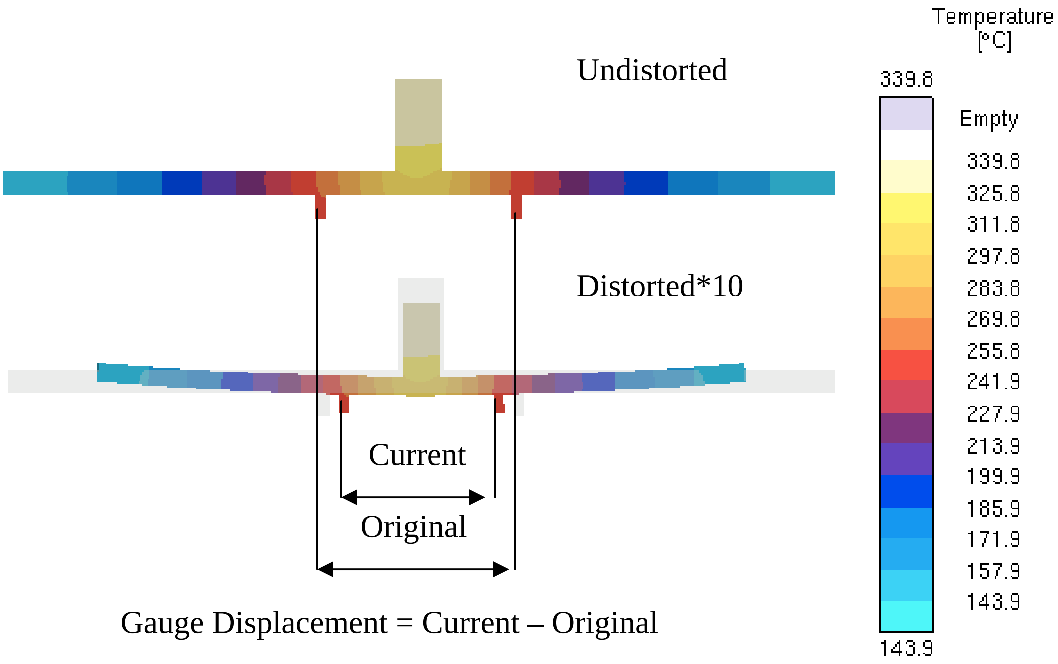

Figure 14. Temperatures at ~1.5 hours into the simulation without the mold of the experiment. The temperatures are shown on a distorted casting geometry that has been magnified by a factor of 10.

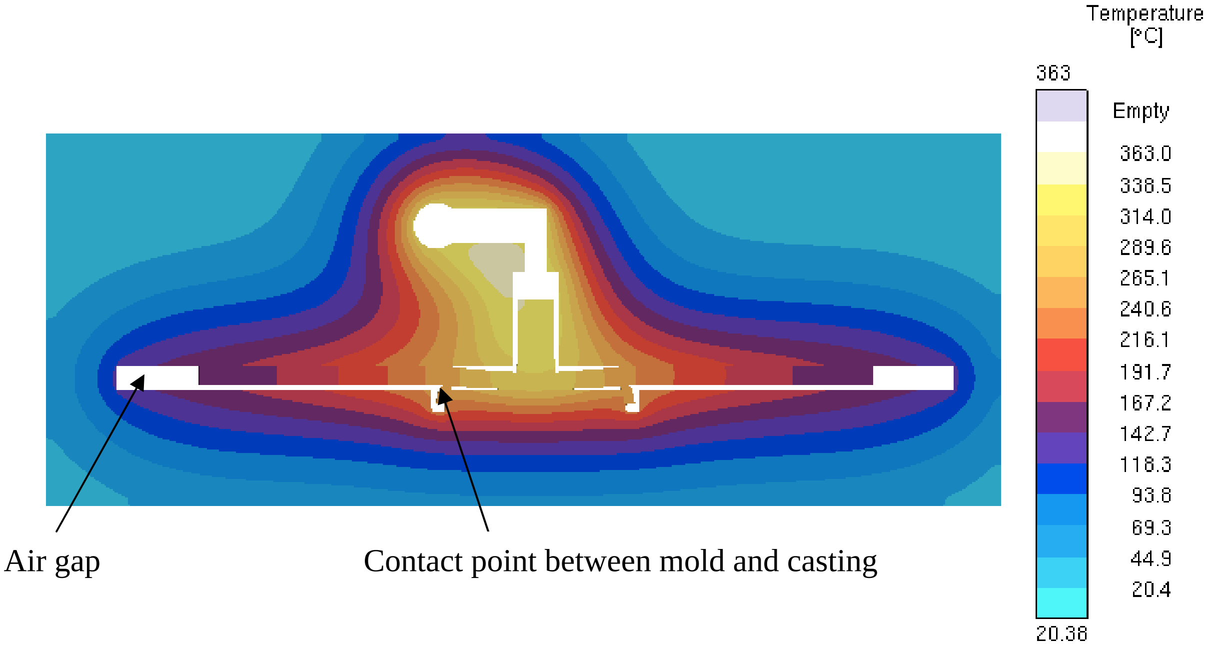

Figure 15. Temperatures at ~1.5 hours into the simulation with the mold of the experiment. The temperatures are shown on a distorted casting and mold geometry that has been magnified by a factor of 10. The air gap around the casting is shown in white.

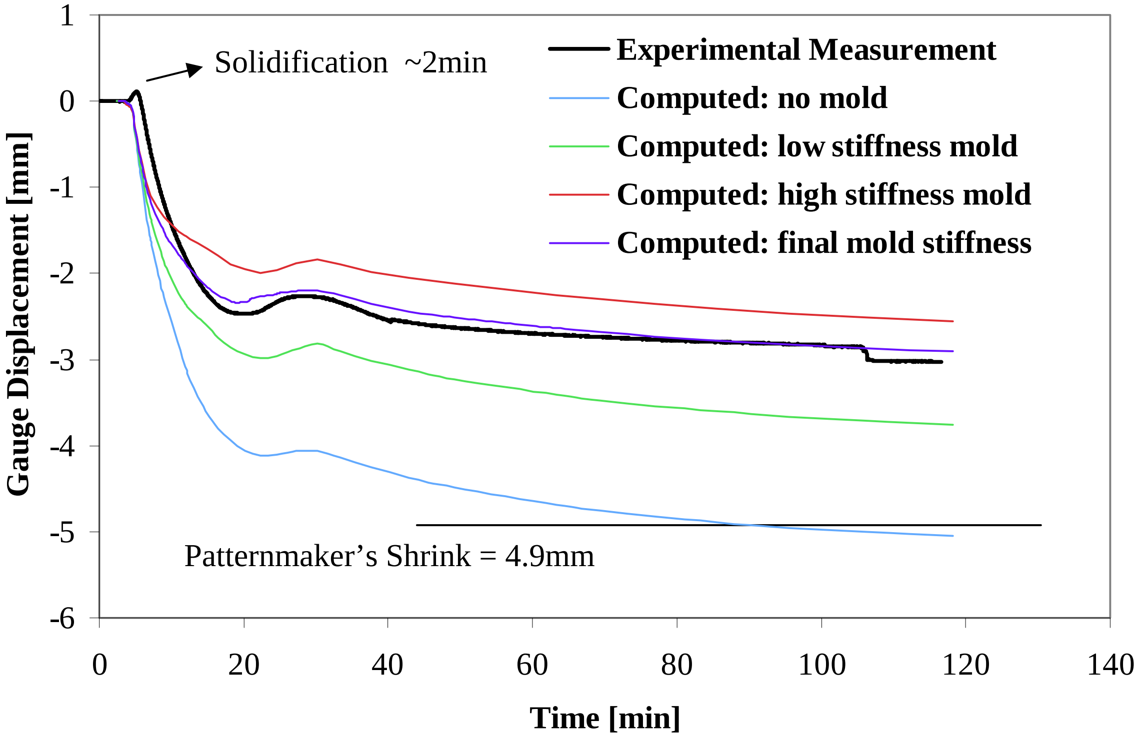

Figure 16. Graph showing the gauge displacement closing either to patternmakers shrink for the simulation with no mold or to the experimental value with the proper choice of mold stiffness.

Discussion

Temperature dependent material mechanical properties for low alloy steel used for modeling are shown. These properties are from high temperature experimental data and Jmatpro. MAGMAsoft is shown to give reasonable distortion prediction for a casting with mold restraint. The entire transient deformation process from pouring to shakeout is measured experimentally and compared to simulation. Results would be useful for reducing distortion and to predict the final properties.

Acknowledgements

This work was prepared with the support of the U.S. department of Energy (DOE) Award No. DE-FC36-04GO14230. However, any opinions, findings, conclusions, or recommendations expressed herein are those of the authors, and do not necessarily reflect the views of the DOE. The authors wish to that the Steel Founder's Society of America, especially Malcolm Blair and Raymond Monroe for their assistance in this work.

References

1. C. Monroe and C. Beckermann, "Simulation of Hot Tearing and Distortion during Casting of Steel: Comparison with Experiments," Steel Founders Society of America, T&O, December 2006.
2. *Jmatpro 4.0*, Sente Software Ltd., Surrey Tech. Center, 40 Occam Road, Guildford GU2-7YG, United-Kingdom.
3. P.J. Wray, "The effect of carbon content on the plastic flow of plain carbon steels at elevated temperature," *Metallurgical Transactions A*, 13A, 1982.
4. P. Kozlowski, J. Azzi, and B.G. Thomas, "Simple constitutive equations for steel at high temperature," *Metallurgical and Materials Transactions A*, 23A, 1992.
5. *MAGMAsoft*, MAGMA GmbH, Krackerstrasse 11, 52072 Aachen, Germany.

Modeling of Casting, Welding, and Advanced Solidification Processes - XII
Edited by: Steve L. Cockcroft and Daan M. Maijer
TMS (The Minerals, Metals & Materials Society), 2009

SIMULATION OF DEFORMATION AND HOT TEAR FORMATION USING A VISCO-PLASTIC MODEL WITH DAMAGE

C.A. Monroe [1], C. Beckermann[1], J. Klinkhammer [2]

[1] Dept. Mechanical and Industrial Engineering, University of Iowa, Iowa City, Iowa 52242, USA
[2] MAGMA Giessereitechnologie GmbH, Kackertstrasse 11, D-52072 Aachen, Germany

Abstract

A three-phase model is presented that predicts solid deformation and damage as well as melt pressure, feeding flow and shrinkage porosity during metal casting. A visco-plastic constitutive theory with damage is used to model the solid deformation. Damage created by mechanically induced voiding is used as a hot tear indicator. The absence of liquid feeding determines when damage starts to form. The model has been implemented in general-purpose simulation codes. Novel steel casting experiments have been designed and performed which measure the deformation and force from solidification to shakeout. The measured and predicted deformations show generally good agreement with the simulation results. Furthermore, the damage predictions show good correspondence with hot tear indications on a radiograph of the test casting.

1. Introduction

In all casting processes, hot tearing and distortion during solidification and cooling are serious defects. Hot tears are cracks that initiate in the mushy zone at high solid fractions [1]. The two necessary conditions for hot tearing are (a) lack of liquid feeding and (b) tensile strain. First, liquid metal feeding is induced by solidification shrinkage. At high solid fractions, this liquid flow may be cut off because the permeability of the mushy zone becomes too low. Note that in shaped castings, a lack of liquid feeding can occur even at low solid fractions when a hot spot is present. The absence of liquid feeding signals the onset of shrinkage porosity formation. Second, non-uniform thermal contractions and mechanical restraints can cause the solid to strain. Such strains result in casting distortions and may also cause additional voiding. This additional voiding due to tensile strains is called damage. Hot tears are a manifestation of the damage that occurs during solidification.

In order to predict hot tearing and distortion, realistic and efficient models must be used to calculate the temperature, liquid flow, and strain fields during solidification and cooling of a casting. M'Hamdi *et al.* [2], Mathier *et al.* [3] and others have proposed two-phase models for calculating liquid flow and solid strain. Void nucleation is assumed to occur at a certain critical liquid pressure drop. After void nucleation, the volumetric part of the inelastic solid strain is integrated to obtain the void volume associated with the formation of a hot tear. However, the solid fraction is assumed to be a function of temperature only, and the effect of voids on the mechanical behavior of the solid (in the absence of liquid) is neglected.

In the present study, deformation and hot tearing during casting is modeled using a visco-plastic constitutive equation for the solid that accounts for the presence of voids (porosity). The liquid feeding flow and shrinkage porosity are predicted using the model first presented in Ref. [4]. Integration of the damage is started when the liquid feeding flow is predicted to be cut off.

The effects of solid deformation on liquid flow and of liquid pressure on solid deformation are neglected. Although the shrinkage porosity and the damage porosity are calculated separately, both porosities affect the mechanical behavior of the solid. The damage induced porosity is used as a hot tear indicator. The predictions of the present model are validated using a specially designed steel sand casting that allows for simultaneous force and displacement measurements during solidification and cooling.

2. Model Description

The volume averaged model accounts for the presence of three phases: solid (*s*), liquid (*l*), and porosity (*p*), such that the volume fractions add to unity, i.e., $g_s + g_l + g_p = 1$. While liquid is present, the solid fraction is assumed to be a unique function of the temperature, *T*, or $g_s(T)$. The porosity phase is split into two contributions, shrinkage and damage, i.e., $g_p = g_{p,sh} + g_{p,d}$. The shrinkage and damage porosity start to form when the liquid pressure falls to the negative of the critical capillary pressure for pore formation. The feeding flow, liquid pressure, and shrinkage porosity model used in the present study [4] neglects any contribution from the deformation of the solid. This model has previously been implemented in a general-purpose casting simulation code [5] that also provides the necessary heat transfer calculations.

The deformation of the solid and the mushy zone (above coherency) is modeled using the concept of an effective stress tensor, $\boldsymbol{\sigma}_s$, for porous solids. As in Ref. [3], the effects of the liquid pressure and liquid shear stress, as well as of gravity, on the solid deformations are neglected. Then, the solid momentum equation reduces to $\nabla \cdot \boldsymbol{\sigma}_s = 0$. The total strain is decomposed into three contributions: thermal, elastic, and visco-plastic. The thermal strain is calculated using the temperature dependent density; only the density changes below the solidus (100% solid) temperature are included. Hooke's law is used to determine the elastic strain. The elastic stiffness tensor is defined by the Young's modulus, *E*, and the Poisson ratio, ν. Both elastic constants depend on temperature and solid fraction [6, 7]. The visco-plastic strain is calculated using an associative flow law. The flow law and the associated yield function are given in Table 1. In the yield function, the solid pressure and the von Mises stress are given by $p_s = -(\boldsymbol{\sigma}_s : \mathbf{1})/3$ and $q_s = 2|\boldsymbol{\sigma}_s + p_s \mathbf{1}|/3$, respectively.

A variety of yield functions are used to model plasticity of porous materials [8, 9, 10]. In the present study, the quadratic yield function from Cocks [8] given in Table 1 is adopted. The functions A_1 and A_2 depend on the volume fraction solid. When the solid fraction is equal to unity, this model reduces to a classical von Mises yield model. In order to account for void coalescence and solid coherency, the solid fraction used in the yield function is scaled according to the expression provided in Table 1. The solid fraction is only scaled below the so-called coalescence solid fraction, g_s^{coal}. For solid fractions below the coalescence solid fraction, voids coalesce and the mush rapidly weakens. The scaled solid fraction reaches zero at the so-called coherency solid fraction, g_s^{coh}. For solid fractions below the coherency solid fraction, the mush has no strength and stiffness. The dynamic yield stress is calculated from the power law given in Table 1, and includes both isotropic hardening and creep (rate-dependency). As shown in Table 1, the equivalent strain, ε_{eq}, and the equivalent strain rate, $\dot{\varepsilon}_{eq}$, are found from the scalar dissipation of energy.

The damage porosity is obtained by integrating the volumetric part of the visco-plastic strain over time (see Table 1). The integration starts at the time t_f, when the feeding flow is cut off. The damage porosity either reduces or increases the solid fraction. Once solidification is complete, the solid fraction used in the mechanical constitutive equations is reduced by the entire porosity fraction, including shrinkage and damage. Hence, the effect of the voids on the mechanical behavior of the solid is taken into account.

The above model for the solid deformations was implemented in a user subroutine of the finite element software ABAQUS [11]. The numerical solution method uses an implicit-explicit integration scheme [9, 10]. Simulations were performed for the steel sand casting described below. The thermophysical properties of the steel were calculated using IDS [12]. The necessary mechanical properties were determined using published data [13, 14, 15]. The deformation of the sand mold, and the contact between the casting and the mold, were also simulated using ABAQUS.

Table 1. Equations and parameters used to model solid deformation.

Equations
Flow law and Yield function: $\dot{\boldsymbol{\varepsilon}}_s^{vp} = \dot{\gamma}\dfrac{\partial f_Y}{\partial \boldsymbol{\sigma}_s}$ and $f_Y = q_s^2 + A_1 p_s^2 - A_2\sigma_{dy}^2 \leq 0$, where $A_1 = \dfrac{9\left(1-g_s^*\right)}{2\left(2-g_s^*\right)\left(1+m\right)\left(1+2\left(1-g_s^*\right)/3\right)}$ and $A_2 = \left(1+2\left(1-g_s^*\right)/3\right)^{-1}\left(g_s^*\right)^{2/(1+m)}$ Scaled solid fraction: $g_s^* = g_s^{coal}\left(g_s - g_s^{coh}\right)/\left(g_s^{coal} - g_s^{coh}\right)$
Dynamic yield stress and equivalent strain: $\sigma_{dy} = \sigma_0\left(1+\varepsilon_{eq}/\varepsilon_0\right)^n\left(1+\dot{\varepsilon}_{eq}/\dot{\varepsilon}_0\right)^m$ and $\dot{\varepsilon}_{eq} = \boldsymbol{\sigma}_s : \dot{\boldsymbol{\varepsilon}}_s^{vp} / g_s\sigma_{dy}$
Damage evolution: $g_{p,d} = \int_{t_f}^{t} g_s\dot{\boldsymbol{\varepsilon}}_s^{vp} : \mathbf{1}dt$

Parameters and Constants	
Quantity	**Value**
Room Temperature 0.2% offset yield strength	317 MPa
Coherency solid fraction	0.5
Coalescence solid fraction	0.85
100% Solid Temperature and Anneal Temperature	1415 ^{o}C

3. Experimental Setup

Steel sand casting experiments were performed to validate the model. The unique feature of the experimental setup is that it allows for simultaneous force and displacement measurements during solidification and cooling of the casting. In addition, the casting can be mechanically restrained in order to induce relatively high stresses and hot tearing. As shown schematically in Figure 1, the casting consists of a 36” (0.914 m) long, 1” (25.4 mm) thick bar, referred to as “arm”. Experiments were performed for arms widths of 1” (25.4 mm) and 2” (50.8 mm). The casting was gated using a runner that meets the bar at mid-length. This runner, referred to as “leg”, creates a hot spot at the mid-length of the arm. A thermocouple was placed near the center of the leg. Leg widths of 1” (25.4 mm) and 2” (50.8 mm) were utilized in the experiments. Casting restraint was achieved by bolts that were embedded in the two ends of the arm. The bolts were connected to a flask that surrounds the mold. The restraining forces were measured using temperature compensated force gauges in each bolt. In one experiment, the bolts were removed so that the arm can contract freely. Displacements were measured using two quartz rods connected to LVDTs. The quartz rods were embedded into the casting through tabs that were cast on the arm on both sides of the hot spot. As shown in Figure 1, the gap between the two tabs defines the gauge length for the displacement measurements. Depending on the restraint offered by the bolt/flask arrangement, the gap can either open (defined as positive gap displacement) or close. The mold was made of phenolic urethane bonded silica sand. The WCB low-alloy steel was poured at 2966°F (1630°C).

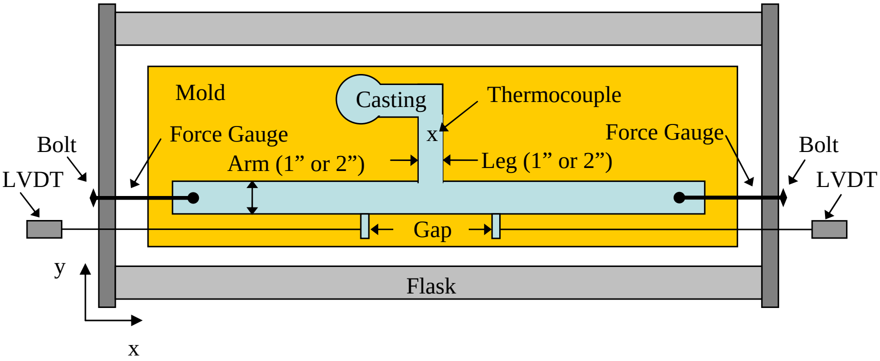

Figure 1. Schematic of the test setup for the steel sand casting experiments.

4. Results and Discussion

An example of a comparison between measured and predicted temperatures is shown in Figure 2. The good agreement between the measurements and predictions was achieved by using a temperature dependent mold-metal interfacial heat transfer coefficient (not shown here due to space limitations). Similar agreement was obtained for all experiments.

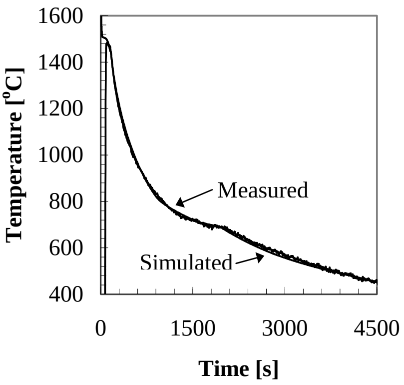

Figure 2. Comparison of measured and predicted temperatures.

Predicted mid-thickness shrinkage porosity fields are shown in Figure 3 for two cases: 2” arm with 2” leg; and 1” arm with 1” leg. In both cases, significant centerline shrinkage is predicted in the arm and leg, since the castings are not risered. In addition, a large amount of shrinkage porosity can be observed at the hot spot that is present near the arm-leg junction. This porosity pattern is as expected. Recall that the time during solidification at which the shrinkage porosity is predicted to start forming at a particular location in the casting is used in the stress analysis as the start time for the integration of the damage.

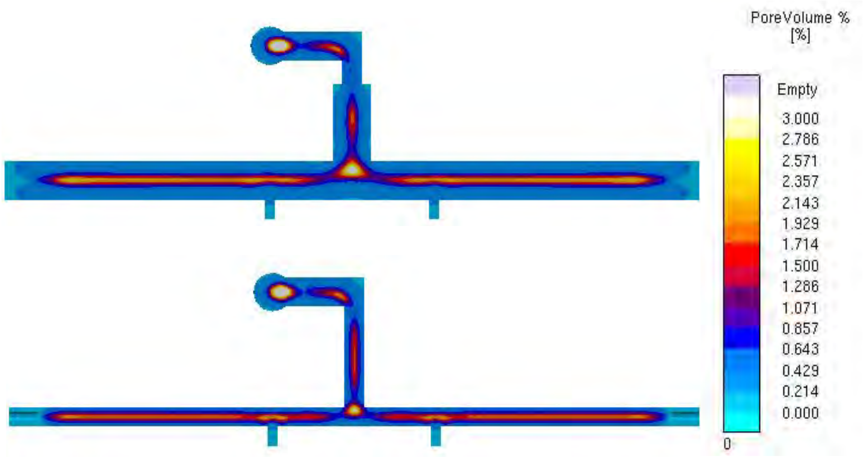

Figure 3. Predicted mid-thickness shrinkage porosity fields for the 2" wide arm/leg (top) and the 1" wide arm/leg (bottom) castings.

One casting was poured unrestrained, without the bolts, the results for which are shown in Figure 4. The measured gap displacement as a function of time is shown in Figure 4(b). It can be seen that, as expected, the gap closes (i.e., the displacement is negative) due to thermal contraction of the arm. However, at about 1100 s after pouring, the gap starts to open by a small amount. This opening can be attributed to the expansion associated with the austenite to pearlite phase transformation. The transformation is complete at approximately 1600 s, after which the

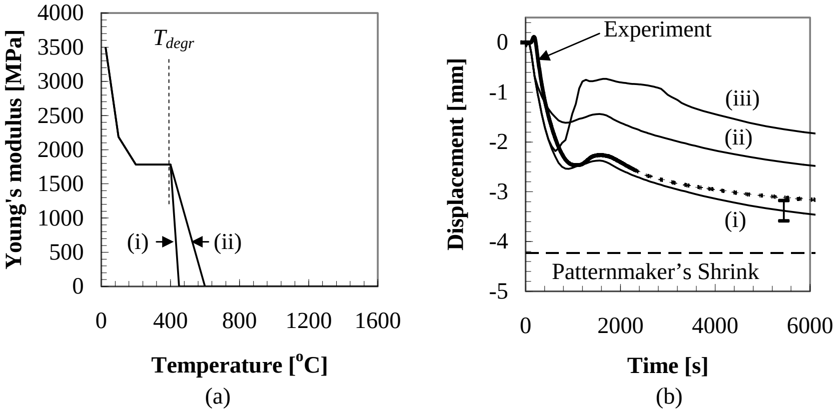

Figure 4. (a) Variation of Young's modulus of the mold with temperature. (b) Comparison of measured and predicted gap displacement variations for the unrestrained casting; predicted results are shown for three different cases: (i) baseline mold stiffness with degradation; (ii) higher mold stiffness at high temperatures, with degradation; (iii) baseline mold stiffness but no degradation upon cooling.

gap starts to close again. As indicated in Figure 4(b), the final measured gap displacement, when the casting is at room temperature, is significantly smaller than the value anticipated from the so-called Patternmaker's Shrink rule for free contraction of steel castings (2.08%). This effect can be attributed to the displacement of the tabs being hindered by the mold between the two tabs. This hindrance is a strong function of the mold stiffness. Simulations were performed for three different mold stiffness variations with temperature. As plotted in Figure 4(a), the baseline mold stiffness variation [case (i)] shows a sharp drop to zero at approximately 400°C. The drop occurs above the binder degradation temperature, T_{degr}. Once the binder is degraded, the mold does not regain stiffness when it cools to lower temperatures. This baseline mold stiffness variation produces excellent agreement between the measured and predicted gap displacements, as shown in Figure 4(b). In case (ii), degradation is also included, but the drop in the mold stiffness above T_{degr} is not as steep and the stiffness does not vanish until about 600°C. This mold stiffness variation results in smaller predicted gap displacements that are in disagreement with the measurements. In case (iii), the same mold stiffness variation as in case (i) is used, but the mold is allowed to regain its stiffness upon cooling, regardless of how high a temperature it had reached previously. This mold stiffness variation also results in incorrect gap displacement predictions [Figure 4(b)].

Next, results are provided for two restrained castings: 2" arm with a 2" leg; and 1" arm with a 1" leg. The measured forces for these two castings are shown in Figure 5. In each experiment, the force measurements at the two bolts were very similar, and only the average values are plotted. It can be seen that the forces begin to increase quickly after the solidification of the arms. The drop in the forces at intermediate times can again be attributed to the expansion associated with the austenite to pearlite transformation. Note that the expansion occurs at different times for the two experiments, since the castings have much different cooling rates. After the phase transformation is completed, the forces increase again. These measured force variations are used as a boundary condition at the end of the arms in the deformation simulations.

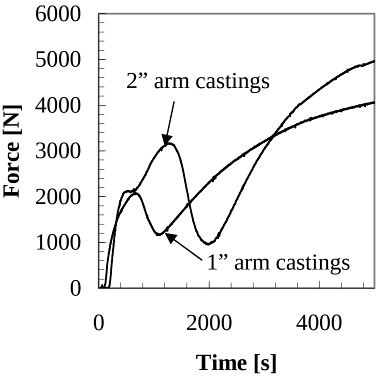

Figure 5. Variation of the average force in the restrained castings with time.

Comparisons of the measured and predicted gap displacements for the restrained castings are shown in Figure 6. Good agreement is obtained for the 2" arm/leg restrained casting [Figure 6(a)]. For this casting the gap displacements are similar to the ones for the unrestrained casting [Figure 4(b)], indicating that the stresses in the 2" wide arm are too low to cause significant yielding. For the 1" arm/leg casting, results from two separate, but nominally identical experiments are included in Figure 6(b). The measured gap displacements for the two experiments are similar and demonstrate little overall gap opening or closing. This indicates that the restraint induces significant yielding. Since the measured forces are of a similar magnitude in the 2" and 1" arm/leg (Figure 5) experiments, the stresses are approximately twice as high in the 1" wide arm as in the 2" wide arm. The simulation of the 1" arm/leg experiments predicts a larger gap closing than measured. Reasons for the disagreement may include uncertainties in the high-temperature mechanical properties and inaccurate modeling of crack propagation.

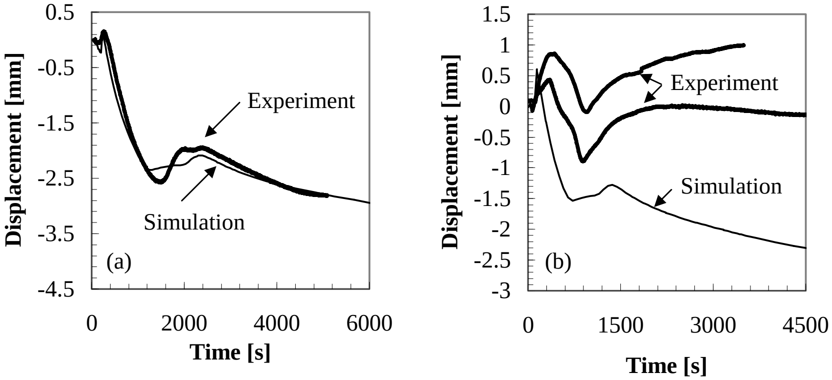

Figure 6. Comparison of measured and predicted gap displacements for the restrained castings; (a) 2” arm/leg, (b) 1” arm/leg.

Figure 7(a) shows the predicted distortions (magnified by a factor of five) and damage porosity field for the restrained 2” arm/leg casting. The casting can be seen to contact the mold at several locations along the metal-mold interface, while at other locations a gap forms. The predicted damage is mostly confined to the hot spot at the junction between the arm and the leg. A radiograph of the casting is provided in Figure 7(b). It shows a large crack in the center of the hot spot region, which is in good agreement with the damage prediction. The smaller indications along the centerline of the arm correspond well with the predicted porosity. Although this comparison is not of a quantitative nature, it illustrates the highly coupled nature of the shrinkage porosity and the damage porosity.

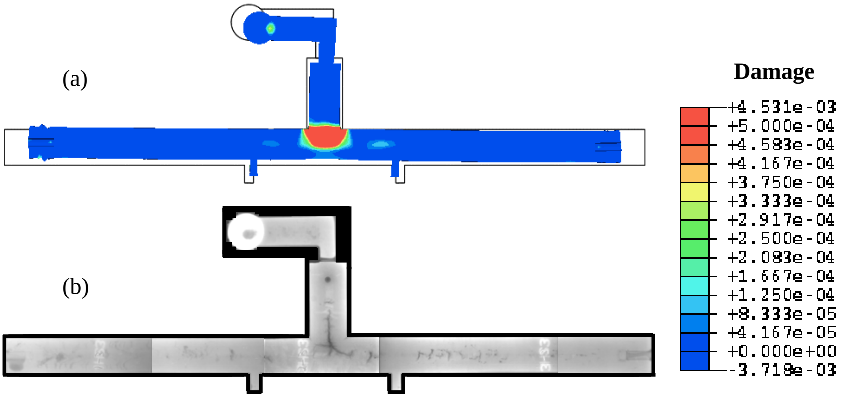

Figure 7. Results for the restrained 2” arm/leg casting. (a) Predicted distortions (five times magnified) and damage porosity field; (b) radiograph of the casting.

5. Conclusions

A model for the deformation and damage accumulation during solidification and cooling of shaped castings has been developed. Novel steel sand casting experiments, which allow for simultaneous displacement and force measurements, are used to validate the model predictions. Good overall agreement is obtained. However, some uncertainty remains regarding the high temperature mechanical properties used in the simulations. The comparisons also illustrate the importance of accurate modeling of the mechanical behavior of the mold, including binder degradation. Additional work is needed to verify the model for situations where significant hot tearing occurs. Such hot tearing significantly affects the subsequent deformation of a casting.

Acknowledgements

This work was supported by the Iowa Energy Center under grant number 06-01 and by DOE under Award No. DE-FC36-04GO14230. The authors would like to thank Dr. Jerry Thiel of the University of Northern Iowa for his help with the steel casting experiments.

References

1. M. Rappaz, J.-M. Drezet, and M. Gremaud, “A new hot-tearing criterion,” *Metall. Mater. Trans. A*, 30A (1999), 449-455.
2. M. M’Hamdi, A. Mo, and H. G. Fjaer, “Tearsim: A two-phase model addressing hot tearing formation during aluminum direct chill casting,” *Metall. Mater. Trans. B*, 37 (2006), 3069-3083.
3. V. Mathier, J.-M. Drezet, and M. Rappaz, “Two-phase modeling of hot tearing in aluminum alloys using a semi-coupled approach,” *Modelling Simul. Mater. Sci. Eng.*, 15, (2007), 121-134.
4. K. Carlson, Z. Lin, R. Hardin, C. Beckermann, G. Mazurkevich, and M. Schneider, “Modeling of porosity formation and feeding flow in steel casting,” in *Modeling of Casting, Welding, and Advanced Solidification Processes X*, TMS (2003), 295-302.
5. MAGMAsoft v4.5, MAGMA GmbH, Aachen, Germany
6. R. A. Hardin and C. Beckermann, “Effect of porosity on the stiffness of cast steel,” *Metall. Mater. Trans. A*, 38 (2007), 2992-3006.
7. A. Roberts and E. Garboczi, “Elastic properties of model porous ceramics,” *Journal of the American Ceramic Society*, 83 (2000), 3041-3048.
8. A. C. F. Cocks, “Inelastic deformation of porous materials,” *J. Mech. Phys. Solids*, 37 (1989), 693-715.
9. E. B. Marin and D. L. McDowell, “A semi-implicit integration scheme for rate-dependent and rate-independent plasticity,” *Computers and Structures*, 63 (1997), 579-600.
10. P. Sanchez, A. Huespe, and J. Oliver, “On some topics for the numerical simulation of ductile fracture,” *Int. J. of Plasticity*, 24 (2008), 1008-1038.
11. ABAQUS v6.7-1, D S Simulia, Dassault Systemes
12. J. Miettinen, “Calculation of solidification-related thermophysical properties for steels,” *Metall. Mater. Trans. B*, 28A (1997), 281-297.
13. P. J. Wray, *Modeling of Casting and Welding Processes*, Ringe, NH: AIME Conference Proceedings (1980), 245-257.
14. P. J. Wray, “Effect of carbon content on the plastic flow of plain carbon steels at elevated temperatures,” *Metall. Mater. Trans. A*, 13A (1982), 125.
15. *High Temperature Property Data: Ferrous Alloys*, ASM International, Metals Park, OH (1988).